Tajik Depression and Greater Pamir Neotectonics from InSAR Rate Maps

Sabrina Metzger[1], Łukasz Gągała[2], Lothar Ratschbacher[3], Milan Lazecky[4], Yasser Maghsoudi[4], and Bernd Dieter Schurr[5]

[1]Helmholtz-Zentrum, Deutsches GeoForschungsZentrum Potsdam
[2]Technische Universität Bergakademie Freiberg
[3]Geologie, Technische Universität Bergakademie Freiberg, 09599 Freiberg, Germany
[4]University of Leeds
[5]Deutsches GeoForschungsZentrum GFZ

November 30, 2022

Abstract

Embedded between the Tian Shan, Pamir, and Hindu Kush, the Tajik depression is a remnant of the Mesozoic-Miocene Tajik-Tarim basin system. Since ~12 Ma, westward collapse of the north-advancing Pamir-Plateau crust inverted the Tajik basin into a thin-skinned fold-thrust belt with ~150 km of ~E-W shortening distributed between foreland- and hinterland-vergent structures. Geodetically-derived shortening rates decay westward from ~15 to 2 mm/yr. Seismicity outlines the ~east-striking dextral Ilyak fault, bounding the fold-thrust belt in the north, and distributed shortening in the central and eastern Tajik depression. We derived E-W and vertical deformation-rate maps from radar interferometric time-series, consisting of 900+ radar scenes acquired over 2.0-4.5 years, and available accurate positioning data. We confirm the westward collapse of the Pamir and the drastic shortening-rate decline across the Main Pamir Thrust at the Pamir front. In the Tajik depression, the maps unveil a combination of basin-scale tectonics, local halokinesis, and seasonal/weather-driven soil or near-surface effects. Although the Tajik-basin strata move westward with rates decreasing away from the Pamir, the most external Babatag backthrust currently absorbs the highest shortening (~6 mm/yr) as it has done in the past (>20 km). The Ilyak fault accommodates ~5-8 mm/yr, eastward-increasing slip; rates decay sharply across the fault, suggesting a locking depth of <1 km - possibly creep. At least 10 mm/yr uplift and westward motion occur across the Tajik-depression-Pamir transition, including the sinistral Darvaz fault zone, likely outlining a crustal-scale ramp. The Hoja Mumin salt fountain is spreading laterally at >300 mm/yr.

Sabrina Metzger[1], Łukasz Gągała[2,3], Lothar Ratschbacher[2], Milan Lazecký[4], Yasser Maghsoudi[4] and Bernd Schurr[1]

[1]Lithosphere Dynamics, Helmholtz Center, Research Center for Geosciences, Potsdam, Germany.

[2]Geologie, Technische Universität Bergakademie Freiberg, Freiberg, Germany.

[3]Now at Hellenic Petroleum, Marousi, Greece.

[4]COMET, School of Earth and Environment, University of Leeds, United Kingdom.

Corresponding author: Sabrina Metzger (*metzger@gfz-potsdam.de*)

Key Points:

- The east- and up-rate maps exhibit tectonic and anthropogenic processes with mm-accuracy in high spatial resolution (400 m).

- The quality of our rate maps depends on interferometric data coherence and the availability of accurate positioning data.
- The major tectonic signal is E–W shortening in the Tajik fold-thrust belt due to the westward collapse of the Pamir-Plateau crust.

Abstract

Embedded between the Tian Shan, Pamir, and Hindu Kush, the Tajik depression is a remnant of the Mesozoic-Miocene Tajik-Tarim basin system. Since ~12 Ma, westward collapse of the north-advancing Pamir-Plateau crust inverted the Tajik basin into a thin-skinned fold-thrust belt with ~150 km of ~E–W shortening distributed between foreland- and hinterland-vergent structures. Geodetically-derived shortening rates decay westward from ~15 to 2 mm/yr. Seismicity outlines the ~east-striking dextral Ilyak fault, bounding the fold-thrust belt in the north, and distributed shortening in the central and eastern Tajik depression. We derived E–W and vertical deformation-rate maps from radar interferometric time-series, consisting of 900+ radar scenes acquired over 2.0–4.5 years, and available accurate positioning data. We confirm the westward collapse of the Pamir and the drastic shortening-rate decline across the Main Pamir Thrust at the Pamir front. In the Tajik depression, the maps unveil a combination of basin-scale tectonics, local halokinesis, and seasonal/weather-driven soil or near-surface effects. Although the Tajik-basin strata move westward with rates decreasing away from the Pamir, the most external Babatag backthrust currently absorbs the highest shortening (~6 mm/yr) as it has done in the past ([?]20 km). The Ilyak fault accommodates ~5–8 mm/yr, eastward-increasing slip; rates decay sharply across the fault, suggesting a locking depth of [?]1 km—possibly creep. At least 10 mm/yr uplift and westward motion occur across the Tajik-depression–Pamir transition, including the sinistral Darvaz fault zone, likely outlining a crustal-scale ramp. The Hoja Mumin salt fountain is spreading laterally at >300 mm/yr.

Plain Language Summary

As a result of the collision of the Eurasian and Indian continent 30 million years ago, the Tethys ocean closed, and the Tian-Shan-Pamir-Tibet-Himalayan mountain ranges were created. Today the Pamir advances north, only being stopped by the Tian Shan, and thus is collapsing westward into the lower-lying Tajik depression. The (formerly) horizontal deposits of ancient marine sediments in the depression now form a series of folds and faults, running parallel to the Pamirs rim. We use ~5-years of regularly acquired satellite radar imagery and pointwise positioning data to monitor the surface-deformation rates of the whole region. The resulting rate maps visualize crustal-scale and near-surface—partly man-made—processes with an accuracy of a few millimeters and a spatial resolution of ~400 m. We show that the folds and faults are sliding on low-friction sediments like salt or gypsum, detached from the underlying basement. The sliding stops suddenly at the western end of the basin. In the basin, old salt deposits are squeezed to the surface, forming a salt fountain that spreads more than 30 cm/yr. In agricultural areas we see subsidence of more than 1 cm/yr, which might be (partially) due to unsustainable ground-water extraction.

1 Introduction

At the western end of the India-Asian collision zone, the Tian Shan, Pamir, and Hindu Kush frame the Tajik depression, hosting the Tajik basin (Figure 1a). Deformation rates derived from global positioning (GNSS) data along the northern and western margins of the Pamir facing the depression reach ~20 mm/yr (Metzger et al., 2020; Zubovich et al., 2010), being among the highest measured inside a continent. The accommodating crustal structures—thrusts and strike-slip faults—host abundant seismicity (e.g., Kufner et al., 2018; Schurr et al., 2014), including seven magnitude M7 earthquakes during the past 100 years. Structural geometries, GNSS velocities, and seismicity inside the Tajik depression suggest that a thin-skinned belt above an evaporitic decollement at 6–12 km depth—the Tajik fold-thrust belt (FTB)—is accommodating westward (lateral) extrusion of Pamir-Plateau crust (e.g., Bekker, 1996; Bourgeois et al., 1997; Gągała et al., 2020; Schurr et al., 2014; Stübner et al., 2013). Although the distribution and age of shortening is relatively well constrained geologically (e.g., Abdulhameed et al., 2020; Gągała et al., 2020), the sparse GNSS data prohibit the quantification of the contributions of the individual structures to the recent E–W shortening;

in addition, the geodetically-derived rates might be influenced by salt tectonics (Ischuk et al., 2013; Metzger et al., 2020). To assess the distribution of active slip within the Tajik FTB and the surrounding mountain ranges, a sampling method with higher spatial resolution for the active deformation is needed.

Since the launch of the European Sentinel-1 radar satellite mission in 2014, Interferometric Synthetic Aperture Radar (InSAR) data have become easily accessible and tectonically active regions are monitored every 3–12 days worldwide. The data—usually provided in single tiles—cover ~240 × 200 km on ground (Figure 1b) and allow the detection of rate changes of ~1 mm/yr (e.g., Weiss et al., 2020). Herein, we present relative displacement-rate maps for the Tajik FTB and the adjoining Pamir and Hindu Kush with a spatial resolution of ~400 m. We derive 13 individual rate maps in two independent view angles, tied to available GNSS rates in a Eurasia-fixed reference frame (Figure 1c), and decomposed into horizontal (E–W) and vertical rates (Figures 2 and 3).

We highlight and discuss the most conspicuous anthropogenic and tectonic features, and link them to the seismicity and the geologic structures formed over the last ~12 Ma. In the Tajik and Ferghana depressions, the vertical rate map outlines stripes with >15 mm/yr subsidence, with the strongest signal following the major river valleys. This subsidence is likely caused by water extraction for irrigation. The vertical uplift rates are also high at the Tajik FTB's eastern edge and the adjacent western Pamir. Together with high horizontal rates, they likely outline passive roof uplift above a crustal-scale ramp, caused by the indentation of the leading edge of the Pamir. The horizontal rate map outlines the complex 3-D geometry of an orogenic margin, with crustal material flowing laterally (westward) out of the N–S collision zone. Lateral extrusion rates increase from east to west from the eastern to the western Pamir and decrease westward across the Tajik FTB, dissipating over the salt-rooted structures. An abrupt rate change occurs across the kinematically-linked dextral Ilyak strike-slip fault bounding the Tajik FTB to the north and the Babatag thrust, the major thrust of the western FTB. The horizontal displacement rates are not affected by the vergence of the fold-thrust structures; therefore, the entire Tajik FTB is detached from its original substratum. The recent kinematics imply that the Tajik FTB is a thin-skinned belt developed above a depression-wide evaporitic decollement, whose evolution is governed by the westward advance of the outward-growing Pamir orocline.

2 Tectonic Setting

The Tajik FTB and the bounding mountain belts of the Tian Shan, Pamir, and Hindu Kush formed due to the northward advance of western promontory of the India (e.g., Burtman & Molnar, 1993; Kufner et al., 2016; Schwab et al., 2004). The 65–75-km-thick Pamir-Plateau crust (Mechie et al., 2012; Schneider et al., 2019) moves northward and collides with the Tian Shan, and at the same time collapses and extrudes westward into the Tajik depression, inverting the Tajik basin and forming the Tajik FTB (Figure 1a; e.g., Kufner et al., 2018; Nikolaev, 2002; Schurr et al., 2014; Stubner et al., 2013). The Tajik FTB comprises a series of westward-convex, ~N-trending folds and thrusts (e.g., Bourgeois et al., 1997; Chapman et al., 2017; Gągała et al., 2020) that bend in the north into the dextral Ilyak fault (Leith & Simpson, 1986); a similar—less pronounced—bending occurs in the south but no bounding strike-slip fault—akin to the Ilyak fault—has developed (Figures 2 and 3). This is compatible with the <50°, paleomagnetically-determined, anti-clockwise vertical-axis rotations in the northern Tajik FTB (e.g., Pozzi & Feinberg, 1991; Thomas et al., 1994). The Tajik FTB, southwestern Tian Shan, and Hindu Kush reflect partitioning of deformation into ~N–S shortening accompanied by dextral slip in the Tian Shan and along the Ilyak fault, ~E–W shortening in the Tajik FTB, and ~NW–SE shortening in the Afghan platform in the foothills of the Hindu Kush (Käßner et al., 2016; Kufner et al., 2018; 2021; McNab et al., 2019).

Total ~E–W shortening reaches ~148 km in the north-central Tajik FTB, with decaying values towards south (~93 km) and towards northeast into the narrow corridor between the Pamir and Tian Shan (>22 km; Gągała et al., 2020). The southeastern part of the Tajik FTB showcases salt tectonics, e.g., at the Hoja Mumin salt fountain with vertical extrusion rates of ~170 mm/yr (Leith & Simpson, 1986). The southwestern Tian Shan—the Uzbek and Tajik Gissar—constitute the thick-skinned foreland buttresses to the Tajik FTB (Figure 1a; Gągała et al., 2020). To the east, along the front of the Pamir, the Tian Shan is separated from the Pamir Plateau by the Pamir Thrust System with its leading fault, the Pamir Frontal Thrust; its western

part—in the Peter I. Range—is the dextral-transpressive Vakhsh thrust that transitions westward into the Ilyak fault (Figure 1a). In the Pamir, the ~NNW-striking, sinistral-transtensive Sarez-Karakul fault system separates the western and eastern Pamir (Figure 1a). The latter is dominated by en-bloc northward advance, whereas the former has distinct westward flow component (Ischuk et al., 2013; Kufner et al., 2018; Metzger et al., 2020).

Abdulhameed et al. (2020) estimated—based on low-temperature thermochronologic data that incorporate dates from Chapman et al. (2017) and Jepson et al. (2018)—that major shortening started at ~12 Ma, spread immediately across the entire FTB, and declined at ~9 Ma in the western FTB; reactivation concentrated in the internal (eastern) FTB with the thickest evaporates. The youngest ages (~7–2 Ma) occur along the Vakhsh thrust, i.e., the active erosional front of the northeastern Tajik FTB belt, where it narrows between the converging Tian Shan and Pamir, and along eastern edge of the FTB—at the western flank of the Pamir Plateau, dominated by the sinistral-transpressive Darvaz fault zone. The onset at ~12 Ma yields 12–8 mm/yr average long-term shortening rates in the north-central and southern Tajik FTB (see total shortening values above).

GNSS survey profiles across the Pamir's northern and western margins provide insights into the large-scale deformation and fault kinematics (Figure 1a). The highest rates were observed across the Pamir Frontal Thrust (13–19 mm/yr shortening, ~7 mm/yr dextral shear, Zubovich et al., 2010). Across the Vakhsh thrust, shortening is 15 +4/-2 mm/yr, while dextral shear increases to 16 ± 3 mm/yr; the Ilyak fault accommodates 8–15 mm/yr of dextral shear and ~5 mm/yr of shortening (Metzger et al., 2020). Kinematic modeling indicates a rather shallow fault-locking depth at the Vakhsh fault of <5 km. The rates across the Darvaz fault zone decay from north to south, i.e., from ~15 to 7–9 mm/yr sinistral shear and from ~10 to 4–0 mm/yr extension. The Sarez-Karakul fault system accommodates 5 ± 2 mm/yr sinistral slip (Metzger et al., 2017). The sparse GNSS data in the Tajik depression show that it is shortening ~ENE–WSW (Ischuk et al., 2013; Metzger et al., 2020; Mohadjer et al., 2010). The interior of the Tian Shan exhibits minor dextral shear and shortening (Figure 1a). The recent kinematics of the Uzbek Gissar and the Afghan platform are largely unresolved. In the Hindu Kush, two relatively short GNSS profiles across the NE- to NNE-striking, poorly-mapped faults indicate sinistral-transpressive motion of [?]2.5 +- 1.8 mm/yr in the central Hindu Kush and [?]7.3 +- 1.0 mm/yr in the northeastern Hindu Kush (Figure 1a; Kufner et al., 2021; Perry et al., 2018).

Abundant crustal seismicity highlights the most active faults, i.e., the Pamir Frontal Thrust, the Vakhsh thrust, the Darvaz fault zone, and the Sarez-Karakul fault system (Figure 1a; Kufner et al., 2018; Schurr et al., 2014; Sippl, et al., 2013). The earthquake focal mechanisms fit the observed fault kinematics (Kufner et al., 2018; Schurr et al., 2014). Seismicity is abundant beneath the Peter I. Range that is squeezed between converging Vakhsh and Darvaz faults, and north of the eastern Pamir, where the 2008 M_w6.6 Nura earthquake (Sippl et al., 2014; Teshebaeva et al., 2014; He et al., 2018), the 2016 M_w6.4 Sary-Tash earthquake (Bloch et al., 2019; Funning & Garcia, 2019; Vajedian et al., 2017), and the 2016 M_w6.6 Aketao/Muji earthquake (e.g., Wang et al., 2017; Feng et al., 2017) ruptured the Pamir Thrust System, respectively the Muji fault (Figure 1a). Sparse seismicity occurs in the western Tajik depression; in its eastern part, it is intense but diffuse with focal mechanisms indicating overall E–W shortening (Figure 3; Kufner et al., 2018). Most events occur at 5–25 km depth, i.e., in general below the evaporite decollement, with the overlying sedimentary stack deforming mostly aseismic (Gągała et al., 2020). The Ilyak fault appears to be mostly aseismic, apart from a cluster of seismicity southeast of Dushanbe (Figure 3; section 4.3.2). In the Hindu Kush, crustal seismicity is also sparse, suggesting that crustal faults are locked, with diffuse strain accumulation (Kufner et al., 2021).

In the context of our data analysis, a few large earthquakes stand out (Figure 1a): the 2015 M_w7.2 Sarez earthquake ruptured the central Pamir along the Sarez-Karakul fault system (Elliot et al., 2020; Metzger et al., 2017; Sangha et al., 2017); this event was in sequence with the two 2016 M6 earthquakes at the northern rim of the Pamir mentioned above (Bloch et al., 2019). The 1949 M_w7.6 Khait earthquake affected the Tian Shan region north of Peter I. Range, causing a series of landslides (Evans et al., 2009; Kulikova,

2016). In 1907, the poorly located M_s7.6 ± 0.3 Kharatag earthquake occurred somewhere at the northern rim of the Tajik depression (Kondorskaya & Shebalin, 1982) or farther east in the Peter I. Range (Kulikova, 2016; Storchak et al., 2013). The region also hosts frequent intermediate-depth earthquakes at 80–300 km depth, which are related to the ongoing indentation of Indian cratonic lithosphere beneath the Pamir and the subduction and break-off of marginal Indian lithosphere below the central Hindu Kush (Figure 1a; Sippl et al. 2013; Kufner et al., 2016, 2017, 2021). In 2015, during the InSAR data acquisition, the Hindu Kush hosted a M_w7.5 earthquake at ~200 km depth, related to slab break-off (Kufner et al., 2017).

3 Data Processing

3.1 InSAR Time-series Analysis

We used data from the Sentinel-1 satellites operating in C-Band with a wavelength of ~5.55 cm, published on the LiCS data portal as automatically pre-processed, differential interferograms (Lazecký et al., 2020): each radar scene was automatically combined with three preceding and three subsequent scenes in time, resulting in six interferometric products with temporal baselines of a couple of weeks each (assuming no time gaps). The interferograms were created with the GAMMA SAR software (Wegmüller et al., 2016; Wegmüller & Werner, 1997) and multi-looked (downsampled) to ~100 m spatial resolution. They were filtered using an adaptive phase filter (Goldstein & Werner, 1998), assuming that short-baseline interferograms contain no sudden phase changes—e.g. due to fault creep—that are naturally smeared by strong filtering. Pixels with low coherence values were masked and the data were unwrapped automatically using SNAPHU v2 (Chen & Zebker, 2002). The unwrapped interferograms were resampled and geocoded using the 1-arc-second, void-filled digital elevation model of the Shuttle Radar Topography Mission (Farr et al., 2007). Each radar scene spatially overlaps along-track with other data frames of the same acquisition time and along-range with time-independent acquisitions (Figure 1b).

Interferometric time-series analysis allows to single out the small, secular tectonic and/or anthropogenic signals from of the interferometric noise. This is done frame-wise (Figure 1b) by spanning a network of all interferometric scenes of one radar frame (Figure S1 of the supporting information). We used a modified small-baseline approach (NSBAS, López-Quiroz et al., 2009; Doin et al., 2011), as implemented in the python code LiCSBAS (Morishita et al., 2020) that directly integrates LiCS interferograms. Tropospheric noise was suppressed using synchronous tropospheric delay maps, which are based on extrapolated weather data of the European Centre for Medium-Range Weather Forecasts in a horizontal resolution of 0.125°, updated every six hours (Yu et al., 2018). We automatically excluded interferograms from further processing, if they contained sparse or noisy data or did not pass a phase-loop closure test indicating severe unwrapping errors. The most stable pixel over time was selected as a reference pixel (red stars in Figures S2a and S2b). The whole interferometric network was then inverted for incremental displacements between the acquisition dates, with the mean displacement velocity being derived from the cumulative displacements by least-squares (Morishita et al., 2020). Network gaps were overcome by adding a linear constraint with a scaling factor to the Green's functions (Doin et al., 2011). The standard deviation of the inverted rates was obtained by percentile bootstrapping (Efron & Tibshirani, 1986). The uncertainties are usually underestimated, particularly if the network is not fully connected (Morishita et al., 2020). The resulting rate maps are masked by several quality assessment criteria, such as interferometric coherence, amount of data, rate standard deviation, time period covered, number of network gaps, or unwrapping errors, or root-mean-square of rate residuals. Finally, the maps were high-pass filtered in time and low-pass filtered in space using a Gaussian filter kernel (Hooper et al., 2007).

We processed six overlapping frames in ascending flight mode and seven frames in descending flight mode of three adjacent satellite tracks (Figure 1b). The assembled dataset covers 270,000 km^2in both view angles, stretching north-south from the Ferghana depression to the Hindu Kush and west-east from the Tajik depression to the eastern Pamir (Figure 2). Before 2016, data acquisition occurred irregularly and only few interferograms of poor quality are available. In the Pamir, many frames show co- or post-seismic displacements related to the 2015 M_w7.2 Sarez earthquake (Metzger et al., 2017). In this region, we used only data acquired one year or more after the earthquake (Figure S1). Overall, each frame contains 255–500

interferograms of 82–175 radar images spanning 2–6 years (Table S1). To increase the processing speed, the interferograms were downsampled by 4x4 block averaging to a ground resolution of ~350 m in range and ~450 m in azimuth. After quality assessment, the remaining 50–110 scenes spanned a network of 120–350 interferograms (Table S1). The rates resulting from the time-series analysis were masked using standard threshold parameters, i.e., an average coherence of >0.05, a rate standard deviation of <100 mm/yr, <10 network gaps, and a spatio-temporal consistency of at least 5 mm. Some of these parameters were modified individually after a visual inspection (Table S2). After the multi-looking and atmospheric correction procedures, we repeated each processing step iteratively, removed poor interferograms, or corrected unwrapping errors manually. This improved the data quality, in particular in the rugged western Pamir, where the rates are most difficult to retrieve. The spatio-temporal filter was set to three times the average sampling interval in time and 2 km in space. Topography-related phase signals were suppressed using a linear correction term estimated between 200 and 10,000 m elevation.

The completeness of the resulting rate maps correlates with topographic roughness (Figures S2a and 2b). While the Tajik depression and the arid eastern Pamir Plateau exhibit a relative high coverage, the deeply incised western Pamir, Tian Shan, and Hindu Kush are mostly void, apart from flat-bottom, formerly glaciated valleys (e.g., Stübner et al., 2017). The obtained deformation rates range between ±15 mm/yr in line-of-sight (LOS) relative to their respective local reference points (red stars in Figures S2a and 2b). Due to data sparsity, the standard rate deviation of the descending frame 005D_053 (Figure S2b) is significantly larger than those of the other frames; we excluded this frame from further processing. The rate uncertainties are between 0.5 and 3.0 mm/yr, with higher uncertainties in the descending acquisition geometry (Figure S3). The highest uncertainties are observed in the Panj valley in the western Pamir and south of the Hindu Kush, where either the topography or a poorly-resolved elevation model foster unwrapping errors. We excluded the area south of the Hindu Kush from further processing, as it also lacks stabilizing GNSS information. The lowest uncertainties are found near the center of each frame at the location of the reference points. These uncertainties only reflect a lower boundary, as they do not take into account atmospheric disturbances or systematic biases caused by spatial subsampling and soil-moisture variations, which are most problematic in interferograms with a short temporal baselines (Ansari et al., 2021; De Zan et al., 2014), as we further discuss in section 4.3.1. Such biases can be suppressed to some extent if long-baseline interferograms are included in the interferometric network, and full resolution data are processed, which was not applicable in our case. However, we qualitatively estimated the spatial footprint of these biases by the phase-loop closure technique: for each frame, we calculated the mean of closed phase loops, that is, the sum of the interferometric phase difference $\varphi_{ij} + \varphi_{jk} - \varphi_{ik}$, between three acquisition epochs i , j and k , which is supposed to be zero (De Zan et al., 2015). If several of these loops are averaged, a systematic phase bias becomes apparent (Figure S4). For each frame, we calculated and averaged 70–90 phase loops acquired during 2017 to 2020. Significantly, mostly negative phase bias is observed in the Tajik and Ferghana depressions, and the extent of the affected regions is spatially well defined.

Thanks to the dense temporal sampling of the Sentinel-1 radar mission, the outcome of our time-series analysis cannot only be used to derive linear rates, but also to monitor temporal rate anomalies, induced by seasonal processes (Figure S5) or smaller earthquakes (see discussion in chapter 4.3.2). Thus, the noise level and temporal information in InSAR time-series nearly reach the one of daily GNSS time-series, but clearly outperform them in terms of spatial coverage.

3.2 Reference Frame and LOS Rate Decomposition

We collapsed all LOS rate maps with their individual stable reference points (red stars in Figures S2a and S2b) into a supra-regional Eurasia-fixed reference frame, using published survey-mode GNSS data (Ischuk et al., 2013; Kufner et al., 2021; Metzger et al., 2019, 2020, 2021; Mohadjer et al., 2010; Zubovich et al., 2016). During this first processing step, we identified and excluded four GNSS rates in the Tajik depression as outliers (white arrows in Figure 2a). Next, we tied each rate map into the Eurasia-fixed reference frame: we applied a linear ramp to each map to optimize (1) the fit to the horizontal GNSS rates within a search radius of ~4 km (or 10 pixels), and (2) the along-track overlap of two data frames (Ou, 2020) by inverting an

over-determined, weighted design matrix, where the GNSS rates were collapsed into LOS (more details are given in the supporting information section S1). After removal of the GNSS outliers, we added seven artificial data points (black squares in Figure 1c) to stabilize the frames covering the southern Hindu Kush, where GNSS data are sparse. Their rates were interpolated from the adjacent stations and their uncertainties were doubled. The individual rate maps descending track 078 and 005 were not fitted to match the along-track overlay, because the data in the overlap area were either too sparse or the deviation was abnormally large (Figure S2b). The resulting rates (Figures S2c and 2d) contain significant offsets across-track, which are mostly due to the sudden LOS change (Figure S6). The westward motion of the western Pamir dominates the ascending rate maps (Figure S2c) with positive values and the descending rate maps (Figure S2d) with negative values. Due to the right-looking acquisition geometry of the Sentinel-1 satellite, the data are sensitive to about 40, 10, and 50 per cent of the full east, north, and vertical displacement signals. If observations are available from ascending and descending LOS, they can be decomposed (Wright et al., 2004) into east and subvertical components, using a weighted inversion. The subvertical component contains a minor north component, which can be suppressed by subtracting interpolated north rates based on independent GNSS rates (Figure 1c; Ou, 2021).

The resulting displacement rates in the east map agree with the corresponding GNSS data (Figure 2a) and range between -20 to +10 mm/yr in the ITRF2014 Eurasia-fixed reference frame (Altamimi et al., 2017). The vertical rates are in a data-centered reference frame and embrace ±18 mm/yr (Figure 2b). The rates are most coherent in the Tajik and Ferghana depressions and—to some extent—in the eastern Pamir and the Alai valley. Rates in the western Pamir could only be extracted along the Panj-river valley and some of its tributaries. We still observe long-wavelength extrema at the corners and edges of some frames, e.g., in the NW-corner of frames 071A_054 and 100A_050 or the SW-corner of 078D_052 (Figures 1b; markers "1" to "3" in Figure 2a). They are probably due to significant atmospheric contributions in radar scenes, which are used uni-directional, that is, *only* as primary or secondary scenes. The spatial data coverage decreased further after decomposition (Figure S2) to regions covered by both view angles only. The decomposed rate uncertainties—now including the GNSS data uncertainties—are in the range of 0.6–2.6 mm/yr (Figures S7 and S8). In a similar study on Anatolia—with slightly more data, the uncertainties are in the range of 2–3 mm/yr for wavelengths of 50–150 km and a 5-year-long time-series (Weiss et al., 2020; see Figure S7). For our slightly sparser dataset, we assume that local rate changes are significant, if >1.5 mm/yr, and long wavelength signals are significant if >3–5 mm/yr. These estimates are probably still too optimistic for the Panj-river valley, where the interferometric networks are short in time and repeatedly sub-divided, impeding the correct assessment of linear rates (Figure S1), or where too few GNSS data points are available (Hindu Kush). There, the decomposed rate uncertainties are significantly higher than in the rest of the dataset and reach up to 4.5 mm/yr.

The individual ascending and descending rate maps and the final decomposed east and vertical rate maps, both stable to Eurasia (Altamimi et al. 2017) are available as geo-referenced TIF-files in the supplementary information.

4 Results and Discussion

4.1 Rate Map Quality Assessment

Interferometric radar analysis is challenged by several factors. Seasonal vegetation change and (ground) water dynamics introduce a bias, if only short temporal baseline interferograms are used (Figure S4; Ansari et al., 2021), or if the network density is not equally distributed throughout the seasons. Heavy snowfall causes interferometric decorrelation, which may apply in particular for the western Pamir. The partially incomplete digital elevation model (Farr et al., 2007) of the deeply-incised western Pamir and southern Hindu Kush contains topographic artifacts, which makes interferograms prone to unwrapping errors. Given these obstacles, our LiCSBAS rate maps contain isolated data patches due to spatial and temporal decorrelation (Figure S2), which challenges the combination of the observed rates of several independent acquisition frames into one single reference frame. We overcame this to some extent by tying the rates to the GNSS reference frame, but some sharp jumps along frame boundaries remain; these are in the Afghan platform, the western

Ferghana depression, the Dushanbe trough north of the Ilyak fault, and the upper Panj valley (markers "1" to "4" in Figure 2a, respectively). Also, the horizontal rates of ˜0 mm/yr observed in the Muksu-river valley in the northern Pamir (Muksu in Figure 2a) are difficult to interpret. Thus, abundant GNSS data are fundamental to correctly transform LOS rate maps into a supra-regional reference frame. For example, the sparse GNSS data in the Hindu Kush do not suffice to stabilize the observed LOS rates correctly—particularly in the region south of the Hindu Kush—and we can only speculate if the long-wavelength signals are rooted in tectonics (Figures 2a and S2).

On a local level, the independent LiCSBAS rate maps offer reliable data to identify km-scale mass movements, which are abundant in this region, but these signals should be confirmed by optical imagery and/or fieldwork. We encourage the reader to make use of the supplementary material for their own specific analyses, as this task exceeds the scope of this paper. When interpreting our results, one must consider the different time periods of data collection (Figure S1). Each individual LOS rate map might be differently affected by moderate-sized earthquake signals or season-dependent near-surface dynamics. The Tajik depression yielded the highest data resolution in space and time, where we have both, dense data and distinct tectonic and non-tectonic signals that can be correlated with independent structural data in high-resolution. We therefore discuss the observations from the Pamir and Hindu Kush in a reconnaissance way and focus on the Tajik depression, in particular the Tajik FTB.

4.2 Pamir and Hindu Kush

In the Eurasia-fixed reference frame, the InSAR rates exhibit westward motion in the order of [?]10 mm/yr in the western Pamir and the Tajik FTB with a good match to the GNSS-derived east rates (Figure 2a). We assign the large-scale west-directed surface displacements to the westward collapse and lateral extrusion of the Pamir-Plateau crust. North of the Pamir-Tian Shan collision boundary, the Ferghana depression appears relatively stable, as all significant features in the rate maps also appear in the phase-bias map (Figure S3) or collocate with radar frame boundaries (marker "2" in Figure 2a) and hence are artifacts. Along the northern front of the Pamir in the southern Alai valley ("Alai" in Figure 2a), sharp rate changes record the westward-increasing dextral shear at the leading edge of the Pamir, indicating its escape towards the west in addition to the dominant N–S shortening showcased by the GNSS data (Zubovich et al., 2010, 2016). The east-rate map also indicates that part of the active deformation steps back south of the eastern Alai valley from the Pamir Frontal Thrust and connects to the ˜WNW-striking Muji fault (Figure 2a). It remains indistinguishable whether the recorded displacement rates reflect post-seismic activation following the 2016 Sary-Tash and Muji earthquakes (Bie et al., 2018; Feng et al., 2017) or are a long-term signal. Afterslip and relaxation can be excluded, since we excluded data acquired in (at least) the first six months after these two M6 events. In any case, the indicated rates support the transfer of the top-to-west normal slip along the Kongur Shan extensional system of the eastern Pamir (e.g., Robinson et al., 2004; 2007; just outside and southeast of the eastern boundary of Figure 2) via the Muji fault and the Kyzilart transfer zone (marker "a" in Figure 2a) to the Pamir Thrust System and in particular to the deformation front along the Pamir Frontal Thrust (Sippl et al., 2014). The existence of this dextral transfer zone, consisting of the Muji fault and the faults of the Kyzilart transfer zone, that transfer ˜E–W crustal extension along the Kongur Shan system to the dextral strike-slip component along the Pamir front, is also implied by the slight divergence of the GNSS velocity field between the eastern Pamir (e.g., Lake Karakul area in Figure 2a) and the Tarim block (Zubovich et al., 2010); north of the transfer zone the GNSS vectors parallel those in the Tarim basin, albeit with much lower rates, reflecting the shortening across the multiple faults of the Pamir Thrust System (Figure 2a). The dextral transfer zone (Muji fault and faults of the Kyzilart transfer zone) implies that the eastern Pamir was involved in the convergence partitioning, here with a westward flow component smaller than that of the western Pamir.

At the northwestern rim of the Pamir, along the Vakhsh valley, sharp east-rate changes of 12–24 mm/yr either imply high landslide activity or—more likely—a shallow locking depth of the evaporite-rooted, dextral-transpressive Vakhsh thrust; the estimated dextral strike-slip rates are 16 +- 3 mm/yr (Metzger et al., 2020). If the Vakhsh thrust is nearly freely creeping, the 1949 M_w7.6 Khait earthquake likely did not rupture the

Vakhsh thrust but a structure in the crystalline basement of the Tian Shan.

On first order—and given that the rates measured in the valleys of the Panj and its tributaries are significant, the horizontal rates appear to increase from 5–15 mm/yr westward motion in the eastern Pamir (east of the Sarez-Karakul fault system) to 15–20 mm/yr in the western Pamir; this conforms with the GNSS data (Metzger et al., 2020), and the intense western Pamir seismicity with focal mechanisms that show strike-slip and normal fault solutions with ˜E-trending T-axes (Schurr et al., 2014). A minor westward rate increase occurs across the distributed segments of the Sarez-Karakul fault system, e.g., near Lake Sarez (Figure 2a). The implied extensional deformation component accommodated by the Sarez-Karakul fault system agrees with the geological observations of major range-bounding normal faults northeast of Lake Sarez (Officers Range, marker "OR" in Figure 2a; Rutte et al., 2017; Schurr et al., 2014) but contrasts with focal mechanism solutions, which record nearly pure sinistral strike-slip (Metzger et al., 2017; Schurr et al., 2014). However, many short wavelength rate changes correlate with slopes and the systematic bias map (Figure S4). We suspect that this is not a topographic artifact but rather caused by seasonal, permafrost-related sagging of (or pore-pressure changes in) unconsolidated material (e.g., Rouyet et al., 2019); we extensively mapped such features that formed as a result of the 2015 Sarez earthquake (Figure 2a shows the modeled rupture trace from Metzger et al., 2017).

The northeastern Hindu Kush of Badakhshan (Figure 1a), with reliable data along the Kokcha-river valley (marker "b" in Figure 2a), exhibits nearly as high westward rates (7–12 mm/yr) as the eastern Tajik FTB (8–15 mm/yr) and the western Pamir (marker "c" in Figure 2a, 16–26 mm/yr). No modern structural information is available for the faults and folds mapped in the northwestern Hindu Kush, but the highest rate changes coincide with thrust-cored folds along the southeastern margin of the Tajik FTB, involving Pliocene strata (Figure 3a; Doebrich & Wahl, 2006; own unpublished mapping). In contrast, the western Hindu Kush—including the Afghan platform—appears to be horizontally mostly stable with respect to Eurasia (west of marker "b" in Figure 2a, 0 +- 2 mm/yr).

We observe strong uplift of 10–17 mm/yr in the westernmost Pamir (along the Panj valley and west of it), and easternmost Tajik FTB where its eastern erosional edge is cut by the Darvaz fault zone (marker "d" in Figures 2b and 3b); this area coincides with the area of rapid westward motion (marker "c" in Figure 2a; see interpretation below). A N–S gradient—with uplift rates of 4–6 mm/yr—occurs at the southern margin of the Tajik depression at its transition to the Afghan platform (marker "e" in Figure 2b). This area south of the Amu Darya–Panj-river valley, marks the interaction and transition from the ˜E–W shortening of the Tajik FTB to the ˜NW–SE shortening within the Afghan platform, implied by earthquake focal mechanism (e.g., Supplementary Figure S5 in Kufner et al., 2021; McNab et al., 2019), and the appearance of ˜E-striking faults, e.g., the dextral-oblique thrust in the Alburz-Marmul fault zone (Figure 1a).

The whole northeastern Hindu Kush and southwestern Pamir are located above steeply-dipping lithospheric slabs; their position in the mantle is outlined by the intermediate-depth earthquakes in Figures 1a and 2a (e.g., Kufner et al., 2016, 2017, 2021; Zhan & Kanamori, 2016). The Pamir slab starts to bend down from west to east beneath the eastern Tajik FTB (Figures 6 and 7 in Schneider et al., 2019; crustal-scale cross section in Figure 18c of Gagała et al., 2020) and likely laterally terminates in the south where strong uplift (marker "d" in Figure 2b) gives way to subsidence in the northeastern Hindu Kush (marker "f" in Figure 2b). The Hindu Kush slab is subducting northward, dips steeply north to vertical, and is in the process of stretching and tearing in its eastern part (Kufner et al., 2017, 2021). The boundary between the mantle parts of the two slabs is clearly outlined by the intermediate-depth earthquakes in the southwesternmost Pamir (Hindu Kush slab: purple dots; Pamir slab: pink dots in Figure 2). It is difficult to assess, whether these deep-seated processes are reflected in our rate maps. InSAR radar satellite antennas are most sensitive to vertical motions, but subtle rate changes across several tens—if not hundreds of kilometers—are challenging to correctly retrieve. Our observation of regional, 0–4 mm/yr subsidence of the northeastern Hindu Kush (marker "f" in Figure 2b) above and north of the Hindu Kush slab, and in particular the marked contrast to the 10–17 mm/yr uplift in the easternmost Tajik FTB (marker "d" in Figure 2b) likely record these lithosphere processes. The region where the crust of the Tajik depression bends down, forming the footwall

of the western Pamir (crustal scale buckling in profile along latitude 38°N in Figure 6 of Schneider et al., 2019; Gagała et al., 2020), likely constitutes a crustal-scale antiform about a ramp, causing uplift. It possibly induces subsidence in the southwestern Pamir where the back-rolling Pamir slab is vertical (Kufner et al., 2016). The north-dipping to subvertical, back-rolling Hindu Kush slab possibly induces the subsidence in the Hindu Kush (marker "f" in Figure 2b): there, subsidence of up to 4 mm/yr changes to uplift at the western end of the slab where it is intact (boundary between markers "e" and "f") and subsidence possibly changes to modest uplift at the slab's eastern end, where the break-off has progressed most (Kufner et al., 2021). We interpret the pronounced patches of 20–40 mm/yr subsidence south of markers "e" along the Kunduz-river valley as anthropogenically-caused (Figure 2b; see section 4.3.1 for equivalent subsidence along the valleys of the Tajik depression). We interpret the general [?]10 mm/yr subsidence south of marker "f" and south of the eastern part of marker "e" as a tectonic signal caused by the Hind Kush slab; there, Kufner et al. (2021) tomographically mapped its down-bending towards its subvertical position in the mantle marked by the purple earthquakes.

4.3 Active Structures in the Tajik Fold-thrust Belt

The rates in the Tajik FTB are interpreted in combination with seismicity (Kufner et al., 2018) and the structural geometries, derived from surface, seismic, and borehole data (Gagała et al., 2020). In addition to the map view (Figure 3), we projected the horizontal and vertical rates onto four geological cross-sections within 5 km swaths (Figures 4a and 4b; cross-section traces in Figure 3), and into a detailed east-rate map and an oblique-crossing profile of the Ilyak fault (Figure 5; frame in Figure 3a). In addition, we compared the rates to topographic profiles and percentage of arable land, both computed within 5 km swaths (Figures 4a and 4b).

4.3.1 Non-tectonic Signal

Herein, we outline the non-tectonic signal, that is systematic subsidence, by land classification data based on Landsat 8 optical imagery (MDA US BaseVue, 2013); land classified as arable correlates well with the systematic soil-moisture bias map (Figure S4). We marked the major agricultural areas by polygons framed thick-white (Figure 3b) respectively shaded in green (Figures 4a and 4b). The vertical rate maps of Figures 2b and 3b outline stripes with >15 mm/yr subsidence as the most outstanding feature of the Tajik depression; the strongest subsidence signal follows the major river valleys of the Tajik depression, which host intense agriculture. The observed subsidence is most likely caused by precipitation-induced soil-moisture changes (Ansari et al., 2021; De Zan et al., 2014). Rainfall causes rapid pore filling and simultaneous soil uplift (Gabriel et al., 1989), which often leads to unwrapping errors in interferograms. The consequent, slow dehumidification (see, e.g., Figure 2 of Albertson & Kiely, 2001), on the other hand, is correctly imaged in interferograms, thus biasing the vertical rates derived from the time-series analysis towards the negative. This bias could be enhanced by water extraction due to the extensive irrigation in the summer months, during which most of the used radar scenes were acquired; a more detailed study of these signals lies beyond the scope of this work. In the horizontal rates, the agricultural areas often coincide with a high measurement scatter, although without any systematic component. A second conspicuous vertical signal—but this time positive—is correlated with major rivers and related to water level increase during hinterland snow melt (e.g., marker "g" in Figure 3b). The distinct, patchy subsidence in the region between the fossil and active (Hoja Mumin) salt diapirs in the southeastern Tajik FTB and the Nurak water reservoir (markers "HM" and "NR" in Figure 2b) may be an affect of salt tectonics (Figure 11 of Gagała et al., 2020). But it is also correlates to arable land that has not been properly classified in the Landsat 8 data.

The highest deformation rates occur at the Hoja Mumin salt fountain, where we observed local uplift of ˜50 mm/yr at its top, surrounded by up to ˜120 mm/yr of subsidence and lateral outflow of ˜350 mm/yr to the west and ˜170 mm/yr to the east. These rates confirm the recent activity of this salt fountain, as documented by Leith & Simpson (1986), Dooley et al. (2015), and Gagała et al. (2020). We also observed localized uplift at the shores of the Nurak reservoirs (and smaller reservoirs downstream; marker "NR" in Figure 2b and cross-sections A and B in Figure 4a) that is probably related to elastic rebound caused by reservoir-volume changes, as observed elsewhere (e.g., Cavalié et al., 2007; Neelmeijer et al., 2018).

4.3.2 Tectonic Signal

The unambiguous horizontal tectonic signal consists of long-wavelength trends. Foremost, the bulk of the Tajik FTB accommodates westward motion (map view in Figure 3a, cross-sectional view in Figures 4a and 4b). Characteristically, the horizontal displacement rates are not affected by the vergence of the fold-thrust structures in the Tajik FTB; in particular, the Yavan synclinorium—the zone of vergence change—is showing similar horizontal rates as the bounding Kafirnigan and Vakhsh anticlinoria. Therefore, the Yavan synclinorium must be—at least at present—entirely detached from its original substratum. Chapman et al. (2017) postulated that the east-vergent western Tajik FTB is part of the greater Tian Shan orogenic system, distinct from the eastern Tajik FTB whose shortening is linked to the Pamir, with the Yavan synclinorium being a remnant foreland common to both fold-thrust systems; again—at least at present—the west-directed rates indicate the detachment of the entire Tajik FTB as part of the outward-growing Pamir orogenic system.

The west-directed displacement rates decay away from the Pamir: Figure 3a shows—in average—higher westward displacements in the part of the Tajik FTB adjacent to the Pamir than away from it. Cross-sections B and C in Figures 4a and 4b illustrate this pattern (envelope 'A' in the horizontal displacement profiles), while in cross-sections A and D this trend is not convincing. We interpret this decrease by the gradual dissipation of the west-directed motion across the salt-rooted structures; however, this effect is subordinate to the coherent westward displacement of the whole Tajik FTB. The rates decrease and become less systematic towards south (cross-sections A–C versus D; Figures 4a and 4b), suggesting active, northward-increasing, anti-clockwise vertical-axis rotations in the Tajik FTB, in agreement with the sense of past rotations evidenced by paleomagnetic data (Pozzi & Feinberg, 1991; Thomas et al., 1994).

In detail, the horizontal displacement profiles often show a saw-blade pattern (Figures 4a and 4b). These short-wavelength perturbations stand out across the Kafirnigan anticlinorium, where positive spikes—reaching up to 10 mm/yr above the regional background—are centered over scarp slopes of east-facing hogback ridges ("E" markers placed over the horizontal displacement profiles in cross-section A–C; Figures 4a and 4b). Figure 6a highlights these short-wavelength anomalies in a high-pass filtered map of horizontal rates that suppresses the regional component: the east-facing scarp slopes ("E" markers) show narrow but pronounced positive, the west-facing slopes negative, albeit less pronounced horizontal displacement anomalies. The divisions between the local positive and negative anomalies follow the crests of the topographic ridges, suggesting divergent ground motions across the ridge crests. We interpret the short-wavelength saw-blade patterns—superimposed on the regional displacement profiles—as related to gravitationally-induced mass movements (slope sagging or creep). Due to the homoclinal structure of the hogback ridges in the Kafirnigan anticlinorium, the east-facing scarp slopes incise older strata, including mass-movement prone Cenomanian-Campanian shale, marl, limestone, and evaporites, while the west-facing ones follow sandstone- and conglomerate-dominated Oligocene-Neogene strata with less mass-movement susceptibility; this likely causes the faster ground motion on eastern than western slopes. Figure 6b provides structural evidence for northwest-directed mass movement, albeit without age control: along a steeply west-dipping slope in the ˜NW-dipping strata of the Karshi anticline—east of the Babatag anticline, an Upper Cretaceous shale-gypsum sequence shows dominantly ˜NW-directed normal faulting, with the faults planes and numerous tension gashes infiltrated/lubricated by gypsum.

Across the frontal anticline of the Vakhsh anticlinorium, where the hogback ridges face west due to the change of the structural polarity across the Yavan synclinorium, this relationship seems to be reversed: there, the west-facing scarp slopes ("W" markers in cross-sections B and C of Figures 4a and 4b; Figure 6a) correlate with negative displacement spikes. This indicates that a local west-directed displacement component adds up to the regional displacement. We propose the same explanation as for the Kafirnigan anticlinorium, i.e., variable susceptibility of the slopes to mass movements; however, the relationship is more diffuse in the Vakhsh than in the Kafirnigan anticlinorium, possibly due to the complex surface geology, in particular the presence of incised hanging-wall anticlines.

An abrupt ˜5 mm/yr change in the horizontal displacement rates occurs across the Ilyak fault and the Babatag thrust (Figures 2a, 3a, 4a, and 5). The Babatag thrust accommodates an abrupt arrest of the Tajik

FTB's westward motion. It is the most prominent structure of the Tajik FTB in terms of the amount of shortening with total displacement exceeding 20 km over the past ~12 Ma in its northern segment; total displacement drops to ~10 km in the south (Gagała et al., 2020). The horizontal velocity contrast across this thrust is ~5 mm/yr all along strike, although the velocity gradient in the north (cross-sections B and C, Figures 4a and 4b) is higher than in the south (cross-section D). The absolute numbers indicate a passive hanging wall and actively underthrusting footwall. The dip of the Babatag thrust—constrained by boreholes—is ~15° (Gagała et al., 2020), hence, the horizontal underthrusting at ~5 mm/yr should resolve in ~1.3 mm/yr vertical displacement of the hanging wall; such an uplift anomaly is not evident, probably due to its low value compared to the noise. Recent activity of the Babatag thrust may independently be indicated by geomorphology: Figure S9 shows a series of 500-m-wide swath profiles along selected stream trunks. Most of the profiles display knickpoints, possibly indicating topographic perturbations due to slip along the Babatag thrust; the most affected stream profiles (2, 3, 5 in Figure S9) face an exposed portion of the Babatag thrust where it overrides Quaternary alluvia. However, due to the resolution of the current-state of geological mapping (scale 1:200,000), we cannot assess the effect of lithological changes on the position of the knickpoints in detail.

Cross-section A in Figure 4a shows and Figure 5 details the transition of the Tajik FTB to the Dushanbe trough, which is involved in the moderate ~N–S shortening of the Tian Shan to the north (Käßner et al., 2016; Gagała et al., 2020). Figure 5 shows the structures, seismicity, and east-rate changes across the Ilyak fault southeast of Dushanbe, where the fault exhibits a horizontal rate change within a corridor of [?]4 km. In an elastic screw dislocation model, 50 % of the fault's relative motion should occur in a corridor of twice its locking depth (Savage & Burford, 1973); this would suggest that the fault is locked at <1 km depth, if not—given the spatial sampling of ~450 m and the strong filtering of the original interferograms—freely creeping as suggested by InSAR LOS rate maps produced by higher spatial sampling (Wilkinson et al., 2020). Dextral slip varies along strike and decreases from ~10 mm/yr in the east to ~5 mm/yr in the west (Figures 5a and 5b). Seismicity is sparse except for an area ~20-km west of Dushanbe, where the focal mechanisms suggest dextral shear (Figure 5a; Kufner et al., 2018). This is where the fault changes strike and several thrusts of the Kafirnigan anticlinorium enter the Ilyak fault, forming transpressive shear lenses, imbricating Lower Cretaceous to Pliocene rocks.

We have no direct structural information on the Ilyak fault, mostly due its strong anthropogenic overprint. The data at the three sites in Figure 5c characterize the northern edge of the Dushanbe trough and the Vakhsh anticlinorium south and north of the Ilyak fault. Pure top-to-south thrusting emplaced the crystalline basement of the Tian Shan on Cretaceous limestone at station 1893A at the northern rim of the Dushanbe trough; the age of thrusting is unknown but younger than ~10 Ma (Käßner et al., 2016). The lack of a strike-slip signal supports our earlier interpretation that the band of westward displacement signal, coinciding with a series of thrusts farther east, is an artifact (marker "3" in Figure 2a). The ~NE-striking fault east of Dushanbe, well-expressed topographically and forming a clear boundary between agricultural and pastural land, appears to accommodate westward displacement rates of up to 5 mm/yr. The two sites (Figure 5c) in the Vakhsh anticlinorium south of the Ilyak fault characterize that part of the Tajik FTB where the overall ~N-striking thrusts progressively bend into the Ilyak fault zone. Characteristically, the thrusts have dextral-transpressive top-to-(N)NW kinematics; these faults accommodate horizontal rate changes of a few mm/yr. Our data neither support nor disprove the hypothesis that the 1907 M_s7.6 ± 0.3 Kharatag earthquake occurred on a locked fault near Dushanbe (Kondorskaya & Shebalin, 1982).

An obvious but small active structure is a ~N-striking fault south of the conjunction of Vakhsh, Panj, and Kunduz rivers that exhibits frequent seismicity and where the hanging wall exhibits increased west-directed motion (marker "h" in Figure 3). Its surface trace reaches a length of ~15 km but may be connected with a similar structure north of the Amu Darya, also hosting a cluster of seismicity and two focal mechanism solutions that indicate slip along ~N-striking subhorizontal planes (Kufner et al., 2018). The original time-series of a pixel selected in the hanging wall captured about ~3 cm of slip towards ascending LOS after a 2017, January 9, M_w5.2 earthquake (event 201701090559A, Ekström et al., 2012; Figure S5). Our kinematic observations are in agreement with the double couple solution from the Global Centroid Moment Tensor

catalog that reports thrusting on a ˜46°-dipping plane on a ˜SSE-striking fault (marked in orange and labeled by magnitude; Figure 3). The epicenter, however, is ˜15 km west of the cluster of earthquakes (Kufner et al., 2018). We consider the structure to be part of the southernmost Kafirnigan anticlinorium, where it bends from a ˜N to a ˜SE strike, marking the southern margin of the Tajik FTB.

Extremely rapid westward motion occurs west of the Darvaz fault zone, at the eastern erosional edge of the Tajik FTB, where westward rates reach 16–26 mm/yr (marker "c" in Figures 2a; Figure 3a; markers "I" in Figure 4a); these high rates can be observed from the Peter I. Range in the north all the way to west of the Kokcha river in Badakhshan in the south, interrupted by a relatively stable area and with pure signal along the Panj valley. Vertical uplift rates also increase towards the Darvaz fault reaching 10–17 mm/yr (marker "d" in Figure 2b; envelopes B in Figures 4a and 4b; see section 4.2). The area of rapid uplift coincides with high topography, developed in often weakly-consolidated Neogene coarse-grained terrestrial strata (Figure 4, topographic swath profiles). From our uncertainty analysis (Figures S4, S7, and S8), we can exclude atmospheric or near-surface contributions to these rates, thus they are of tectonic origin. Both the high horizontal rates and the Pamir-ward increase of the vertical uplift rates support the earlier given interpretation (section 4.2) of a tectonic stack above a ramp, caused by ongoing indentation of the leading edge of the Pamir below this marginal part of the Tajik depression, resulting in a passive roof uplift. This, however, appears inconsistent with the modern sinistral kinematics of the Darvaz fault (Kufner et al., 2018; Metzger et al., 2020). We favor an interpretation of slip partitioning, with top-to-WNW thrusting of the Pamir's buried leading edge being kinematically decoupled by the sinistral Darvaz fault from the Pamir hinterland. We envision a similar displacement partitioning as described for the deformation at the northern edge of the Pamir, east of the Alai valley (section 4.2): there, dominant northward motion is accommodated by the large thrusts of the Pamir Thrust System (with the recent Nura and Sary-Tash earthquakes) and subordinate dextral strike-slip faults, the Muji fault and the Kyzilart transfer zone (with the recent Muji earthquake), that accommodate the westward escape of the Pamir. In this scenario, the thrusts and strike-slip faults at the eastern edge of the Tajik FTB would partition deformation in northward motion along the Darvaz fault zone (and parallel faults in the western Pamir) and westward motion along the thrusts.

If significant, the westward acceleration of the horizontal rates west of the Darvaz fault zone (marker "c" in Figures 2a) would imply ongoing extension along the eastern border of the displacement anomaly and concomitant shortening along its western border, a pattern typical for gravity-driven deformation. Past extension is indeed evidenced by likely Neogene graben fills in the Darvaz fault zone (Gagała et al. 2020), but we are lacking structural and geomorphic data to confirm that such a process is operating today. We interpret the eastern edge of the Tajik FTB as the western margin of the province with strike-slip and normal fault focal mechanisms that indicate ˜E–W extension across the western Pamir (Schurr et al., 2014). The westward accelerating rates may indicate the zone where the crust of the topographically-high western Pamir Plateau acquires a component of westward gravitational sliding being transferred from the crustal ramp to the salt-décollement of the Tajik FTB.

There is a conspicuous westward horizontal rate increase of up to 7 mm/yr across a ˜NNE-trending watershed between the Panj and the Kokcha rivers that seems to be a true kinematic signal (marker "j" in Figures 2a and 3a); towards east, rates increase again to ˜8 mm/a westward movement (southern extension of marker "c" in Figure 2a), which we interpreted above as due to a component of westward gravitation sliding along the at the western margin of the Pamir Plateau. The boundary of accelerated westward motion at marker "h" coincides with the transition from the west-vergent thrust-folds with thick Neogene hanging-wall strata to the area in the southeastern Tajik FTB that is governed by salt-tectonics (marker "H" in cross-section D of Figure 4b). The box-shaped antiform with a >25-km wavelength, cored by up to 5-km-thick evaporites and a salt diapir at its western tip west of marker "H", may indicate a zone of enhanced westward flow feeding the various thrusted detachment folds with thick evaporite cores farther west. This indicates that parts of the buried salt structures of the southeastern Tajik FTB may—besides the Hoja Mumin salt fountain—are active; the strong anthropogenic overprint prohibits an interpretation of the vertical displacements but as in the area between the Nurak reservoir and Hoja Mumin salt fountain, the subsidence signal features a distinct, patchy pattern.

5 Conclusions

The interferometric rate maps of the greater Pamir area exhibit large-scale tectonic features, ground subsidence due to water level changes, salt tectonics, and mass movements. Rate interpretation is limited by data sparsity of the underlying interferometric network in time and space. Single interferograms of poor quality might significantly influence the 13 derived relative rate maps in LOS. The GNSS data play a key role to correctly tie the rate maps to a supra-regional, Eurasian-fixed reference frame and the decomposition of the LOS rates into east and vertical rates, particularly for long-wavelength signals. The GNSS data quality is somewhat limited, as the database contains only horizontal rates, derived from repeated, annual surveys in difficult terrain and confined by topography. The temporal resolution and accuracy of InSAR time-series (in line-of-sight) nearly equals daily GNSS solutions today and are able to reproduce ephemeral and seasonal processes. We discussed the most conspicuous tectonic and anthropogenic features, and linked them to the seismicity, and the geologic structures formed over the last ˜12 Ma.

The displacement-rate maps highlight the 3-D geometry of large parts of the northwestern orogenic margin of the India-Asia collision zone, with crustal material flowing laterally (westward) out of the N–S collision zone. The west-directed lateral extrusion rates increase from east to west from the eastern to the western Pamir and decrease from ˜20 to 5 mm/yr westward across the Tajik fold-thrust belt, dissipating over the salt-rooted structures. On the first-order, the modern shortening rates across the Tajik fold-thrust belt (20–5 mm/yr) correspond to the 12–8 mm/yr long-term shortening rates (148–93 km shortening over 12 Myr) in the north-central and southern Tajik fold-thrust belt, determined from line-length restoration and thermochronology. Characteristically, the modern westward rates are not affected by the vergence of the Tajik fold-thrust belt structures, in particular the Yavan synclinorium—the zone of vergence change; therefore, the entire Tajik fold-thrust belt is detached from its original substratum. The modern kinematics thus shows that the Tajik fold-thrust belt is a depression-wide, thin-skinned belt developed above an evaporitic decollement, whose evolution is governed by the westward growth of the Pamir orocline. A short-wavelength saw-blade pattern—superimposed on the regional horizontal displacement profiles—is interpreted as related to mass movements on steeply-dipping slopes of structurally controlled hogback ridges.

Abrupt ˜6 mm/yr changes in the horizontal rates occur across the kinematically-linked dextral Ilyak strike-slip fault bounding the Tajik fold-thrust belt to the north and the Babatag thrust, the major thrust of the fold-thrust belt, located far west in the belt. The dextral slip or creep rates on the Ilyak fault are of 5–10 mm/yr, decreasing towards west; the locking depth of the fault is [?]1 km.

The vertical and horizontal rates of the southeastern Tajik fold-thrust belt are laterally diverse with a distinct, patchy displacement signal, in particular in the region with salt tectonics, where upright detachment anticlines and bivergent thrust sheets pointing at an unconfined detachment. The highest displacement rates occur at the Hoja Mumin salt fountain, where we observed local uplift of ˜50 mm/yr at its top, surrounded by up to ˜120 mm/yr of subsidence and lateral outflow of ˜350 mm/yr to the west and ˜170 mm/yr to the east.

The vertical rate map outlines stripes with >15 mm/yr subsidence as the most outstanding feature of the Tajik depression; the strongest subsidence signal follows the major river valleys of the Tajik depression, which host intense agriculture. The subsidence is likely caused by a combination of a bias related to soil-moisture changes (slow dehumidification) and water extraction for the extensive irrigation. In addition, we observed strong uplift of 10–17 mm/yr in the western Pamir, and easternmost Tajik FTB where its eastern erosional edge is cut by the broad Darvaz fault zone. Both the high horizontal rates and the Pamir-ward increase of the vertical uplift rates support the existence of a crustal-scale antiform above a ramp caused by ongoing indentation of the leading edge of the Pamir below this marginal part of the Tajik depression, resulting in a passive roof uplift.

Acknowledgments

Qi Ou advised us on how to tie multiple InSAR rate maps to GNSS data. Some figures were created using GMT (Wessel et al., 2013) and colormaps of Crameri (2020). LiCS data (Looking into the

Continents from Space,*https://comet.nerc.ac.uk/comet-lics-portal/*) contains modified Copernicus Sentinel data analyzed by COMET, the Centre for the Observation and Modelling of Earthquakes, Volcanoes and Tectonics, using JASMIN, the UK's collaborative data analysis environment (*http://jasmin.ac.uk*). Atmospheric phase delay maps were provided by the Generic Atmospheric Correction Online Service for InSAR (*https://www.gacos.net*). The code for the LiCSBAS time-series analysis is available at*https://github.com/yumorishita/LiCSBAS*. GNSS rate tables are published as mentioned in the main text. The individual and the final, decomposed rate maps and uncertainties are provided in the Supporting Material. Funded by the Helmholtz Center, German Research Center for Geosciences, Potsdam, the German Research Council (DFG) grant RA 442/41, and the German Ministry of Science and Education within the CaTeNA project (support 3G0878A).

References

Abdulhameed, S., Ratschbacher, L., Jonckheere, R., Gagała, Ł., Enkelmann, E., Käßner, A., et al. (2020). Tajik Basin and Southwestern Tian Shan, Northwestern India-Asia Collision Zone: 2. Timing of Basin Inversion, Tian Shan Mountain Building, and Relation to Pamir-Plateau Advance and Deep India-Asia Indentation. *Tectonics* , *39* (5), e2019TC005873*https://doi.org/10.1029/2019TC005873*

Albertson, J. D. & Kiely, G. (2001). On the structure of soil moisture time series in the context of land surface models, *Journal of Hydrology* , *243* , 1–2, 101–119.*https://doi.org/10.1016/S0022-1694(00)00405-4*

Altamimi, Z., Métivier, L., Rebischung, P., Rouby, H., & Collilieux, X. (2017). ITRF2014 plate motion model. *Geophysical Journal International* , *209* (3), 1906–1912.*https://doi.org/10.1093/gji/ggx136*

Ansari, H., De Zan, F., & Parizzi, A. (2021). Study of Systematic Bias in Measuring Surface Deformation with SAR Interferometry. *IEEE Transactions on Geoscience and Remote Sensing* , *59* (2), 1285–1301.*https://doi.org/10.1109/TGRS.2020.3003421*

Bekker, Y.A. (1996). Tectonics of the Afghan–Tadjik Depression (russ.),*Geotektonika* , *30* (1), 76–82.

Bie, L., Hicks, S., Garth, T., Gonzalez, P., & Rietbrock, A. (2018). 'Two go together': Near-simultaneous moment release of two asperities during the 2016 Mw 6.6 Muji, China earthquake, *Earth and Planetary Science Letters* , *491* , 34–42.*https://doi.org/10.1016/j.epsl.2018.03.033*

Bloch, W., Metzger, S., Yuan, X., Xu, Q., Zhao, J., Schurr, B. (2019). Strain evolution and stress transfer during a 2-years earthquake sequence in the Pamirs, *American Geophysical Union* , Fall Meeting 2019, #G41B-0732.

Bourgeois, O., Cobbold, P. R., Rouby, D., Thomas, J.-C. J., & Shein, V. (1997). Least squares restoration of Tertiary thrust sheets in map view, Tajik depression, central Asia, *Journal of Geophysical Research* ,*102* (B12), 27553–27573.*https://doi.org/10.1029/97JB02477*

Burtman, V. S., & Molnar, P. (1993). Geological and Geophysical Evidence for Deep Subduction of Continental Crust Beneath the Pamir.*Geological Society of America Special Paper* , *281* , 1–76.*https://doi.org/10.1130/SPE281*

Cavalié, O., Doin, M.-P. P., Lasserre, C., & Briole, P. (2007). Ground motion measurement in the Lake Mead area, Nevada, by differential synthetic aperture radar interferometry time series analysis: Probing the lithosphere rheological structure, *Journal of Geophysical Research: Solid Earth* , *112* (B3), 1–18.*https://doi.org/10.1029/2006JB004344*

Chapman, J.B., Carrapa, B., Ballato, P., DeCelles, P.G., Worthington, J., Oimahmadov, I., Gadoev, M., Ketcham, R. (2017). Intracontinental subduction beneath the Pamir Mountains: Constraints from thermokinematic modeling of shortening in the Tajik fold-and-thrust belt, *GSA Bulletin* , *129* (11–12), 1450–1471.*https://doi.org/10.1130/B31730.1*

Chen, C. W., & Zebker, H. A. (2002). Phase unwrapping for large SAR interferograms: Statistical segmentation and generalized network models,*IEEE Transactions on Geoscience and Remote Sensing* , *40* (8),

1709–1719.*https://doi.org/10.1109/TGRS.2002.802453*

Crameri, F. (2020). Scientific color maps (Version 6.0.4).*https://doi.org/10.5281/zenodo.4153113*

De Zan, F., Parizzi, A., Prats-Iraola, P., & López-Dekker, P. (2014). A SAR interferometric model for soil moisture, *IEEE Transactions on Geoscience and Remote Sensing* , *52* (1), 418–425.*https://doi.org/10.1109/TGRS.2013.2241069*

De Zan, F., Zonno, M., & López-Dekker, P. (2015). Phase Inconsistencies and Multiple Scattering in SAR Interferometry, *IEEE Transactions on Geoscience and Remote Sensing* , *53* (12), 6608–6616.*https://doi.org/10.1109/TGRS.2015.2444431*

Doebrich, J. L., & Wahl R. R. (Compilators) (2006). Geological and mineral resource map of Afghanistan; Version 2. *U.S. Geol. Surv. Open File Rep.* , 2006–1038.

Doin, M.-P., Lodge, F., Guillaso, S., Jolivet, R., Lasserre, C., Ducret, G., et al. (2011). Presentation of the small baseline NSBAS processing chain on a case example: the Etna deformation monitoring from 2003 to 2010 using Envisat data, *Proceedings of the ESA Fringe 2011 Workshop* , Frascati, Italy, 19–23.

Dooley, T. P., Jackson, M. P. A., & Hudec, M. R. (2015). Breakout of squeezed stocks: Dispersal of roof fragments, source of extrusive salt and interaction with regional thrust faults, *Basin Research* ,*27* (1), 3–25.*https://doi.org/10.1111/bre.12056*

Efron, B., & Tibshirani, R. (1986). Bootstrap Methods for Standard Errors, Confidence Intervals, and Other Measures of Statistical Accuracy, *Statistical Science* , *1* , 54–75.*https://doi.org/10.1214/ss/1177013815*

Ekström, G., Nettles, M., & Dziewonski, A. M. (2012). The global CMT project 2004-2010: Centroid-moment tensors for 13,017 earthquakes,*Physics of the Earth and Planetary Interiors* , *200–201* , 1–9.*https://doi.org/10.1016/j.pepi.2012.04.002*

Elliott, A., Elliott, J., Hollingsworth, J., Kulikova, G., Parsons, B., & Walker, R. (2020). Satellite imaging of the 2015 M 7.2 earthquake in the Central Pamir, Tajikistan, elucidates a sequence of shallow strike-slip ruptures of the Sarez-Karakul fault, *Geophysical Journal International, 221* (3), 1696–1718. https://doi.org/10.1093/gji/ggaa090

Evans, S. G., Roberts, N. J., Ischuk, A., Delaney, K. B., Morozova, G. S., & Tutubalina, O. (2009). Landslides triggered by the 1949 Khait earthquake, Tajikistan, and associated loss of life, *Engineering Geology* , *109* (3–4), 195–212.*https://doi.org/10.1016/j.enggeo.2009.08.007*

Farr, T. G., Rosen, P. A., Caro, E., Crippen, R., Duren, R., Hensley, S., et al. (2007). The Shuttle Radar Topography Mission, *Review of Geophysics* , *45* (RG2004), 248.*https://doi.org/10.1029/2005RG000183*

Feng, W., Tian, Y., Zhang, Y., Samsonov, S., Almeida, R., & Liu, P. (2017). A Slip Gap of the 2016 Mw6.6 Muji, Xinjiang, China, Earthquake Inferred from Sentinel-1 TOPS Interferometry. *Seismological Research Letters* , *88* (4), 1054–1064.*https://doi.org/10.1785/0220170019*

Funning, G. J., Garcia, A. (2019). A systematic study of earthquake detectability using Sentinel-1 Interferometric Wide-Swath data,*Geophysical Journal International* , *216* (1), 332–349, Figure S23 in the supporting information.*https://doi.org/10.1093/gji/ggy426*

Gabriel, A. K., Goldstein, R. M., and Zebker, H. A. (1989). Mapping small elevation changes over large areas: Differential radar interferometry, *Journal Geophysical Research* , *94* (B7), 9183– 9191,*https://doi.org/10.1029/JB094iB07p09183*

Gareth, J. F., Garcia, A. (2019). A systematic study of earthquake detectability using Sentinel-1 Interferometric Wide-Swath data,*Geophysical Journal International* , *216* (1), 332–349.*https://doi.org/10.1093/gji/ggy426*

Gagała, Ł., Ratschbacher, L., Ringenbach, J. C., Kufner, S.-K., Schurr, B., Dedow, R., et al. (2020). Tajik Basin and Southwestern Tian Shan, Northwestern India-Asia Collision Zone: 1. Structure, Kinematics, and Salt Tectonics in the Tajik Fold-and-Thrust Belt of the Western Foreland of the Pamir, *Tectonics* , *39* (5), e2019TC005871.*https://doi.org/10.1029/2019TC005871*

Goldstein, R. M., & Werner, C. L. (1998). Radar interferogram filtering for geophysical applications, *Geophysical Research Letters* ,*25* (21), 4035–4038.*https://doi.org/10.1029/1998GL900033*

He, P., Hetland, E.A., Niemi, N.A., Wang, Q., Wen, Y. and Ding, K. (2018). The 2016 Mw6.5 Nura earthquake in the Trans Alai range, northern Pamir: possible rupture on a back-thrust fault constrained by Sentinel-1A radar interferometry, *Tectonophysics* , *749* , 62–71.*https://doi.org/10.1016/j.tecto.2018.10.025*

Hooper, A., Segall, P., & Zebker, H. (2007). Persistent scatterer interferometric synthetic aperture radar for crustal deformation analysis, with application to Volcán Alcedo, Galápagos, *Journal of Geophysical Research: Solid Earth* , *112* (7), 1–21.*https://doi.org/10.1029/2006JB004763*

Ischuk, A., Bendick, R., Rybin, A., Molnar, P., Khan, S. F., Kuzikov, S., et al. (2013). Kinematics of the Pamir and Hindu Kush regions from GPS geodesy, *Journal of Geophysical Research: Solid Earth* ,*118* (5), 2408–2416.*https://doi.org/10.1002/jgrb.50185*

Jepson, G., Glorie, S., Konopelko, D., Gillespie, J., Danišık, M., Evans, N. J., et al. (2018). Thermochronological insights into the structural contact between the Tian Shan and Pamirs, Tajikistan, *Terra Nova* , *30* , 95–104.*https://doi.org/10.1111/ter.12313*

Käßner, A., Ratschbacher, L., Jonckheere, R., Enkelmann, E., Khan, J., Sonntag, B.-L., et al. (2016). Cenozoic intracontinental deformation and exhumation at the northwestern tip of the India-Asia collision—southwestern Tian Shan, Tajikistan, and Kyrgyzstan, *Tectonics* , *35* (9), 2171–2194.*https://doi.org/10.1002/2015TC003897*

Kondorskaya, N., & Shebalin, N. (chief editors). (1982). New Catalog of Strong Earthquakes in the U.S.S.R. from Ancient Times Through 1977, Report SE31, *World Data Center A for Solid Earth Geophysics* , 609.

Kufner, S.-K., Schurr, B., Sippl, C., Yuan, X., Ratschbacher, L., son of Mohammad Akbar, A., et al. (2016). Deep India meets deep Asia: Lithospheric indentation, delamination and break-off under Pamir and Hindu Kush (Central Asia), *Earth and Planetary Science Letters* ,*435* , 171–184.*https://doi.org/10.1016/j.epsl.2015.11.046*

Kufner, S.-K., Schurr, B., Haberland, C., Zhang, Y., Saul, J., Ischuk, A., & Oimahmadov, I. (2017). Zooming into the Hindu Kush slab break-off: a rare glimpse on the terminal stage of subduction, *Earth and Planetary Science Letters* , *461* , 127–140.*https://doi.org/10.1016/j.epsl.2016.12.043*

Kufner, S.-K., Schurr, B., Ratschbacher, L., Murodkulov, S., Abdulhameed, S., Ischuk, A., et al. (2018). Seismotectonics of the Tajik Basin and Surrounding Mountain Ranges, *Tectonics* , *37* (8), 2404–2424.*https://doi.org/10.1029/2017TC004812*

Kufner, S.-K., Kakar, N., Bezada, M., Bloch, W., Metzger, S., Yuan, X., et al. (2021). The Hindu Kush slab break-off as revealed by deep structure and crustal deformation, *Nature Communication* , 12, 1685.*https://doi.org/10.1038/s41467-021-21760-w*

Kulikova, G. (2016). Source parameters of the major historical earthquakes in the Tien-Shan region from the late 19th to the early 20th century, *PhD Thesis* , Potsdam University

Lazeck, M., Spaans, K., González, P. J., Maghsoudi, Y., Morishita, Y., Albino, F., et al. (2020). LiCSAR: An automatic InSAR tool for measuring and monitoring tectonic and volcanic activity, *Remote Sensing* ,*12* (15).*https://doi.org/10.3390/RS12152430*

López-Quiroz, P., Doin, M.P., Tupin, F., Briole, P., Nicolas, J.M., (2009). Time series analysis of

Mexico City subsidence constrained by radar interferometry, Journal of Applied Geophysics, 69, 1–15.*https://doi.org/10.1016/j.jappgeo.2009.02.006*

Leith, W., & Simpson, D. W. (1986). Earthquakes related to active salt doming near Kulyab, Tadjikistan, USSR, *Geophysical Research Letters* , *13* (10), 1019–1022.*https://doi.org/10.1029/GL013i010p01019*

McNab, F., Sloan, R. A., & Walker, R. T. (2019). Simultaneous orthogonal shortening in the Afghan-Tajik Depression, *Geology* ,*47* (9), 862–866.*https://doi.org/10.1130/G46090.1*

Mechie, J., Yuan, X., Schurr, B., Schneider, F., Sippl, C., Ratschbacher, L., et al. (2012). Crustal and uppermost mantle velocity structure along a profile across the Pamir and southern Tien Shan as derived from project TIPAGE wide-angle seismic data, *Geophysical Journal International* , *188* (2), 385–407.*https://doi.org/10.1111/j.1365-246X.2011.05278.x*

Metzger, S., Schurr, B., Ratschbacher, L., Sudhaus, H., Kufner, S.-K., Schöne, T., et al. (2017). The 2015 Mw7.2 Sarez strike-slip earthquake in the Pamir interior: Response to the underthrusting of India's western promontory, *Tectonics* , *36* (11), 2407–2421.*https://doi.org/10.1002/2017TC004581R*

Metzger, S., Ischuk, A., Akhmedov, A., Ilyasova, Z., Moreno, M., Murodkulov, S., & Deng, Z. (2019). Survey mode GPS data in the West Pamir, Tajikistan, Central Asia, 2013–2016, *GFZ Data Services .https://doi.org/10.5880/GFZ.4.1.2019.007*

Metzger, S., Ischuk, A., Deng, Z., Ratschbacher, L., Perry, M., Kufner, S.-K., et al. (2020). Dense GNSS profiles across the northwestern tip of the India-Asia collision zone: Triggered slip and westward flow of the Peter the First Range, Pamir, into the Tajik depression,*Tectonics* , *39* (2), e2019TC005797.*https://doi.org/10.1029/2019TC005797*

Metzger, S., Kakar, N., Zubovich, A., Borisov, M., Saif, S., Panjsheri, A.H., Rahmani, J.R., Zaryab, M.Y., Rezai, M.T., Deng, Z.,Bendick, R., Kufner, S.-K., Okoev, J. (2021). Survey mode GNSS data, acquired 2014-2019 in the Afghan Hindu Kush and across northern Pamir margin, Central Asia, *GFZ Data Services* ,*https://doi.org/10.5880/GFZ.4.1.2021.003*

Mohadjer, S., Bendick, R., Ischuk, A., Kuzikov, S., Kostuk, A., Saydullaev, U., et al. (2010). Partitioning of India-Eurasia convergence in the Pamir-Hindu Kush from GPS measurements, *Geophysical Research Letters* , *37* (4).*https://doi.org/10.1029/2009GL041737*

Morishita, Y., Lazecky, M., Wright, T. J., Weiss, J. R., Hooper, A., Elliott, J. R., & Hooper, A. (2020). LiCSBAS: An Open-Source InSAR Time Series Analysis Package Integrated with the LiCSAR Automated Sentinel-1 InSAR Processor, *Remote Sensing* , *12* (3), 5–8.*https://doi.org/10.3390/rs12030424*

Neelmeijer, J., Schöne, T., Dill, R., Klemann, V., & Motagh, M. (2018). Ground Deformations around the Toktogul Reservoir, Kyrgyzstan, from Envisat ASAR and Sentinel-1 Data—A Case Study about the Impact of Atmospheric Corrections on InSAR Time Series, *Remote Sensing* ,*10* (3), 462.*https://doi.org/10.3390/rs10030462*

Nikolaev, V. G. (2002). Afghan-Tajik depression: Architecture of sedimentary cover and evolution, *Russian Journal of Earth Science* , *4* (6), 399–421.

Ou, Q. (2020). Crustal Deformation and Seismic Hazard of the NE Tibetan Plateau, *PhD Thesis* , University of Oxford.

Perry, M., Kakar, N., Ischuk, A., Metzger, S., Bendick, R., Molnar, P., & Mohadjer, S. (2018). Little Geodetic Evidence for Localized Indian Subduction in the Pamir-Hindu Kush of Central Asia, *Geophysical Research Letters* , *46* (1), 109–118.*https://doi.org/10.1029/2018GL080065*

Pozzi, J. P., & Feinberg, H. (1991). Paleomagnetism in the Tajikistan: Continental shortening of European margin in the Pamirs during Indian Eurasian collision, *Earth and Planetary Science Letters* ,*103* (1–4), 365–378.*https://doi.org/10.1016/0012-821X(91)90173-F*

Robinson, A.C., Yin, A., Manning, C.E., Harrison, T.M., Zhang, S.-H., Wang, X.-F. (2004). Tectonic evolution of the northeastern Pamir: Constraints from the northern portion of the Cenozoic Kongur Shan extensional system, western China, *GSA Bulletin* ,*116* (7–8), 953–973.*https://doi.org/10.1130/B25375.1*

Robinson, A.C., Yin, A., Manning, C.E., Harrison, T. M., Zhang, S.-H., Wang, X.-F. (2007) Cenozoic evolution of the eastern Pamir: Implications for strain-accommodation mechanisms at the western end of the Himalayan-Tibetan orogen, *GSA Bulletin* , *119* (7–8), 882–896.*https://doi.org/10.1130/B25981.1*

Rouyet, L., Lauknes, T. R., Christiansen, H. H., Strand, S. M., & Larsen, Y. (2019). Seasonal dynamics of a permafrost landscape, Adventdalen, Svalbard, investigated by InSAR, *Remote Sensing of Environment* , *231* , 111236.*https://doi.org/10.1016/j.rse.2019.111236*

Rutte, D., Ratschbacher, L., Schneider, S., Stübner, K., Stearns, M. A., Gulzar, M. A., et al. (2017). Building the Pamir-Tibetan Plateau – Crustal stacking, extensional collapse, and lateral extrusion in the Central Pamir: 1. Geometry and kinematics, *Tectonics* ,*36* (3), 342–384.*https://doi.org/10.1002/2016TC004293*

Sangha, S., Peltzer, G., Zhang, A., Meng, L., Lian, C., Lundgren, P., et al. (2017). Fault geometry of 2015, Mw7.2 Murghab, Tajikistan earthquake controls rupture propagation: Insights from InSAR and seismological data, *Earth and Planetary Science Letters* , *462* , 132–141.*https://doi.org/10.1016/j.epsl.2017.01.018*

Savage, J. C., & Burford, R. O. (1973). Geodetic Determination of Relative Plate Motion in Central California, *Journal of Geophysical Research* , *78* (5), 832–845.*https://doi.org/10.1029/JB078i005p00832*

Schneider, F. M., Yuan, X., Schurr, B., Mechie, J., Sippl, C., Kufner, S.-K., et al. (2019). The Crust in the Pamir: Insights From Receiver Functions Journal of Geophysical Research: Solid Earth, *Journal of Geophysical Research: Solid Earth* , *124* , 9313– 9331.*https://doi.org/10.1029/2019JB017765*

Schurr, B., Ratschbacher, L., Sippl, C., Gloaguen, R., Yuan, X., & Mechie, J. (2014). Seismotectonics of the Pamir, *Tectonics* ,*33* (80), 1501–1518.*https://doi.org/10.1002/2014TC003576*

Schwab, M., Ratschbacher, L., Siebel, W., McWilliams, M., Minaev, V., Lutkov, V., et al. (2004), Assembly of the Pamirs: Age and origin of magmatic belts from the southern Tien Shan to the southern Pamirs and their relation to Tibet, *Tectonics* , *23* , TC4002.*https://doi.org/10.1029/2003TC001583*

Sippl, C., Schurr, B., Yuan, X., Mechie, J., Schneider, F. M., Gadoev, M., et al. (2013). Geometry of the Pamir-Hindu Kush intermediate-depth earthquake zone from local seismic data, *Journal of Geophysical Research: Solid Earth* , *118* (4), 1438–1457.*https://doi.org/10.1002/jgrb.50128*

Sippl, C., Ratschbacher, L., Schurr, B., Krumbiegel, C., Rui, H., Pingren, L., & Abdybachaev, U. (2014). The 2008 Nura earthquake sequence at the Pamir-Tian Shan collision zone, southern Kyrgyzstan, *Tectonics* , *33* (12), 2382–2399.*https://doi.org/10.1002/2014TC003705*

Sperner, B. & Ratschbacher, L. (1994). A Turbo Pascal program package for graphical presentation and stress analysis of calcite deformation,*Zeitschriften der Deutschen Geologischen Gesellschaft* ,*145* , 414–423.

Storchak, D. A., Di Giacomo, D., Bondár, I., Engdahl, E. R., Harris, J., Lee, W. H. K., et al. (2013). Public release of the ISC-GEM global instrumental earthquake catalogue (1900–2009), *Seismological Research Letters* , *84* , 810–815.*https://doi.org/10.1785/0220130034*

Stübner, K., Ratschbacher, L., Rutte, D., Stanek, K., Minaev, V., Wiesinger, R., et al. (2013). The giant Shakhdara migmatitic gneiss dome, Pamir, India-Asia collision zone, 1: Geometry and kinematics, *Tectonics* , *32* , 948–979.*https://doi.org/10.1002/tect.20057*

Stübner, K., Grin, E., Hidy, A.J., Schaller, M., Gold, R.D., Ratschbacher, L., Ehlers, T. (2017). Middle and Late Pleistocene glaciations in the southwestern Pamir and their effects on topography,*Earth and Planetary Science Letters* , *466* , 181–194.*https://doi.org/10.1016/j.epsl.2017.03.012*

Teshebaeva, K., Sudhaus, H., Echtler, H., Schurr, B., & Roessner, S. (2014). Strain partitioning at the eastern Pamir-Alai revealed through SAR data analysis of the 2008 Nura earthquake, *Geophysical Journal*

International , *198* (2), 760–774.*https://doi.org/10.1093/gji/ggu158*

Thomas, J.-C., Chauvin, A., Gapais, D., Bazhenov, M. L., Perroud, H., Cobbold, P. R., and Burtman, V. S. (1994). Paleomagnetic evidence for Cenozoic block rotations in the Tadjik depression (Central Asia),*Journal of Geophysical Research* , *99* (B8), 15141-15160.*https://doi.org/10.1029/94JB00901*

Vajedian, S., Motagh, M., Wetzel, H.-U., Teshebaeva, K. (2017). Coupling of Sentinel-1, Sentinel-2 and ALOS-2 to assess coseismic deformation and earthquake-induced landslides following the 26 June, 2016 earthquake in Kyrgyzstan, *Geophysical Research Abstracts* , *19* , EGU2017-18464-1.

Wang, S., Xu, C., Wen, Y., Yin, Z., Jiang, G., Fang, L. (2017). Slip Model for the 25 November 2016 Mw6.6 Aketao Earthquake, Western China, Revealed by Sentinel-1 and ALOS-2 Observations, *Remote Sensing* ,*9* , 325,*https://doi.org/10.3390/rs9040325*

Wegmuller, U., & Werner, C. (1997). Gamma SAR processor and interferometry software. *ERS Symposium on Space at the Service of Our Environment* , Florence, Italy.

Wegmuller, U., Werner, C., Strozzi, T., Wiesmann, A., Frey, O., & Santoro, M. (2016). Sentinel-1 Support in the GAMMA Software,*Procedia Computer Science* , *100* , 1305–1312.*https://doi.org/https://doi.org/10.1016/j.procs.2016.09.246*

Weiss, J. R., Walters, R. J., Morishita, Y., Wright, T. J., Lazecky, M., Wang, H., et al. (2020). High-Resolution Surface Velocities and Strain for Anatolia From Sentinel-1 InSAR and GNSS Data, *Geophysical Research Letters* , *47* (17).*https://doi.org/10.1029/2020GL087376*

Wessel, P., Smith, W. H. F., Scharroo, R., Luis, J. F., & Wobbe, F. (2013). Generic Mapping Tools: Improved version released, *EOS Transactions AGU* , *94* , 409–410.*https://doi.org/10.1002/2013EO450001*

Wilkinson, R., Daout, S., Parsons, B., & Walker, R. T. (2020). A time-series InSAR study of faulting and folding in the Tajik Basin,*American Geophysical Union* , Fall Meeting 2020, #G021-0007.

Wright, T. J., Parsons, B. E., & Lu, Z. (2004). Toward mapping surface deformation in three dimensions using InSAR, *Geophysical Research Letters* , *31* , L01607.*https://doi.org/https://doi.org/10.1029/2003GL018827*

Yu, C., Li, Z., Penna, N. T., & Crippa, P. (2018). Generic Atmospheric Correction Model for Interferometric Synthetic Aperture Radar Observations, *Journal of Geophysical Research: Solid Earth* ,*123* (10), 9202–9222.*https://doi.org/10.1029/2017JB015305*

Zhan, Z., & Kanamori, H. (2016). Recurring large deep earthquakes in Hindu Kush driven by a sinking slab, *Geophysical Research Letters* , *43* (14), 7433–7441.*https://doi.org/10.1002/2016GL069603*

Zubovich, A. V., Wang, X. Q., Scherba, Y. G., Schelochkov, G. G., Reilinger, R., Reigber, C., et al. (2010). GPS velocity field of the Tien Shan and surrounding regions, *Tectonics* , *29* (TC6014), 1–23.*https://doi.org/10.1029/2010TC002772*

Zubovich, A. V., Schone, T., Metzger, S., Mosienko, O., Mukhamediev, S., Sharshebaev, A., & Zech, C. (2016). Tectonic interaction between the Pamir and Tien Shan observed by GPS, *Tectonics* , *35* (2), 283–292.*https://doi.org/10.1002/2015TC004055*

Sabrina Metzger[1], Łukasz Gągała[2,3], Lothar Ratschbacher[2], Milan Lazecký[4], Yasser Maghsoudi[4] and Bernd Schurr[1]

[1]Lithosphere Dynamics, Helmholtz Center, Research Center for Geosciences, Potsdam, Germany.

[2]Geologie, Technische Universität Bergakademie Freiberg, Freiberg, Germany.

[3]Now at Hellenic Petroleum, Marousi, Greece.

[4]COMET, School of Earth and Environment, University of Leeds, United Kingdom.

Corresponding author: Sabrina Metzger (metzger@gfz-potsdam.de)

Key Points:

- The east- and up-rate maps exhibit tectonic and anthropogenic processes with mm-accuracy in high spatial resolution (400 m).
- The quality of our rate maps depends on interferometric data coherence and the availability of accurate positioning data.
- The major tectonic signal is E–W shortening in the Tajik fold-thrust belt due to the westward collapse of the Pamir-Plateau crust.

Abstract

Embedded between the Tian Shan, Pamir, and Hindu Kush, the Tajik depression is a remnant of the Mesozoic-Miocene Tajik-Tarim basin system. Since ~12 Ma, westward collapse of the north-advancing Pamir-Plateau crust inverted the Tajik basin into a thin-skinned fold-thrust belt with ~150 km of ~E–W shortening distributed between foreland- and hinterland-vergent structures. Geodetically-derived shortening rates decay westward from ~15 to 2 mm/yr. Seismicity outlines the ~east-striking dextral Ilyak fault, bounding the fold-thrust belt in the north, and distributed shortening in the central and eastern Tajik depression. We derived E–W and vertical deformation-rate maps from radar interferometric time-series, consisting of 900+ radar scenes acquired over 2.0–4.5 years, and available accurate positioning data. We confirm the westward collapse of the Pamir and the drastic shortening-rate decline across the Main Pamir Thrust at the Pamir front. In the Tajik depression, the maps unveil a combination of basin-scale tectonics, local halokinesis, and seasonal/weather-driven soil or near-surface effects. Although the Tajik-basin strata move westward with rates decreasing away from the Pamir, the most external Babatag backthrust currently absorbs the highest shortening (~6 mm/yr) as it has done in the past (20 km). The Ilyak fault accommodates ~5–8 mm/yr, eastward-increasing slip; rates decay sharply across the fault, suggesting a locking depth of 1 km—possibly creep. At least 10 mm/yr uplift and westward motion occur across the Tajik-depression–Pamir transition, including the sinistral Darvaz fault zone, likely outlining a crustal-scale ramp. The Hoja Mumin salt fountain is spreading laterally at >300 mm/yr.

Plain Language Summary

As a result of the collision of the Eurasian and Indian continent 30 million years ago, the Tethys ocean closed, and the Tian-Shan-Pamir-Tibet-Himalayan mountain ranges were created. Today the Pamir advances north, only being stopped by the Tian Shan, and thus is collapsing westward into the lower-lying Tajik depression. The (formerly) horizontal deposits of ancient marine sediments in the depression now form a series of folds and faults, running parallel to the Pamirs rim. We use ~5-years of regularly acquired satellite radar imagery and pointwise positioning data to monitor the surface-deformation rates of the whole region. The resulting rate maps visualize crustal-scale and near-surface—partly man-made—processes with an accuracy of a few millimeters and a spatial resolution of ~400 m. We show that the folds and faults are sliding on low-friction sediments like salt or gypsum, detached from the underlying basement. The sliding stops suddenly at the western end of the basin. In the basin, old salt deposits are squeezed to the surface, forming a salt fountain that spreads more than 30 cm/yr. In agricultural areas we see subsidence of more than 1 cm/yr, which might be (partially) due to unsustainable ground-water extraction.

1 Introduction

At the western end of the India-Asian collision zone, the Tian Shan, Pamir, and Hindu Kush frame the Tajik depression, hosting the Tajik basin (Figure 1a). Deformation rates derived from global positioning (GNSS) data along the northern and western margins of the Pamir facing the depression reach ~20 mm/yr (Metzger et al., 2020; Zubovich et al., 2010), being among the highest measured inside a continent. The accommodating crustal structures—thrusts and strike-slip faults—host abundant seismicity (e.g., Kufner et al., 2018; Schurr et al., 2014), including seven magnitude M7 earthquakes during the past 100 years. Structural geometries, GNSS velocities, and seismicity inside the Tajik depression suggest that a thin-skinned belt above an evaporitic décollement at 6–12 km depth—the Tajik fold-thrust belt (FTB)—is accommodating westward (lateral) extrusion of Pamir-Plateau crust (e.g., Bekker, 1996; Bourgeois et al., 1997; Gągała et al., 2020; Schurr et al., 2014; Stübner et al., 2013). Although the distribution and age of shortening is relatively well constrained geologically (e.g., Abdulhameed et al., 2020; Gągała et al., 2020), the sparse GNSS data prohibit the quantification of the contributions of the individual structures to the recent E–W shortening; in addition, the geodetically-derived rates might be influenced by salt tectonics (Ischuk et al., 2013; Metzger et al., 2020). To assess the distribution of active slip within the Tajik FTB and the surrounding mountain ranges, a sampling method with higher spatial resolution for the active deformation is needed.

Since the launch of the European Sentinel-1 radar satellite mission in 2014, Interferometric Synthetic Aperture Radar (InSAR) data have become easily accessible and tectonically active regions are monitored every 3–12 days worldwide. The data—usually provided in single tiles—cover ~240 × 200 km on ground (Figure 1b) and allow the detection of rate changes of ~1 mm/yr (e.g.,

Weiss et al., 2020). Herein, we present relative displacement-rate maps for the Tajik FTB and the adjoining Pamir and Hindu Kush with a spatial resolution of ~400 m. We derive 13 individual rate maps in two independent view angles, tied to available GNSS rates in a Eurasia-fixed reference frame (Figure 1c), and decomposed into horizontal (E–W) and vertical rates (Figures 2 and 3).

We highlight and discuss the most conspicuous anthropogenic and tectonic features, and link them to the seismicity and the geologic structures formed over the last ~12 Ma. In the Tajik and Ferghana depressions, the vertical rate map outlines stripes with >15 mm/yr subsidence, with the strongest signal following the major river valleys. This subsidence is likely caused by water extraction for irrigation. The vertical uplift rates are also high at the Tajik FTB's eastern edge and the adjacent western Pamir. Together with high horizontal rates, they likely outline passive roof uplift above a crustal-scale ramp, caused by the indentation of the leading edge of the Pamir. The horizontal rate map outlines the complex 3-D geometry of an orogenic margin, with crustal material flowing laterally (westward) out of the N–S collision zone. Lateral extrusion rates increase from east to west from the eastern to the western Pamir and decrease westward across the Tajik FTB, dissipating over the salt-rooted structures. An abrupt rate change occurs across the kinematically-linked dextral Ilyak strike-slip fault bounding the Tajik FTB to the north and the Babatag thrust, the major thrust of the western FTB. The horizontal displacement rates are not affected by the vergence of the fold-thrust structures; therefore, the entire Tajik FTB is detached from its original substratum. The recent kinematics imply that the Tajik FTB is a thin-skinned belt developed above a depression-wide evaporitic décollement, whose evolution is governed by the westward advance of the outward-growing Pamir orocline.

2 **Tectonic Setting**

The Tajik FTB and the bounding mountain belts of the Tian Shan, Pamir, and Hindu Kush formed due to the northward advance of western promontory of the India (e.g., Burtman & Molnar, 1993; Kufner et al., 2016; Schwab et al., 2004). The 65–75-km-thick Pamir-Plateau crust (Mechie et al., 2012; Schneider et al., 2019) moves northward and collides with the Tian Shan, and at the same time collapses and extrudes westward into the Tajik depression, inverting the Tajik basin and forming the Tajik FTB (Figure 1a; e.g., Kufner et al., 2018; Nikolaev, 2002; Schurr et al., 2014; Stübner et al., 2013). The Tajik FTB comprises a series of westward-convex, ~N-trending folds and thrusts (e.g., Bourgeois et al., 1997; Chapman et al., 2017; Gągała et al., 2020) that bend in the north into the dextral Ilyak fault (Leith & Simpson, 1986); a similar—less pronounced—bending occurs in the south but no bounding strike-slip fault—akin to the Ilyak fault—has developed (Figures 2 and 3). This is compatible with the <50°, paleomagnetically-determined, anti-clockwise vertical-axis rotations in the northern Tajik FTB (e.g., Pozzi & Feinberg, 1991; Thomas et al., 1994). The Tajik FTB, southwestern Tian Shan, and Hindu Kush reflect partitioning of deformation into ~N–S shortening accompanied by dextral slip in the Tian Shan

and along the Ilyak fault, ~E–W shortening in the Tajik FTB, and ~NW–SE shortening in the Afghan platform in the foothills of the Hindu Kush (Käßner et al., 2016; Kufner et al., 2018; 2021; McNab et al., 2019).

Total ~E–W shortening reaches ~148 km in the north-central Tajik FTB, with decaying values towards south (~93 km) and towards northeast into the narrow corridor between the Pamir and Tian Shan (>22 km; Gągała et al., 2020). The southeastern part of the Tajik FTB showcases salt tectonics, e.g., at the Hoja Mumin salt fountain with vertical extrusion rates of ~170 mm/yr (Leith & Simpson, 1986). The southwestern Tian Shan—the Uzbek and Tajik Gissar—constitute the thick-skinned foreland buttresses to the Tajik FTB (Figure 1a; Gągała et al., 2020). To the east, along the front of the Pamir, the Tian Shan is separated from the Pamir Plateau by the Pamir Thrust System with its leading fault, the Pamir Frontal Thrust; its western part—in the Peter I. Range—is the dextral-transpressive Vakhsh thrust that transitions westward into the Ilyak fault (Figure 1a). In the Pamir, the ~NNW-striking, sinistral-transtensive Sarez-Karakul fault system separates the western and eastern Pamir (Figure 1a). The latter is dominated by en-bloc northward advance, whereas the former has distinct westward flow component (Ischuk et al., 2013; Kufner et al., 2018; Metzger et al., 2020).

Abdulhameed et al. (2020) estimated—based on low-temperature thermochronologic data that incorporate dates from Chapman et al. (2017) and Jepson et al. (2018)—that major shortening started at ~12 Ma, spread immediately across the entire FTB, and declined at ~9 Ma in the western FTB; reactivation concentrated in the internal (eastern) FTB with the thickest evaporates. The youngest ages (~7–2 Ma) occur along the Vakhsh thrust, i.e., the active erosional front of the northeastern Tajik FTB belt, where it narrows between the converging Tian Shan and Pamir, and along eastern edge of the FTB—at the western flank of the Pamir Plateau, dominated by the sinistral-transpressive Darvaz fault zone. The onset at ~12 Ma yields 12–8 mm/yr average long-term shortening rates in the north-central and southern Tajik FTB (see total shortening values above).

GNSS survey profiles across the Pamir's northern and western margins provide insights into the large-scale deformation and fault kinematics (Figure 1a). The highest rates were observed across the Pamir Frontal Thrust (13–19 mm/yr shortening, ~7 mm/yr dextral shear, Zubovich et al., 2010). Across the Vakhsh thrust, shortening is 15 +4/-2 mm/yr, while dextral shear increases to 16 ± 3 mm/yr; the Ilyak fault accommodates 8–15 mm/yr of dextral shear and ~5 mm/yr of shortening (Metzger et al., 2020). Kinematic modeling indicates a rather shallow fault-locking depth at the Vakhsh fault of <5 km. The rates across the Darvaz fault zone decay from north to south, i.e., from ~15 to 7–9 mm/yr sinistral shear and from ~10 to 4–0 mm/yr extension. The Sarez-Karakul fault system accommodates 5 ± 2 mm/yr sinistral slip (Metzger et al., 2017). The sparse GNSS data in the Tajik depression show that it is shortening ~ENE–WSW (Ischuk et al., 2013; Metzger et al., 2020; Mohadjer et al., 2010). The

interior of the Tian Shan exhibits minor dextral shear and shortening (Figure 1a). The recent kinematics of the Uzbek Gissar and the Afghan platform are largely unresolved. In the Hindu Kush, two relatively short GNSS profiles across the NE- to NNE-striking, poorly-mapped faults indicate sinistral-transpressive motion of 2.5 ± 1.8 mm/yr in the central Hindu Kush and 7.3 ± 1.0 mm/yr in the northeastern Hindu Kush (Figure 1a; Kufner et al., 2021; Perry et al., 2018).

Abundant crustal seismicity highlights the most active faults, i.e., the Pamir Frontal Thrust, the Vakhsh thrust, the Darvaz fault zone, and the Sarez-Karakul fault system (Figure 1a; Kufner et al., 2018; Schurr et al., 2014; Sippl, et al., 2013). The earthquake focal mechanisms fit the observed fault kinematics (Kufner et al., 2018; Schurr et al., 2014). Seismicity is abundant beneath the Peter I. Range that is squeezed between converging Vakhsh and Darvaz faults, and north of the eastern Pamir, where the 2008 M_w6.6 Nura earthquake (Sippl et al., 2014; Teshebaeva et al., 2014; He et al., 2018), the 2016 M_w6.4 Sary-Tash earthquake (Bloch et al., 2019; Funning & Garcia, 2019; Vajedian et al., 2017), and the 2016 M_w6.6 Aketao/Muji earthquake (e.g., Wang et al., 2017; Feng et al., 2017) ruptured the Pamir Thrust System, respectively the Muji fault (Figure 1a). Sparse seismicity occurs in the western Tajik depression; in its eastern part, it is intense but diffuse with focal mechanisms indicating overall E–W shortening (Figure 3; Kufner et al., 2018). Most events occur at 5–25 km depth, i.e., in general below the evaporite décollement, with the overlying sedimentary stack deforming mostly aseismic (Gągała et al., 2020). The Ilyak fault appears to be mostly aseismic, apart from a cluster of seismicity southeast of Dushanbe (Figure 3; section 4.3.2). In the Hindu Kush, crustal seismicity is also sparse, suggesting that crustal faults are locked, with diffuse strain accumulation (Kufner et al., 2021).

In the context of our data analysis, a few large earthquakes stand out (Figure 1a): the 2015 M_w7.2 Sarez earthquake ruptured the central Pamir along the Sarez-Karakul fault system (Elliot et al., 2020; Metzger et al., 2017; Sangha et al., 2017); this event was in sequence with the two 2016 M6 earthquakes at the northern rim of the Pamir mentioned above (Bloch et al., 2019). The 1949 M_w7.6 Khait earthquake affected the Tian Shan region north of Peter I. Range, causing a series of landslides (Evans et al., 2009; Kulikova, 2016). In 1907, the poorly located $M_s7.6 \pm 0.3$ Kharatag earthquake occurred somewhere at the northern rim of the Tajik depression (Kondorskaya & Shebalin, 1982) or farther east in the Peter I. Range (Kulikova, 2016; Storchak et al., 2013). The region also hosts frequent intermediate-depth earthquakes at 80–300 km depth, which are related to the ongoing indentation of Indian cratonic lithosphere beneath the Pamir and the subduction and break-off of marginal Indian lithosphere below the central Hindu Kush (Figure 1a; Sippl et al. 2013; Kufner et al., 2016, 2017, 2021). In 2015, during the InSAR data acquisition, the Hindu Kush hosted a M_w7.5 earthquake at ~200 km depth, related to slab break-off (Kufner et al., 2017).

3 Data Processing

3.1 InSAR Time-series Analysis

We used data from the Sentinel-1 satellites operating in C-Band with a wavelength of ~5.55 cm, published on the LiCS data portal as automatically preprocessed, differential interferograms (Lazecký et al., 2020): each radar scene was automatically combined with three preceding and three subsequent scenes in time, resulting in six interferometric products with temporal baselines of a couple of weeks each (assuming no time gaps). The interferograms were created with the GAMMA SAR software (Wegmüller et al., 2016; Wegmüller & Werner, 1997) and multi-looked (downsampled) to ~100 m spatial resolution. They were filtered using an adaptive phase filter (Goldstein & Werner, 1998), assuming that short-baseline interferograms contain no sudden phase changes—e.g. due to fault creep—that are naturally smeared by strong filtering. Pixels with low coherence values were masked and the data were unwrapped automatically using SNAPHU v2 (Chen & Zebker, 2002). The unwrapped interferograms were resampled and geocoded using the 1-arc-second, void-filled digital elevation model of the Shuttle Radar Topography Mission (Farr et al., 2007). Each radar scene spatially overlaps along-track with other data frames of the same acquisition time and along-range with time-independent acquisitions (Figure 1b).

Interferometric time-series analysis allows to single out the small, secular tectonic and/or anthropogenic signals from of the interferometric noise. This is done frame-wise (Figure 1b) by spanning a network of all interferometric scenes of one radar frame (Figure S1 of the supporting information). We used a modified small-baseline approach (NSBAS, López-Quiroz et al., 2009; Doin et al., 2011), as implemented in the python code LiCSBAS (Morishita et al., 2020) that directly integrates LiCS interferograms. Tropospheric noise was suppressed using synchronous tropospheric delay maps, which are based on extrapolated weather data of the European Centre for Medium-Range Weather Forecasts in a horizontal resolution of 0.125°, updated every six hours (Yu et al., 2018). We automatically excluded interferograms from further processing, if they contained sparse or noisy data or did not pass a phase-loop closure test indicating severe unwrapping errors. The most stable pixel over time was selected as a reference pixel (red stars in Figures S2a and S2b). The whole interferometric network was then inverted for incremental displacements between the acquisition dates, with the mean displacement velocity being derived from the cumulative displacements by least-squares (Morishita et al., 2020). Network gaps were overcome by adding a linear constraint with a scaling factor to the Green's functions (Doin et al., 2011). The standard deviation of the inverted rates was obtained by percentile bootstrapping (Efron & Tibshirani, 1986). The uncertainties are usually underestimated, particularly if the network is not fully connected (Morishita et al., 2020). The resulting rate maps are masked by several quality assessment criteria, such as interferometric coherence, amount of data, rate standard deviation, time period covered, number of network gaps, or unwrapping errors, or root-mean-square of rate residuals. Finally, the maps were high-pass filtered in

time and low-pass filtered in space using a Gaussian filter kernel (Hooper et al., 2007).

We processed six overlapping frames in ascending flight mode and seven frames in descending flight mode of three adjacent satellite tracks (Figure 1b). The assembled dataset covers 270,000 km^2 in both view angles, stretching north-south from the Ferghana depression to the Hindu Kush and west-east from the Tajik depression to the eastern Pamir (Figure 2). Before 2016, data acquisition occurred irregularly and only few interferograms of poor quality are available. In the Pamir, many frames show co- or post-seismic displacements related to the 2015 M_w7.2 Sarez earthquake (Metzger et al., 2017). In this region, we used only data acquired one year or more after the earthquake (Figure S1). Overall, each frame contains 255–500 interferograms of 82–175 radar images spanning 2–6 years (Table S1). To increase the processing speed, the interferograms were downsampled by 4x4 block averaging to a ground resolution of ~350 m in range and ~450 m in azimuth. After quality assessment, the remaining 50–110 scenes spanned a network of 120–350 interferograms (Table S1). The rates resulting from the time-series analysis were masked using standard threshold parameters, i.e., an average coherence of >0.05, a rate standard deviation of <100 mm/yr, <10 network gaps, and a spatio-temporal consistency of at least 5 mm. Some of these parameters were modified individually after a visual inspection (Table S2). After the multi-looking and atmospheric correction procedures, we repeated each processing step iteratively, removed poor interferograms, or corrected unwrapping errors manually. This improved the data quality, in particular in the rugged western Pamir, where the rates are most difficult to retrieve. The spatio-temporal filter was set to three times the average sampling interval in time and 2 km in space. Topography-related phase signals were suppressed using a linear correction term estimated between 200 and 10,000 m elevation.

The completeness of the resulting rate maps correlates with topographic roughness (Figures S2a and 2b). While the Tajik depression and the arid eastern Pamir Plateau exhibit a relative high coverage, the deeply incised western Pamir, Tian Shan, and Hindu Kush are mostly void, apart from flat-bottom, formerly glaciated valleys (e.g., Stübner et al., 2017). The obtained deformation rates range between ±15 mm/yr in line-of-sight (LOS) relative to their respective local reference points (red stars in Figures S2a and 2b). Due to data sparsity, the standard rate deviation of the descending frame 005D_053 (Figure S2b) is significantly larger than those of the other frames; we excluded this frame from further processing. The rate uncertainties are between 0.5 and 3.0 mm/yr, with higher uncertainties in the descending acquisition geometry (Figure S3). The highest uncertainties are observed in the Panj valley in the western Pamir and south of the Hindu Kush, where either the topography or a poorly-resolved elevation model foster unwrapping errors. We excluded the area south of the Hindu Kush from further processing, as it also lacks stabilizing GNSS information. The lowest uncertainties are found near the center of each frame at the location of the reference points. These uncertainties only reflect a lower boundary, as they do not take into account atmospheric disturbances or systematic biases caused

by spatial subsampling and soil-moisture variations, which are most problematic in interferograms with a short temporal baselines (Ansari et al., 2021; De Zan et al., 2014), as we further discuss in section 4.3.1. Such biases can be suppressed to some extent if long-baseline interferograms are included in the interferometric network, and full resolution data are processed, which was not applicable in our case. However, we qualitatively estimated the spatial footprint of these biases by the phase-loop closure technique: for each frame, we calculated the mean of closed phase loops, that is, the sum of the interferometric phase difference $_{ij}$ + $_{jk}$ − $_{ik}$, between three acquisition epochs i, j and k, which is supposed to be zero (De Zan et al., 2015). If several of these loops are averaged, a systematic phase bias becomes apparent (Figure S4). For each frame, we calculated and averaged 70–90 phase loops acquired during 2017 to 2020. Significantly, mostly negative phase bias is observed in the Tajik and Ferghana depressions, and the extent of the affected regions is spatially well defined.

Thanks to the dense temporal sampling of the Sentinel-1 radar mission, the outcome of our time-series analysis cannot only be used to derive linear rates, but also to monitor temporal rate anomalies, induced by seasonal processes (Figure S5) or smaller earthquakes (see discussion in chapter 4.3.2). Thus, the noise level and temporal information in InSAR time-series nearly reach the one of daily GNSS time-series, but clearly outperform them in terms of spatial coverage.

3.2 Reference Frame and LOS Rate Decomposition

We collapsed all LOS rate maps with their individual stable reference points (red stars in Figures S2a and S2b) into a supra-regional Eurasia-fixed reference frame, using published survey-mode GNSS data (Ischuk et al., 2013; Kufner et al., 2021; Metzger et al., 2019, 2020, 2021; Mohadjer et al., 2010; Zubovich et al., 2016). During this first processing step, we identified and excluded four GNSS rates in the Tajik depression as outliers (white arrows in Figure 2a). Next, we tied each rate map into the Eurasia-fixed reference frame: we applied a linear ramp to each map to optimize (1) the fit to the horizontal GNSS rates within a search radius of ~4 km (or 10 pixels), and (2) the along-track overlap of two data frames (Ou, 2020) by inverting an over-determined, weighted design matrix, where the GNSS rates were collapsed into LOS (more details are given in the supporting information section S1). After removal of the GNSS outliers, we added seven artificial data points (black squares in Figure 1c) to stabilize the frames covering the southern Hindu Kush, where GNSS data are sparse. Their rates were interpolated from the adjacent stations and their uncertainties were doubled. The individual rate maps descending track 078 and 005 were not fitted to match the along-track overlay, because the data in the overlap area were either too sparse or the deviation was abnormally large (Figure S2b). The resulting rates (Figures S2c and 2d) contain significant offsets across-track, which are mostly due to the sudden LOS change (Figure S6). The westward motion of the western Pamir dominates the ascending rate maps (Figure S2c) with positive values and the descending rate maps (Figure S2d) with negative values. Due to

the right-looking acquisition geometry of the Sentinel-1 satellite, the data are sensitive to about 40, 10, and 50 per cent of the full east, north, and vertical displacement signals. If observations are available from ascending and descending LOS, they can be decomposed (Wright et al., 2004) into east and subvertical components, using a weighted inversion. The subvertical component contains a minor north component, which can be suppressed by subtracting interpolated north rates based on independent GNSS rates (Figure 1c; Ou, 2021).

The resulting displacement rates in the east map agree with the corresponding GNSS data (Figure 2a) and range between -20 to +10 mm/yr in the ITRF2014 Eurasia-fixed reference frame (Altamimi et al., 2017). The vertical rates are in a data-centered reference frame and embrace ±18 mm/yr (Figure 2b). The rates are most coherent in the Tajik and Ferghana depressions and—to some extent—in the eastern Pamir and the Alai valley. Rates in the western Pamir could only be extracted along the Panj-river valley and some of its tributaries. We still observe long-wavelength extrema at the corners and edges of some frames, e.g., in the NW-corner of frames 071A_054 and 100A_050 or the SW-corner of 078D_052 (Figures 1b; markers "1" to "3" in Figure 2a). They are probably due to significant atmospheric contributions in radar scenes, which are used uni-directional, that is, *only* as primary or secondary scenes. The spatial data coverage decreased further after decomposition (Figure S2) to regions covered by both view angles only. The decomposed rate uncertainties—now including the GNSS data uncertainties—are in the range of 0.6–2.6 mm/yr (Figures S7 and S8). In a similar study on Anatolia—with slightly more data, the uncertainties are in the range of 2–3 mm/yr for wavelengths of 50–150 km and a 5-year-long time-series (Weiss et al., 2020; see Figure S7). For our slightly sparser dataset, we assume that local rate changes are significant, if >1.5 mm/yr, and long wavelength signals are significant if >3–5 mm/yr. These estimates are probably still too optimistic for the Panj-river valley, where the interferometric networks are short in time and repeatedly sub-divided, impeding the correct assessment of linear rates (Figure S1), or where too few GNSS data points are available (Hindu Kush). There, the decomposed rate uncertainties are significantly higher than in the rest of the dataset and reach up to 4.5 mm/yr.

The individual ascending and descending rate maps and the final decomposed east and vertical rate maps, both stable to Eurasia (Altamimi et al. 2017) are available as geo-referenced TIF-files in the supplementary information.

4 Results and Discussion

4.1 Rate Map Quality Assessment

Interferometric radar analysis is challenged by several factors. Seasonal vegetation change and (ground) water dynamics introduce a bias, if only short temporal baseline interferograms are used (Figure S4; Ansari et al., 2021), or if the network density is not equally distributed throughout the seasons. Heavy snowfall causes interferometric decorrelation, which may apply in particular for the western Pamir. The partially incomplete digital elevation model (Farr et al.,

2007) of the deeply-incised western Pamir and southern Hindu Kush contains topographic artifacts, which makes interferograms prone to unwrapping errors. Given these obstacles, our LiCSBAS rate maps contain isolated data patches due to spatial and temporal decorrelation (Figure S2), which challenges the combination of the observed rates of several independent acquisition frames into one single reference frame. We overcame this to some extent by tying the rates to the GNSS reference frame, but some sharp jumps along frame boundaries remain; these are in the Afghan platform, the western Ferghana depression, the Dushanbe trough north of the Ilyak fault, and the upper Panj valley (markers "1" to "4" in Figure 2a, respectively). Also, the horizontal rates of ~0 mm/yr observed in the Muksu-river valley in the northern Pamir (Muksu in Figure 2a) are difficult to interpret. Thus, abundant GNSS data are fundamental to correctly transform LOS rate maps into a supra-regional reference frame. For example, the sparse GNSS data in the Hindu Kush do not suffice to stabilize the observed LOS rates correctly—particularly in the region south of the Hindu Kush—and we can only speculate if the long-wavelength signals are rooted in tectonics (Figures 2a and S2).

On a local level, the independent LiCSBAS rate maps offer reliable data to identify km-scale mass movements, which are abundant in this region, but these signals should be confirmed by optical imagery and/or fieldwork. We encourage the reader to make use of the supplementary material for their own specific analyses, as this task exceeds the scope of this paper. When interpreting our results, one must consider the different time periods of data collection (Figure S1). Each individual LOS rate map might be differently affected by moderate-sized earthquake signals or season-dependent near-surface dynamics. The Tajik depression yielded the highest data resolution in space and time, where we have both, dense data and distinct tectonic and non-tectonic signals that can be correlated with independent structural data in high-resolution. We therefore discuss the observations from the Pamir and Hindu Kush in a reconnaissance way and focus on the Tajik depression, in particular the Tajik FTB.

4.2 Pamir and Hindu Kush

In the Eurasia-fixed reference frame, the InSAR rates exhibit westward motion in the order of 10 mm/yr in the western Pamir and the Tajik FTB with a good match to the GNSS-derived east rates (Figure 2a). We assign the large-scale west-directed surface displacements to the westward collapse and lateral extrusion of the Pamir-Plateau crust. North of the Pamir-Tian Shan collision boundary, the Ferghana depression appears relatively stable, as all significant features in the rate maps also appear in the phase-bias map (Figure S3) or collocate with radar frame boundaries (marker "2" in Figure 2a) and hence are artifacts. Along the northern front of the Pamir in the southern Alai valley ("Alai" in Figure 2a), sharp rate changes record the westward-increasing dextral shear at the leading edge of the Pamir, indicating its escape towards the west in addition to the dominant N–S shortening showcased by the GNSS data (Zubovich et al., 2010, 2016). The east-rate map also indicates that part of the

active deformation steps back south of the eastern Alai valley from the Pamir Frontal Thrust and connects to the ~WNW-striking Muji fault (Figure 2a). It remains indistinguishable whether the recorded displacement rates reflect post-seismic activation following the 2016 Sary-Tash and Muji earthquakes (Bie et al., 2018; Feng et al., 2017) or are a long-term signal. Afterslip and relaxation can be excluded, since we excluded data acquired in (at least) the first six months after these two M6 events. In any case, the indicated rates support the transfer of the top-to-west normal slip along the Kongur Shan extensional system of the eastern Pamir (e.g., Robinson et al., 2004; 2007; just outside and southeast of the eastern boundary of Figure 2) via the Muji fault and the Kyzilart transfer zone (marker "a" in Figure 2a) to the Pamir Thrust System and in particular to the deformation front along the Pamir Frontal Thrust (Sippl et al., 2014). The existence of this dextral transfer zone, consisting of the Muji fault and the faults of the Kyzilart transfer zone, that transfer ~E–W crustal extension along the Kongur Shan system to the dextral strike-slip component along the Pamir front, is also implied by the slight divergence of the GNSS velocity field between the eastern Pamir (e.g., Lake Karakul area in Figure 2a) and the Tarim block (Zubovich et al., 2010); north of the transfer zone the GNSS vectors parallel those in the Tarim basin, albeit with much lower rates, reflecting the shortening across the multiple faults of the Pamir Thrust System (Figure 2a). The dextral transfer zone (Muji fault and faults of the Kyzilart transfer zone) implies that the eastern Pamir was involved in the convergence partitioning, here with a westward flow component smaller than that of the western Pamir.

At the northwestern rim of the Pamir, along the Vakhsh valley, sharp east-rate changes of 12–24 mm/yr either imply high landslide activity or—more likely—a shallow locking depth of the evaporite-rooted, dextral-transpressive Vakhsh thrust; the estimated dextral strike-slip rates are 16 ± 3 mm/yr (Metzger et al., 2020). If the Vakhsh thrust is nearly freely creeping, the 1949 M_w7.6 Khait earthquake likely did not rupture the Vakhsh thrust but a structure in the crystalline basement of the Tian Shan.

On first order—and given that the rates measured in the valleys of the Panj and its tributaries are significant, the horizontal rates appear to increase from 5–15 mm/yr westward motion in the eastern Pamir (east of the Sarez-Karakul fault system) to 15–20 mm/yr in the western Pamir; this conforms with the GNSS data (Metzger et al., 2020), and the intense western Pamir seismicity with focal mechanisms that show strike-slip and normal fault solutions with ~E-trending T-axes (Schurr et al., 2014). A minor westward rate increase occurs across the distributed segments of the Sarez-Karakul fault system, e.g., near Lake Sarez (Figure 2a). The implied extensional deformation component accommodated by the Sarez-Karakul fault system agrees with the geological observations of major range-bounding normal faults northeast of Lake Sarez (Officers Range, marker "OR" in Figure 2a; Rutte et al., 2017; Schurr et al., 2014) but contrasts with focal mechanism solutions, which record nearly pure sinistral strike-slip (Metzger et al., 2017; Schurr et al., 2014). However, many short wavelength rate changes correlate with slopes and the systematic bias map (Figure S4). We suspect that

this is not a topographic artifact but rather caused by seasonal, permafrost-related sagging of (or pore-pressure changes in) unconsolidated material (e.g., Rouyet et al., 2019); we extensively mapped such features that formed as a result of the 2015 Sarez earthquake (Figure 2a shows the modeled rupture trace from Metzger et al., 2017).

The northeastern Hindu Kush of Badakhshan (Figure 1a), with reliable data along the Kokcha-river valley (marker "b" in Figure 2a), exhibits nearly as high westward rates (7–12 mm/yr) as the eastern Tajik FTB (8–15 mm/yr) and the western Pamir (marker "c" in Figure 2a, 16–26 mm/yr). No modern structural information is available for the faults and folds mapped in the northwestern Hindu Kush, but the highest rate changes coincide with thrust-cored folds along the southeastern margin of the Tajik FTB, involving Pliocene strata (Figure 3a; Doebrich & Wahl, 2006; own unpublished mapping). In contrast, the western Hindu Kush—including the Afghan platform—appears to be horizontally mostly stable with respect to Eurasia (west of marker "b" in Figure 2a, 0 ± 2 mm/yr).

We observe strong uplift of 10–17 mm/yr in the westernmost Pamir (along the Panj valley and west of it), and easternmost Tajik FTB where its eastern erosional edge is cut by the Darvaz fault zone (marker "d" in Figures 2b and 3b); this area coincides with the area of rapid westward motion (marker "c" in Figure 2a; see interpretation below). A N–S gradient—with uplift rates of 4–6 mm/yr—occurs at the southern margin of the Tajik depression at its transition to the Afghan platform (marker "e" in Figure 2b). This area south of the Amu Darya–Panj-river valley, marks the interaction and transition from the ~E–W shortening of the Tajik FTB to the ~NW–SE shortening within the Afghan platform, implied by earthquake focal mechanism (e.g., Supplementary Figure S5 in Kufner et al., 2021; McNab et al., 2019), and the appearance of ~E-striking faults, e.g., the dextral-oblique thrust in the Alburz-Marmul fault zone (Figure 1a).

The whole northeastern Hindu Kush and southwestern Pamir are located above steeply-dipping lithospheric slabs; their position in the mantle is outlined by the intermediate-depth earthquakes in Figures 1a and 2a (e.g., Kufner et al., 2016, 2017, 2021; Zhan & Kanamori, 2016). The Pamir slab starts to bend down from west to east beneath the eastern Tajik FTB (Figures 6 and 7 in Schneider et al., 2019; crustal-scale cross section in Figure 18c of Gągała et al., 2020) and likely laterally terminates in the south where strong uplift (marker "d" in Figure 2b) gives way to subsidence in the northeastern Hindu Kush (marker "f" in Figure 2b). The Hindu Kush slab is subducting northward, dips steeply north to vertical, and is in the process of stretching and tearing in its eastern part (Kufner et al., 2017, 2021). The boundary between the mantle parts of the two slabs is clearly outlined by the intermediate-depth earthquakes in the southwesternmost Pamir (Hindu Kush slab: purple dots; Pamir slab: pink dots in Figure 2). It is difficult to assess, whether these deep-seated processes are reflected in our rate maps. InSAR radar satellite antennas are most sensitive to vertical motions, but subtle rate changes across several tens—if not hundreds of

kilometers—are challenging to correctly retrieve. Our observation of regional, 0–4 mm/yr subsidence of the northeastern Hindu Kush (marker "f" in Figure 2b) above and north of the Hindu Kush slab, and in particular the marked contrast to the 10–17 mm/yr uplift in the easternmost Tajik FTB (marker "d" in Figure 2b) likely record these lithosphere processes. The region where the crust of the Tajik depression bends down, forming the footwall of the western Pamir (crustal scale buckling in profile along latitude 38°N in Figure 6 of Schneider et al., 2019; Gągała et al., 2020), likely constitutes a crustal-scale antiform about a ramp, causing uplift. It possibly induces subsidence in the southwestern Pamir where the back-rolling Pamir slab is vertical (Kufner et al., 2016). The north-dipping to subvertical, back-rolling Hindu Kush slab possibly induces the subsidence in the Hindu Kush (marker "f" in Figure 2b): there, subsidence of up to 4 mm/yr changes to uplift at the western end of the slab where it is intact (boundary between markers "e" and "f") and subsidence possibly changes to modest uplift at the slab's eastern end, where the break-off has progressed most (Kufner et al., 2021). We interpret the pronounced patches of 20–40 mm/yr subsidence south of markers "e" along the Kunduz-river valley as anthropogenically-caused (Figure 2b; see section 4.3.1 for equivalent subsidence along the valleys of the Tajik depression). We interpret the general 10 mm/yr subsidence south of marker "f" and south of the eastern part of marker "e" as a tectonic signal caused by the Hind Kush slab; there, Kufner et al. (2021) tomographically mapped its down-bending towards its subvertical position in the mantle marked by the purple earthquakes.

4.3 Active Structures in the Tajik Fold-thrust Belt

The rates in the Tajik FTB are interpreted in combination with seismicity (Kufner et al., 2018) and the structural geometries, derived from surface, seismic, and borehole data (Gągała et al., 2020). In addition to the map view (Figure 3), we projected the horizontal and vertical rates onto four geological cross-sections within 5 km swaths (Figures 4a and 4b; cross-section traces in Figure 3), and into a detailed east-rate map and an oblique-crossing profile of the Ilyak fault (Figure 5; frame in Figure 3a). In addition, we compared the rates to topographic profiles and percentage of arable land, both computed within 5 km swaths (Figures 4a and 4b).

4.3.1 Non-tectonic Signal

Herein, we outline the non-tectonic signal, that is systematic subsidence, by land classification data based on Landsat 8 optical imagery (MDA US BaseVue, 2013); land classified as arable correlates well with the systematic soil-moisture bias map (Figure S4). We marked the major agricultural areas by polygons framed thick-white (Figure 3b) respectively shaded in green (Figures 4a and 4b). The vertical rate maps of Figures 2b and 3b outline stripes with >15 mm/yr subsidence as the most outstanding feature of the Tajik depression; the strongest subsidence signal follows the major river valleys of the Tajik depression, which host intense agriculture. The observed subsidence is most likely caused by precipitation-induced soil-moisture changes (Ansari et al., 2021; De

Zan et al., 2014). Rainfall causes rapid pore filling and simultaneous soil uplift (Gabriel et al., 1989), which often leads to unwrapping errors in interferograms. The consequent, slow dehumidification (see, e.g., Figure 2 of Albertson & Kiely, 2001), on the other hand, is correctly imaged in interferograms, thus biasing the vertical rates derived from the time-series analysis towards the negative. This bias could be enhanced by water extraction due to the extensive irrigation in the summer months, during which most of the used radar scenes were acquired; a more detailed study of these signals lies beyond the scope of this work. In the horizontal rates, the agricultural areas often coincide with a high measurement scatter, although without any systematic component. A second conspicuous vertical signal—but this time positive—is correlated with major rivers and related to water level increase during hinterland snow melt (e.g., marker "g" in Figure 3b). The distinct, patchy subsidence in the region between the fossil and active (Hoja Mumin) salt diapirs in the southeastern Tajik FTB and the Nurak water reservoir (markers "HM" and "NR" in Figure 2b) may be an affect of salt tectonics (Figure 11 of Gągała et al., 2020). But it is also correlates to arable land that has not been properly classified in the Landsat 8 data.

The highest deformation rates occur at the Hoja Mumin salt fountain, where we observed local uplift of ~50 mm/yr at its top, surrounded by up to ~120 mm/yr of subsidence and lateral outflow of ~350 mm/yr to the west and ~170 mm/yr to the east. These rates confirm the recent activity of this salt fountain, as documented by Leith & Simpson (1986), Dooley et al. (2015), and Gągała et al. (2020). We also observed localized uplift at the shores of the Nurak reservoirs (and smaller reservoirs downstream; marker "NR" in Figure 2b and cross-sections A and B in Figure 4a) that is probably related to elastic rebound caused by reservoir-volume changes, as observed elsewhere (e.g., Cavalié et al., 2007; Neelmeijer et al., 2018).

4.3.2 Tectonic Signal

The unambiguous horizontal tectonic signal consists of long-wavelength trends. Foremost, the bulk of the Tajik FTB accommodates westward motion (map view in Figure 3a, cross-sectional view in Figures 4a and 4b). Characteristically, the horizontal displacement rates are not affected by the vergence of the fold-thrust structures in the Tajik FTB; in particular, the Yavan synclinorium—the zone of vergence change—is showing similar horizontal rates as the bounding Kafirnigan and Vakhsh anticlinoria. Therefore, the Yavan synclinorium must be—at least at present—entirely detached from its original substratum. Chapman et al. (2017) postulated that the east-vergent western Tajik FTB is part of the greater Tian Shan orogenic system, distinct from the eastern Tajik FTB whose shortening is linked to the Pamir, with the Yavan synclinorium being a remnant foreland common to both fold-thrust systems; again—at least at present—the west-directed rates indicate the detachment of the entire Tajik FTB as part of the outward-growing Pamir orogenic system.

The west-directed displacement rates decay away from the Pamir: Figure 3a shows—in average—higher westward displacements in the part of the Tajik FTB

adjacent to the Pamir than away from it. Cross-sections B and C in Figures 4a and 4b illustrate this pattern (envelope 'A' in the horizontal displacement profiles), while in cross-sections A and D this trend is not convincing. We interpret this decrease by the gradual dissipation of the west-directed motion across the salt-rooted structures; however, this effect is subordinate to the coherent westward displacement of the whole Tajik FTB. The rates decrease and become less systematic towards south (cross-sections A–C versus D; Figures 4a and 4b), suggesting active, northward-increasing, anti-clockwise vertical-axis rotations in the Tajik FTB, in agreement with the sense of past rotations evidenced by paleomagnetic data (Pozzi & Feinberg, 1991; Thomas et al., 1994).

In detail, the horizontal displacement profiles often show a saw-blade pattern (Figures 4a and 4b). These short-wavelength perturbations stand out across the Kafirnigan anticlinorium, where positive spikes—reaching up to 10 mm/yr above the regional background—are centered over scarp slopes of east-facing hogback ridges ("E" markers placed over the horizontal displacement profiles in cross-section A–C; Figures 4a and 4b). Figure 6a highlights these short-wavelength anomalies in a high-pass filtered map of horizontal rates that suppresses the regional component: the east-facing scarp slopes ("E" markers) show narrow but pronounced positive, the west-facing slopes negative, albeit less pronounced horizontal displacement anomalies. The divisions between the local positive and negative anomalies follow the crests of the topographic ridges, suggesting divergent ground motions across the ridge crests. We interpret the short-wavelength saw-blade patterns—superimposed on the regional displacement profiles—as related to gravitationally-induced mass movements (slope sagging or creep). Due to the homoclinal structure of the hogback ridges in the Kafirnigan anticlinorium, the east-facing scarp slopes incise older strata, including mass-movement prone Cenomanian-Campanian shale, marl, limestone, and evaporites, while the west-facing ones follow sandstone- and conglomerate-dominated Oligocene-Neogene strata with less mass-movement susceptibility; this likely causes the faster ground motion on eastern than western slopes. Figure 6b provides structural evidence for northwest-directed mass movement, albeit without age control: along a steeply west-dipping slope in the ~NW-dipping strata of the Karshi anticline—east of the Babatag anticline, an Upper Cretaceous shale-gypsum sequence shows dominantly ~NW-directed normal faulting, with the faults planes and numerous tension gashes infiltrated/lubricated by gypsum.

Across the frontal anticline of the Vakhsh anticlinorium, where the hogback ridges face west due to the change of the structural polarity across the Yavan synclinorium, this relationship seems to be reversed: there, the west-facing scarp slopes ("W" markers in cross-sections B and C of Figures 4a and 4b; Figure 6a) correlate with negative displacement spikes. This indicates that a local west-directed displacement component adds up to the regional displacement. We propose the same explanation as for the Kafirnigan anticlinorium, i.e., variable susceptibility of the slopes to mass movements; however, the relationship is more diffuse in the Vakhsh than in the Kafirnigan anticlinorium, possibly due to the complex surface geology, in particular the presence of incised hanging-wall

anticlines.

An abrupt ~5 mm/yr change in the horizontal displacement rates occurs across the Ilyak fault and the Babatag thrust (Figures 2a, 3a, 4a, and 5). The Babatag thrust accommodates an abrupt arrest of the Tajik FTB's westward motion. It is the most prominent structure of the Tajik FTB in terms of the amount of shortening with total displacement exceeding 20 km over the past ~12 Ma in its northern segment; total displacement drops to ~10 km in the south (Gągała et al., 2020). The horizontal velocity contrast across this thrust is ~5 mm/yr all along strike, although the velocity gradient in the north (cross-sections B and C, Figures 4a and 4b) is higher than in the south (cross-section D). The absolute numbers indicate a passive hanging wall and actively underthrusting footwall. The dip of the Babatag thrust—constrained by boreholes—is ~15° (Gągała et al., 2020), hence, the horizontal underthrusting at ~5 mm/yr should resolve in ~1.3 mm/yr vertical displacement of the hanging wall; such an uplift anomaly is not evident, probably due to its low value compared to the noise. Recent activity of the Babatag thrust may independently be indicated by geomorphology: Figure S9 shows a series of 500-m-wide swath profiles along selected stream trunks. Most of the profiles display knickpoints, possibly indicating topographic perturbations due to slip along the Babatag thrust; the most affected stream profiles (2, 3, 5 in Figure S9) face an exposed portion of the Babatag thrust where it overrides Quaternary alluvia. However, due to the resolution of the current-state of geological mapping (scale 1:200,000), we cannot assess the effect of lithological changes on the position of the knickpoints in detail.

Cross-section A in Figure 4a shows and Figure 5 details the transition of the Tajik FTB to the Dushanbe trough, which is involved in the moderate ~N–S shortening of the Tian Shan to the north (Käßner et al., 2016; Gągała et al., 2020). Figure 5 shows the structures, seismicity, and east-rate changes across the Ilyak fault southeast of Dushanbe, where the fault exhibits a horizontal rate change within a corridor of 4 km. In an elastic screw dislocation model, 50 % of the fault's relative motion should occur in a corridor of twice its locking depth (Savage & Burford, 1973); this would suggest that the fault is locked at <1 km depth, if not—given the spatial sampling of ~450 m and the strong filtering of the original interferograms—freely creeping as suggested by InSAR LOS rate maps produced by higher spatial sampling (Wilkinson et al., 2020). Dextral slip varies along strike and decreases from ~10 mm/yr in the east to ~5 mm/yr in the west (Figures 5a and 5b). Seismicity is sparse except for an area ~20-km west of Dushanbe, where the focal mechanisms suggest dextral shear (Figure 5a; Kufner et al., 2018). This is where the fault changes strike and several thrusts of the Kafirnigan anticlinorium enter the Ilyak fault, forming transpressive shear lenses, imbricating Lower Cretaceous to Pliocene rocks.

We have no direct structural information on the Ilyak fault, mostly due its strong anthropogenic overprint. The data at the three sites in Figure 5c characterize the northern edge of the Dushanbe trough and the Vakhsh anticlinorium south and north of the Ilyak fault. Pure top-to-south thrusting emplaced the

crystalline basement of the Tian Shan on Cretaceous limestone at station 1893A at the northern rim of the Dushanbe trough; the age of thrusting is unknown but younger than ~10 Ma (Käßner et al., 2016). The lack of a strike-slip signal supports our earlier interpretation that the band of westward displacement signal, coinciding with a series of thrusts farther east, is an artifact (marker "3" in Figure 2a). The ~NE-striking fault east of Dushanbe, well-expressed topographically and forming a clear boundary between agricultural and pastural land, appears to accommodate westward displacement rates of up to 5 mm/yr. The two sites (Figure 5c) in the Vakhsh anticlinorium south of the Ilyak fault characterize that part of the Tajik FTB where the overall ~N-striking thrusts progressively bend into the Ilyak fault zone. Characteristically, the thrusts have dextral-transpressive top-to-(N)NW kinematics; these faults accommodate horizontal rate changes of a few mm/yr. Our data neither support nor disprove the hypothesis that the 1907 M_s7.6 ± 0.3 Kharatag earthquake occurred on a locked fault near Dushanbe (Kondorskaya & Shebalin, 1982).

An obvious but small active structure is a ~N-striking fault south of the conjunction of Vakhsh, Panj, and Kunduz rivers that exhibits frequent seismicity and where the hanging wall exhibits increased west-directed motion (marker "h" in Figure 3). Its surface trace reaches a length of ~15 km but may be connected with a similar structure north of the Amu Darya, also hosting a cluster of seismicity and two focal mechanism solutions that indicate slip along ~N-striking subhorizontal planes (Kufner et al., 2018). The original time-series of a pixel selected in the hanging wall captured about ~3 cm of slip towards ascending LOS after a 2017, January 9, M_w5.2 earthquake (event 201701090559A, Ekström et al., 2012; Figure S5). Our kinematic observations are in agreement with the double couple solution from the Global Centroid Moment Tensor catalog that reports thrusting on a ~46°-dipping plane on a ~SSE-striking fault (marked in orange and labeled by magnitude; Figure 3). The epicenter, however, is ~15 km west of the cluster of earthquakes (Kufner et al., 2018). We consider the structure to be part of the southernmost Kafirnigan anticlinorium, where it bends from a ~N to a ~SE strike, marking the southern margin of the Tajik FTB.

Extremely rapid westward motion occurs west of the Darvaz fault zone, at the eastern erosional edge of the Tajik FTB, where westward rates reach 16–26 mm/yr (marker "c" in Figures 2a; Figure 3a; markers "I" in Figure 4a); these high rates can be observed from the Peter I. Range in the north all the way to west of the Kokcha river in Badakhshan in the south, interrupted by a relatively stable area and with pure signal along the Panj valley. Vertical uplift rates also increase towards the Darvaz fault reaching 10–17 mm/yr (marker "d" in Figure 2b; envelopes B in Figures 4a and 4b; see section 4.2). The area of rapid uplift coincides with high topography, developed in often weakly-consolidated Neogene coarse-grained terrestrial strata (Figure 4, topographic swath profiles). From our uncertainty analysis (Figures S4, S7, and S8), we can exclude atmospheric or near-surface contributions to these rates, thus they are of tectonic origin. Both the high horizontal rates and the Pamir-ward increase of the vertical uplift rates support the earlier given interpretation (section 4.2) of a tectonic stack

above a ramp, caused by ongoing indentation of the leading edge of the Pamir below this marginal part of the Tajik depression, resulting in a passive roof uplift. This, however, appears inconsistent with the modern sinistral kinematics of the Darvaz fault (Kufner et al., 2018; Metzger et al., 2020). We favor an interpretation of slip partitioning, with top-to-WNW thrusting of the Pamir's buried leading edge being kinematically decoupled by the sinistral Darvaz fault from the Pamir hinterland. We envision a similar displacement partitioning as described for the deformation at the northern edge of the Pamir, east of the Alai valley (section 4.2): there, dominant northward motion is accommodated by the large thrusts of the Pamir Thrust System (with the recent Nura and Sary-Tash earthquakes) and subordinate dextral strike-slip faults, the Muji fault and the Kyzilart transfer zone (with the recent Muji earthquake), that accommodate the westward escape of the Pamir. In this scenario, the thrusts and strike-slip faults at the eastern edge of the Tajik FTB would partition deformation in northward motion along the Darvaz fault zone (and parallel faults in the western Pamir) and westward motion along the thrusts.

If significant, the westward acceleration of the horizontal rates west of the Darvaz fault zone (marker "c" in Figures 2a) would imply ongoing extension along the eastern border of the displacement anomaly and concomitant shortening along its western border, a pattern typical for gravity-driven deformation. Past extension is indeed evidenced by likely Neogene graben fills in the Darvaz fault zone (Gągała et al. 2020), but we are lacking structural and geomorphic data to confirm that such a process is operating today. We interpret the eastern edge of the Tajik FTB as the western margin of the province with strike-slip and normal fault focal mechanisms that indicate ~E–W extension across the western Pamir (Schurr et al., 2014). The westward accelerating rates may indicate the zone where the crust of the topographically-high western Pamir Plateau acquires a component of westward gravitational sliding being transferred from the crustal ramp to the salt-décollement of the Tajik FTB.

There is a conspicuous westward horizontal rate increase of up to 7 mm/yr across a ~NNE-trending watershed between the Panj and the Kokcha rivers that seems to be a true kinematic signal (marker "j" in Figures 2a and 3a); towards east, rates increase again to ~8 mm/a westward movement (southern extension of marker "c" in Figure 2a), which we interpreted above as due to a component of westward gravitation sliding along the at the western margin of the Pamir Plateau. The boundary of accelerated westward motion at marker "h" coincides with the transition from the west-vergent thrust-folds with thick Neogene hanging-wall strata to the area in the southeastern Tajik FTB that is governed by salt-tectonics (marker "H" in cross-section D of Figure 4b). The box-shaped antiform with a >25-km wavelength, cored by up to 5-km-thick evaporites and a salt diapir at its western tip west of marker "H", may indicate a zone of enhanced westward flow feeding the various thrusted detachment folds with thick evaporite cores farther west. This indicates that parts of the buried salt structures of the southeastern Tajik FTB may—besides the Hoja Mumin salt fountain—are active; the strong anthropogenic overprint prohibits

an interpretation of the vertical displacements but as in the area between the Nurak reservoir and Hoja Mumin salt fountain, the subsidence signal features a distinct, patchy pattern.

5 Conclusions

The interferometric rate maps of the greater Pamir area exhibit large-scale tectonic features, ground subsidence due to water level changes, salt tectonics, and mass movements. Rate interpretation is limited by data sparsity of the underlying interferometric network in time and space. Single interferograms of poor quality might significantly influence the 13 derived relative rate maps in LOS. The GNSS data play a key role to correctly tie the rate maps to a supra-regional, Eurasian-fixed reference frame and the decomposition of the LOS rates into east and vertical rates, particularly for long-wavelength signals. The GNSS data quality is somewhat limited, as the database contains only horizontal rates, derived from repeated, annual surveys in difficult terrain and confined by topography. The temporal resolution and accuracy of InSAR time-series (in line-of-sight) nearly equals daily GNSS solutions today and are able to reproduce ephemeral and seasonal processes. We discussed the most conspicuous tectonic and anthropogenic features, and linked them to the seismicity, and the geologic structures formed over the last ~12 Ma.

The displacement-rate maps highlight the 3-D geometry of large parts of the northwestern orogenic margin of the India-Asia collision zone, with crustal material flowing laterally (westward) out of the N–S collision zone. The west-directed lateral extrusion rates increase from east to west from the eastern to the western Pamir and decrease from ~20 to 5 mm/yr westward across the Tajik fold-thrust belt, dissipating over the salt-rooted structures. On the first-order, the modern shortening rates across the Tajik fold-thrust belt (20–5 mm/yr) correspond to the 12–8 mm/yr long-term shortening rates (148–93 km shortening over 12 Myr) in the north-central and southern Tajik fold-thrust belt, determined from line-length restoration and thermochronology. Characteristically, the modern westward rates are not affected by the vergence of the Tajik fold-thrust belt structures, in particular the Yavan synclinorium—the zone of vergence change; therefore, the entire Tajik fold-thrust belt is detached from its original substratum. The modern kinematics thus shows that the Tajik fold-thrust belt is a depression-wide, thin-skinned belt developed above an evaporitic décollement, whose evolution is governed by the westward growth of the Pamir orocline. A short-wavelength saw-blade pattern—superimposed on the regional horizontal displacement profiles—is interpreted as related to mass movements on steeply-dipping slopes of structurally controlled hogback ridges.

Abrupt ~6 mm/yr changes in the horizontal rates occur across the kinematically-linked dextral Ilyak strike-slip fault bounding the Tajik fold-thrust belt to the north and the Babatag thrust, the major thrust of the fold-thrust belt, located far west in the belt. The dextral slip or creep rates on the Ilyak fault are of 5–10 mm/yr, decreasing towards west; the locking depth of the fault is 1 km.

The vertical and horizontal rates of the southeastern Tajik fold-thrust belt are laterally diverse with a distinct, patchy displacement signal, in particular in the region with salt tectonics, where upright detachment anticlines and bivergent thrust sheets pointing at an unconfined detachment. The highest displacement rates occur at the Hoja Mumin salt fountain, where we observed local uplift of ~50 mm/yr at its top, surrounded by up to ~120 mm/yr of subsidence and lateral outflow of ~350 mm/yr to the west and ~170 mm/yr to the east.

The vertical rate map outlines stripes with >15 mm/yr subsidence as the most outstanding feature of the Tajik depression; the strongest subsidence signal follows the major river valleys of the Tajik depression, which host intense agriculture. The subsidence is likely caused by a combination of a bias related to soil-moisture changes (slow dehumidification) and water extraction for the extensive irrigation. In addition, we observed strong uplift of 10–17 mm/yr in the western Pamir, and easternmost Tajik FTB where its eastern erosional edge is cut by the broad Darvaz fault zone. Both the high horizontal rates and the Pamir-ward increase of the vertical uplift rates support the existence of a crustal-scale antiform above a ramp caused by ongoing indentation of the leading edge of the Pamir below this marginal part of the Tajik depression, resulting in a passive roof uplift.

Acknowledgments

Qi Ou advised us on how to tie multiple InSAR rate maps to GNSS data. Some figures were created using GMT (Wessel et al., 2013) and colormaps of Crameri (2020). LiCS data (Looking into the Continents from Space, https://comet.nerc.ac.uk/comet-lics-portal/) contains modified Copernicus Sentinel data analyzed by COMET, the Centre for the Observation and Modelling of Earthquakes, Volcanoes and Tectonics, using JASMIN, the UK's collaborative data analysis environment (http://jasmin.ac.uk). Atmospheric phase delay maps were provided by the Generic Atmospheric Correction Online Service for InSAR (https://www.gacos.net). The code for the LiCSBAS time-series analysis is available at https://github.com/yumorishita/LiCSBAS. GNSS rate tables are published as mentioned in the main text. The individual and the final, decomposed rate maps and uncertainties are provided in the Supporting Material. Funded by the Helmholtz Center, German Research Center for Geosciences, Potsdam, the German Research Council (DFG) grant RA 442/41, and the German Ministry of Science and Education within the CaTeNA project (support 3G0878A).

References

Abdulhameed, S., Ratschbacher, L., Jonckheere, R., Gągała, Ł., Enkelmann, E., Käßner, A., et al. (2020). Tajik Basin and Southwestern Tian Shan, Northwestern India-Asia Collision Zone: 2. Timing of Basin Inversion, Tian Shan Mountain Building, and Relation to Pamir-Plateau Advance and Deep India-Asia Indentation. *Tectonics*, *39*(5), e2019TC005873 https://doi.org/10.1029/2019TC005873

Albertson, J. D. & Kiely, G. (2001). On the structure of soil moisture time series in the context of land surface models, *Journal of Hydrology*, *243*, 1–2, 101–119. https://doi.org/10.1016/S0022-1694(00)00405-4

Altamimi, Z., Métivier, L., Rebischung, P., Rouby, H., & Collilieux, X. (2017). ITRF2014 plate motion model. *Geophysical Journal International*, *209*(3), 1906–1912. https://doi.org/10.1093/gji/ggx136

Ansari, H., De Zan, F., & Parizzi, A. (2021). Study of Systematic Bias in Measuring Surface Deformation with SAR Interferometry. *IEEE Transactions on Geoscience and Remote Sensing*, *59*(2), 1285–1301. https://doi.org/10.1109/TGRS.2020.3003421

Bekker, Y.A. (1996). Tectonics of the Afghan–Tadjik Depression (russ.), *Geotektonika*, *30*(1), 76–82.

Bie, L., Hicks, S., Garth, T., Gonzalez, P., & Rietbrock, A. (2018). 'Two go together': Near-simultaneous moment release of two asperities during the 2016 Mw 6.6 Muji, China earthquake, *Earth and Planetary Science Letters*, *491*, 34–42. https://doi.org/10.1016/j.epsl.2018.03.033

Bloch, W., Metzger, S., Yuan, X., Xu, Q., Zhao, J., Schurr, B. (2019). Strain evolution and stress transfer during a 2-years earthquake sequence in the Pamirs, *American Geophysical Union*, Fall Meeting 2019, #G41B-0732.

Bourgeois, O., Cobbold, P. R., Rouby, D., Thomas, J.-C. J., & Shein, V. (1997). Least squares restoration of Tertiary thrust sheets in map view, Tajik depression, central Asia, *Journal of Geophysical Research*, *102*(B12), 27553–27573. https://doi.org/10.1029/97JB02477

Burtman, V. S., & Molnar, P. (1993). Geological and Geophysical Evidence for Deep Subduction of Continental Crust Beneath the Pamir. *Geological Society of America Special Paper*, *281*, 1–76. https://doi.org/10.1130/SPE281

Cavalié, O., Doin, M.-P. P., Lasserre, C., & Briole, P. (2007). Ground motion measurement in the Lake Mead area, Nevada, by differential synthetic aperture radar interferometry time series analysis: Probing the lithosphere rheological structure, *Journal of Geophysical Research: Solid Earth*, *112*(B3), 1–18. https://doi.org/10.1029/2006JB004344

Chapman, J.B., Carrapa, B., Ballato, P., DeCelles, P.G., Worthington, J., Oimahmadov, I., Gadoev, M., Ketcham, R. (2017). Intracontinental subduction beneath the Pamir Mountains: Constraints from thermokinematic modeling of shortening in the Tajik fold-and-thrust belt, *GSA Bulletin*, *129*(11–12), 1450–1471. https://doi.org/10.1130/B31730.1

Chen, C. W., & Zebker, H. A. (2002). Phase unwrapping for large SAR interferograms: Statistical segmentation and generalized network models, *IEEE Transactions on Geoscience and Remote Sensing*, *40*(8), 1709–1719. https://doi.org/10.1109/TGRS.2002.802453

Crameri, F. (2020). Scientific color maps (Version 6.0.4). https://doi.org/10.5281/zenodo.4153113

De Zan, F., Parizzi, A., Prats-Iraola, P., & López-Dekker, P. (2014). A SAR interferometric model for soil moisture, *IEEE Transactions on Geoscience and Remote Sensing*, *52*(1), 418–425. https://doi.org/10.1109/TGRS.2013.2241069

De Zan, F., Zonno, M., & López-Dekker, P. (2015). Phase Inconsistencies and Multiple Scattering in SAR Interferometry, *IEEE Transactions on Geoscience and Remote Sensing*, *53*(12), 6608–6616. https://doi.org/10.1109/TGRS.2015.2444431

Doebrich, J. L., & Wahl R. R. (Compilators) (2006). Geological and mineral resource map of Afghanistan; Version 2. *U.S. Geol. Surv. Open File Rep.*, 2006–1038.

Doin, M.-P., Lodge, F., Guillaso, S., Jolivet, R., Lasserre, C., Ducret, G., et al. (2011). Presentation of the small baseline NSBAS processing chain on a case example: the Etna deformation monitoring from 2003 to 2010 using Envisat data, *Proceedings of the ESA Fringe 2011 Workshop*, Frascati, Italy, 19–23.

Dooley, T. P., Jackson, M. P. A., & Hudec, M. R. (2015). Breakout of squeezed stocks: Dispersal of roof fragments, source of extrusive salt and interaction with regional thrust faults, *Basin Research*, *27*(1), 3–25. https://doi.org/10.1111/bre.12056

Efron, B., & Tibshirani, R. (1986). Bootstrap Methods for Standard Errors, Confidence Intervals, and Other Measures of Statistical Accuracy, *Statistical Science*, *1*, 54–75. https://doi.org/10.1214/ss/1177013815

Ekström, G., Nettles, M., & Dziewonski, A. M. (2012). The global CMT project 2004-2010: Centroid-moment tensors for 13,017 earthquakes, *Physics of the Earth and Planetary Interiors*, *200–201*, 1–9. https://doi.org/10.1016/j.pepi.2012.04.002

Elliott, A., Elliott, J., Hollingsworth, J., Kulikova, G., Parsons, B., & Walker, R. (2020). Satellite imaging of the 2015 M 7.2 earthquake in the Central Pamir, Tajikistan, elucidates a sequence of shallow strike-slip ruptures of the Sarez-Karakul fault, *Geophysical Journal International, 221*(3), 1696–1718. https://doi.org/10.1093/gji/ggaa090

Evans, S. G., Roberts, N. J., Ischuk, A., Delaney, K. B., Morozova, G. S., & Tutubalina, O. (2009). Landslides triggered by the 1949 Khait earthquake, Tajikistan, and associated loss of life, *Engineering Geology*, *109*(3–4), 195–212. https://doi.org/10.1016/j.enggeo.2009.08.007

Farr, T. G., Rosen, P. A., Caro, E., Crippen, R., Duren, R., Hensley, S., et al. (2007). The Shuttle Radar Topography Mission, *Review of Geophysics*, *45*(RG2004), 248. https://doi.org/10.1029/2005RG000183

Feng, W., Tian, Y., Zhang, Y., Samsonov, S., Almeida, R., & Liu, P. (2017). A

Slip Gap of the 2016 Mw6.6 Muji, Xinjiang, China, Earthquake Inferred from Sentinel-1 TOPS Interferometry. *Seismological Research Letters*, *88*(4), 1054–1064. https://doi.org/10.1785/0220170019

Funning, G. J., Garcia, A. (2019). A systematic study of earthquake detectability using Sentinel-1 Interferometric Wide-Swath data, *Geophysical Journal International*, *216*(1), 332–349, Figure S23 in the supporting information. https://doi.org/10.1093/gji/ggy426

Gabriel, A. K., Goldstein, R. M., and Zebker, H. A. (1989). Mapping small elevation changes over large areas: Differential radar interferometry, *Journal Geophysical Research*, *94*(B7), 9183– 9191, https://doi.org/10.1029/JB094iB07p09183

Gareth, J. F., Garcia, A. (2019). A systematic study of earthquake detectability using Sentinel-1 Interferometric Wide-Swath data, *Geophysical Journal International*, *216*(1), 332–349. https://doi.org/10.1093/gji/ggy426

Gągała, Ł., Ratschbacher, L., Ringenbach, J. C., Kufner, S.-K., Schurr, B., Dedow, R., et al. (2020). Tajik Basin and Southwestern Tian Shan, Northwestern India-Asia Collision Zone: 1. Structure, Kinematics, and Salt Tectonics in the Tajik Fold-and-Thrust Belt of the Western Foreland of the Pamir, *Tectonics*, *39*(5), e2019TC005871. https://doi.org/10.1029/2019TC005871

Goldstein, R. M., & Werner, C. L. (1998). Radar interferogram filtering for geophysical applications, *Geophysical Research Letters*, *25*(21), 4035–4038. https://doi.org/10.1029/1998GL900033

He, P., Hetland, E.A., Niemi, N.A., Wang, Q., Wen, Y. and Ding, K. (2018). The 2016 Mw6.5 Nura earthquake in the Trans Alai range, northern Pamir: possible rupture on a back-thrust fault constrained by Sentinel-1A radar interferometry, *Tectonophysics*, *749*, 62–71. https://doi.org/10.1016/j.tecto.2018.10.025

Hooper, A., Segall, P., & Zebker, H. (2007). Persistent scatterer interferometric synthetic aperture radar for crustal deformation analysis, with application to Volcán Alcedo, Galápagos, *Journal of Geophysical Research: Solid Earth*, *112*(7), 1–21. https://doi.org/10.1029/2006JB004763

Ischuk, A., Bendick, R., Rybin, A., Molnar, P., Khan, S. F., Kuzikov, S., et al. (2013). Kinematics of the Pamir and Hindu Kush regions from GPS geodesy, *Journal of Geophysical Research: Solid Earth*, *118*(5), 2408–2416. https://doi.org/10.1002/jgrb.50185

Jepson, G., Glorie, S., Konopelko, D., Gillespie, J., Danišık, M., Evans, N. J., et al. (2018). Thermochronological insights into the structural contact between the Tian Shan and Pamirs, Tajikistan, *Terra Nova*, *30*, 95–104. https://doi.org/10.1111/ter.12313

Käßner, A., Ratschbacher, L., Jonckheere, R., Enkelmann, E., Khan, J., Sonntag, B.-L., et al. (2016). Cenozoic intracontinental deformation and exhumation at the northwestern tip of the India-Asia collision—southwestern

Tian Shan, Tajikistan, and Kyrgyzstan, *Tectonics*, *35*(9), 2171–2194. https://doi.org/10.1002/2015TC003897

Kondorskaya, N., & Shebalin, N. (chief editors). (1982). New Catalog of Strong Earthquakes in the U.S.S.R. from Ancient Times Through 1977, Report SE31, *World Data Center A for Solid Earth Geophysics*, 609.

Kufner, S.-K., Schurr, B., Sippl, C., Yuan, X., Ratschbacher, L., son of Mohammad Akbar, A., et al. (2016). Deep India meets deep Asia: Lithospheric indentation, delamination and break-off under Pamir and Hindu Kush (Central Asia), *Earth and Planetary Science Letters*, *435*, 171–184. https://doi.org/10.1016/j.epsl.2015.11.046

Kufner, S.-K., Schurr, B., Haberland, C., Zhang, Y., Saul, J., Ischuk, A., & Oimahmadov, I. (2017). Zooming into the Hindu Kush slab break-off: a rare glimpse on the terminal stage of subduction, *Earth and Planetary Science Letters*, *461*, 127–140. https://doi.org/10.1016/j.epsl.2016.12.043

Kufner, S.-K., Schurr, B., Ratschbacher, L., Murodkulov, S., Abdulhameed, S., Ischuk, A., et al. (2018). Seismotectonics of the Tajik Basin and Surrounding Mountain Ranges, *Tectonics*, *37*(8), 2404–2424. https://doi.org/10.1029/2017TC004812

Kufner, S.-K., Kakar, N., Bezada, M., Bloch, W., Metzger, S., Yuan, X., et al. (2021). The Hindu Kush slab break-off as revealed by deep structure and crustal deformation, *Nature Communication*, 12, 1685. https://doi.org/10.1038/s41467-021-21760-w

Kulikova, G. (2016). Source parameters of the major historical earthquakes in the Tien-Shan region from the late 19th to the early 20th century, *PhD Thesis*, Potsdam University

Lazeckỳ, M., Spaans, K., González, P. J., Maghsoudi, Y., Morishita, Y., Albino, F., et al. (2020). LiCSAR: An automatic InSAR tool for measuring and monitoring tectonic and volcanic activity, *Remote Sensing*, *12*(15). https://doi.org/10.3390/RS12152430

López-Quiroz, P., Doin, M.P., Tupin, F., Briole, P., Nicolas, J.M., (2009). Time series analysis of Mexico City subsidence constrained by radar interferometry, Journal of Applied Geophysics, 69, 1–15. https://doi.org/10.1016/j.jappgeo.2009.02.006

Leith, W., & Simpson, D. W. (1986). Earthquakes related to active salt doming near Kulyab, Tadjikistan, USSR, *Geophysical Research Letters*, *13*(10), 1019–1022. https://doi.org/10.1029/GL013i010p01019

McNab, F., Sloan, R. A., & Walker, R. T. (2019). Simultaneous orthogonal shortening in the Afghan-Tajik Depression, *Geology*, *47*(9), 862–866. https://doi.org/10.1130/G46090.1

Mechie, J., Yuan, X., Schurr, B., Schneider, F., Sippl, C., Ratschbacher, L., et

al. (2012). Crustal and uppermost mantle velocity structure along a profile across the Pamir and southern Tien Shan as derived from project TIPAGE wide-angle seismic data, *Geophysical Journal International*, *188*(2), 385–407. https://doi.org/10.1111/j.1365-246X.2011.05278.x

Metzger, S., Schurr, B., Ratschbacher, L., Sudhaus, H., Kufner, S.-K., Schöne, T., et al. (2017). The 2015 Mw7.2 Sarez strike-slip earthquake in the Pamir interior: Response to the underthrusting of India's western promontory, *Tectonics*, *36*(11), 2407–2421. https://doi.org/10.1002/2017TC004581R

Metzger, S., Ischuk, A., Akhmedov, A., Ilyasova, Z., Moreno, M., Murodkulov, S., & Deng, Z. (2019). Survey mode GPS data in the West Pamir, Tajikistan, Central Asia, 2013–2016, *GFZ Data Services*. https://doi.org/10.5880/GFZ.4.1.2019.007

Metzger, S., Ischuk, A., Deng, Z., Ratschbacher, L., Perry, M., Kufner, S.-K., et al. (2020). Dense GNSS profiles across the northwestern tip of the India-Asia collision zone: Triggered slip and westward flow of the Peter the First Range, Pamir, into the Tajik depression, *Tectonics*, *39*(2), e2019TC005797. https://doi.org/10.1029/2019TC005797

Metzger, S., Kakar, N., Zubovich, A., Borisov, M., Saif, S., Panjsheri, A.H., Rahmani, J.R., Zaryab, M.Y., Rezai, M.T., Deng, Z.,Bendick, R., Kufner, S.-K., Okoev, J. (2021). Survey mode GNSS data, acquired 2014-2019 in the Afghan Hindu Kush and across northern Pamir margin, Central Asia, *GFZ Data Services*, https://doi.org/10.5880/GFZ.4.1.2021.003

Mohadjer, S., Bendick, R., Ischuk, A., Kuzikov, S., Kostuk, A., Saydullaev, U., et al. (2010). Partitioning of India-Eurasia convergence in the Pamir-Hindu Kush from GPS measurements, *Geophysical Research Letters*, *37*(4). https://doi.org/10.1029/2009GL041737

Morishita, Y., Lazecky, M., Wright, T. J., Weiss, J. R., Hooper, A., Elliott, J. R., & Hooper, A. (2020). LiCSBAS: An Open-Source InSAR Time Series Analysis Package Integrated with the LiCSAR Automated Sentinel-1 InSAR Processor, *Remote Sensing*, *12*(3), 5–8. https://doi.org/10.3390/rs12030424

Neelmeijer, J., Schöne, T., Dill, R., Klemann, V., & Motagh, M. (2018). Ground Deformations around the Toktogul Reservoir, Kyrgyzstan, from Envisat ASAR and Sentinel-1 Data—A Case Study about the Impact of Atmospheric Corrections on InSAR Time Series, *Remote Sensing*, *10*(3), 462. https://doi.org/10.3390/rs10030462

Nikolaev, V. G. (2002). Afghan-Tajik depression: Architecture of sedimentary cover and evolution, *Russian Journal of Earth Science*, *4*(6), 399–421.

Ou, Q. (2020). Crustal Deformation and Seismic Hazard of the NE Tibetan Plateau, *PhD Thesis*, University of Oxford.

Perry, M., Kakar, N., Ischuk, A., Metzger, S., Bendick, R., Molnar, P., & Mohadjer, S. (2018). Little Geodetic Evidence for Localized Indian Subduction

in the Pamir-Hindu Kush of Central Asia, *Geophysical Research Letters*, *46*(1), 109–118. https://doi.org/10.1029/2018GL080065

Pozzi, J. P., & Feinberg, H. (1991). Paleomagnetism in the Tajikistan: Continental shortening of European margin in the Pamirs during Indian Eurasian collision, *Earth and Planetary Science Letters*, *103*(1–4), 365–378. https://doi.org/10.1016/0012-821X(91)90173-F

Robinson, A.C., Yin, A., Manning, C.E., Harrison, T.M., Zhang, S.-H., Wang, X.-F. (2004). Tectonic evolution of the northeastern Pamir: Constraints from the northern portion of the Cenozoic Kongur Shan extensional system, western China, *GSA Bulletin*, *116*(7–8), 953–973. https://doi.org/10.1130/B25375.1

Robinson, A.C., Yin, A., Manning, C.E., Harrison, T. M., Zhang, S.-H., Wang, X.-F. (2007) Cenozoic evolution of the eastern Pamir: Implications for strain-accommodation mechanisms at the western end of the Himalayan-Tibetan orogen, *GSA Bulletin*, *119*(7–8), 882–896. https://doi.org/10.1130/B25981.1

Rouyet, L., Lauknes, T. R., Christiansen, H. H., Strand, S. M., & Larsen, Y. (2019). Seasonal dynamics of a permafrost landscape, Adventdalen, Svalbard, investigated by InSAR, *Remote Sensing of Environment*, *231*, 111236. https://doi.org/10.1016/j.rse.2019.111236

Rutte, D., Ratschbacher, L., Schneider, S., Stübner, K., Stearns, M. A., Gulzar, M. A., et al. (2017). Building the Pamir-Tibetan Plateau – Crustal stacking, extensional collapse, and lateral extrusion in the Central Pamir: 1. Geometry and kinematics, *Tectonics*, *36*(3), 342–384. https://doi.org/10.1002/2016TC004293

Sangha, S., Peltzer, G., Zhang, A., Meng, L., Lian, C., Lundgren, P., et al. (2017). Fault geometry of 2015, Mw7.2 Murghab, Tajikistan earthquake controls rupture propagation: Insights from InSAR and seismological data, *Earth and Planetary Science Letters*, *462*, 132–141. https://doi.org/10.1016/j.epsl.2017.01.018

Savage, J. C., & Burford, R. O. (1973). Geodetic Determination of Relative Plate Motion in Central California, *Journal of Geophysical Research*, *78*(5), 832–845. https://doi.org/10.1029/JB078i005p00832

Schneider, F. M., Yuan, X., Schurr, B., Mechie, J., Sippl, C., Kufner, S.-K., et al. (2019). The Crust in the Pamir: Insights From Receiver Functions Journal of Geophysical Research: Solid Earth, *Journal of Geophysical Research: Solid Earth*, *124*, 9313– 9331. https://doi.org/10.1029/2019JB017765

Schurr, B., Ratschbacher, L., Sippl, C., Gloaguen, R., Yuan, X., & Mechie, J. (2014). Seismotectonics of the Pamir, *Tectonics*, *33*(80), 1501–1518. https://doi.org/10.1002/2014TC003576

Schwab, M., Ratschbacher, L., Siebel, W., McWilliams, M., Minaev, V., Lutkov, V., et al. (2004), Assembly of the Pamirs: Age and origin of magmatic belts

from the southern Tien Shan to the southern Pamirs and their relation to Tibet, *Tectonics*, *23*, TC4002. https://doi.org/10.1029/2003TC001583

Sippl, C., Schurr, B., Yuan, X., Mechie, J., Schneider, F. M., Gadoev, M., et al. (2013). Geometry of the Pamir-Hindu Kush intermediate-depth earthquake zone from local seismic data, *Journal of Geophysical Research: Solid Earth*, *118*(4), 1438–1457. https://doi.org/10.1002/jgrb.50128

Sippl, C., Ratschbacher, L., Schurr, B., Krumbiegel, C., Rui, H., Pingren, L., & Abdybachaev, U. (2014). The 2008 Nura earthquake sequence at the Pamir-Tian Shan collision zone, southern Kyrgyzstan, *Tectonics*, *33*(12), 2382–2399. https://doi.org/10.1002/2014TC003705

Sperner, B. & Ratschbacher, L. (1994). A Turbo Pascal program package for graphical presentation and stress analysis of calcite deformation, *Zeitschriften der Deutschen Geologischen Gesellschaft*, *145*, 414–423.

Storchak, D. A., Di Giacomo, D., Bondár, I., Engdahl, E. R., Harris, J., Lee, W. H. K., et al. (2013). Public release of the ISC-GEM global instrumental earthquake catalogue (1900–2009), *Seismological Research Letters*, *84*, 810–815. https://doi.org/10.1785/0220130034

Stübner, K., Ratschbacher, L., Rutte, D., Stanek, K., Minaev, V., Wiesinger, R., et al. (2013). The giant Shakhdara migmatitic gneiss dome, Pamir, India-Asia collision zone, 1: Geometry and kinematics, *Tectonics*, *32*, 948–979. https://doi.org/10.1002/tect.20057

Stübner, K., Grin, E., Hidy, A.J., Schaller, M., Gold, R.D., Ratschbacher, L., Ehlers, T. (2017). Middle and Late Pleistocene glaciations in the southwestern Pamir and their effects on topography, *Earth and Planetary Science Letters*, *466*, 181–194. https://doi.org/10.1016/j.epsl.2017.03.012

Teshebaeva, K., Sudhaus, H., Echtler, H., Schurr, B., & Roessner, S. (2014). Strain partitioning at the eastern Pamir-Alai revealed through SAR data analysis of the 2008 Nura earthquake, *Geophysical Journal International*, *198*(2), 760–774. https://doi.org/10.1093/gji/ggu158

Thomas, J.-C., Chauvin, A., Gapais, D., Bazhenov, M. L., Perroud, H., Cobbold, P. R., and Burtman, V. S. (1994). Paleomagnetic evidence for Cenozoic block rotations in the Tadjik depression (Central Asia), *Journal of Geophysical Research*, *99*(B8), 15141−15160. https://doi.org/10.1029/94JB00901

Vajedian, S., Motagh, M., Wetzel, H.-U., Teshebaeva, K. (2017). Coupling of Sentinel-1, Sentinel-2 and ALOS-2 to assess coseismic deformation and earthquake-induced landslides following the 26 June, 2016 earthquake in Kyrgyzstan, *Geophysical Research Abstracts*, *19*, EGU2017-18464-1.

Wang, S., Xu, C., Wen, Y., Yin, Z., Jiang, G., Fang, L. (2017). Slip Model for the 25 November 2016 Mw6.6 Aketao Earthquake, Western China, Revealed by Sentinel-1 and ALOS-2 Observations, *Remote Sensing*, *9*, 325, https://doi.org/10.3390/rs9040325

Wegmüller, U., & Werner, C. (1997). Gamma SAR processor and interferometry software. *ERS Symposium on Space at the Service of Our Environment*, Florence, Italy.

Wegmüller, U., Werner, C., Strozzi, T., Wiesmann, A., Frey, O., & Santoro, M. (2016). Sentinel-1 Support in the GAMMA Software, *Procedia Computer Science*, *100*, 1305–1312. https://doi.org/https://doi.org/10.1016/j.procs.2016.09.246

Weiss, J. R., Walters, R. J., Morishita, Y., Wright, T. J., Lazecky, M., Wang, H., et al. (2020). High-Resolution Surface Velocities and Strain for Anatolia From Sentinel-1 InSAR and GNSS Data, *Geophysical Research Letters*, *47*(17). https://doi.org/10.1029/2020GL087376

Wessel, P., Smith, W. H. F., Scharroo, R., Luis, J. F., & Wobbe, F. (2013). Generic Mapping Tools: Improved version released, *EOS Transactions AGU*, *94*, 409–410. https://doi.org/10.1002/2013EO450001

Wilkinson, R., Daout, S., Parsons, B., & Walker, R. T. (2020). A time-series InSAR study of faulting and folding in the Tajik Basin, *American Geophysical Union*, Fall Meeting 2020, #G021-0007.

Wright, T. J., Parsons, B. E., & Lu, Z. (2004). Toward mapping surface deformation in three dimensions using InSAR, *Geophysical Research Letters*, *31*, L01607. https://doi.org/https://doi.org/10.1029/2003GL018827

Yu, C., Li, Z., Penna, N. T., & Crippa, P. (2018). Generic Atmospheric Correction Model for Interferometric Synthetic Aperture Radar Observations, *Journal of Geophysical Research: Solid Earth*, *123*(10), 9202–9222. https://doi.org/10.1029/2017JB015305

Zhan, Z., & Kanamori, H. (2016). Recurring large deep earthquakes in Hindu Kush driven by a sinking slab, *Geophysical Research Letters*, *43*(14), 7433–7441. https://doi.org/10.1002/2016GL069603

Zubovich, A. V., Wang, X. Q., Scherba, Y. G., Schelochkov, G. G., Reilinger, R., Reigber, C., et al. (2010). GPS velocity field of the Tien Shan and surrounding regions, *Tectonics*, *29*(TC6014), 1–23. https://doi.org/10.1029/2010TC002772

Zubovich, A. V., Schöne, T., Metzger, S., Mosienko, O., Mukhamediev, S., Sharshebaev, A., & Zech, C. (2016). Tectonic interaction between the Pamir and Tien Shan observed by GPS, *Tectonics*, *35*(2), 283–292. https://doi.org/10.1002/2015TC004055

Supporting Information for "Tajik Depression and Greater Pamir Neotectonics from InSAR Rate Maps"

Sabrina Metzger[1], Łukasz Gągała[2,3], Lothar Ratschbacher[2], Milan Lazecký[4], Yasser Maghsoudi[4], Bernd Schurr[1]

[1]Lithosphere Dynamics, Helmholtz Center, Research Center for Geosciences, Potsdam, Germany

[2]Geologie, Technische Universität Bergakademie Freiberg, Freiberg, Germany

[3]Now at Hellenic Petroleum, Marousi, Greece

[4]COMET, School of Earth and Environment, University of Leeds, United Kingdom

Contents of this file

1. Supplementary text to Section 3 of the main text: How the individual rate maps in LOS were tied to the GNSS reference frame and decomposed into East and Up rates.

2. Tables S1 to S2 as mentioned in main text

3. Figures S1 to S9 as mentioned in main text

Additional Supporting Information (Files uploaded separately)

1. **RateMaps.zip** – LiCSBAS InSAR rate maps and auxiliary information in geotiff-format: linear rates, uncertainties and LOS information of individual frames (labeled by frame number); concatenated and decomposed East and Up rates (in stable Eurasian reference frame, ITRF2014, Altamimi et al., 2017) and corresponding uncertainties.

Corresponding author: Sabrina Metzger, metzger@gfz-potsdam.de

1. From LOS rates to East/Vertical rates in a GNSS-fixed reference frame

We corrected each rate map with a linear ramp to optimize the fit to the horizontal GNSS rates and the frame overlap along-track. These two conditions can be formulated as a $M \times N$ design matrix G, which, if multiplied with N ramp parameters $m = [m_1, ..., m_N]^T$, match M observations $d = [d_1, ..., d_M]^T$. If uncertainties are included as data weights W this results in $Wd = WGm$. If this problem is linear and over-determined it can be solved for the best-fit ramp parameters,

$$m = (G^T W G)^{-1} G^T W d.$$

Both conditions are met for any given three successive InSAR frames $I1$, $I2$ and $I3$ and the co-located GNSS rates $G1$, $G2$ and $G3$ (collapsed into line-of-sight) with

$$\begin{bmatrix} I1-I2 \\ I2-I3 \\ I1-G1 \\ I2-G2 \\ I3-G3 \end{bmatrix} = \begin{bmatrix} x & y & 1 & -x & -y & -1 & 0 & 0 & 0 \\ 0 & 0 & 0 & x & y & 1 & -x & -y & -1 \\ x & y & 1 & 0 & 0 & 0 & 0 & 0 & 0 \\ 0 & 0 & 0 & x & y & 1 & 0 & 0 & 0 \\ 0 & 0 & 0 & 0 & 0 & 0 & x & y & 1 \end{bmatrix} \cdot \begin{bmatrix} a_1 \\ b_1 \\ c_1 \\ ... \\ a_3 \\ b_3 \\ c_3 \end{bmatrix}$$

where x,y being the column and row index numbers of the merged pixel index frame and a,b,c the linear ramp parameters to be inverted for. Following Ou (2020) we weighted the InSAR rates overlapping along-track with the inverted sum of the standard deviation of the detrended overlap area, for example $(\sigma(I1) + \sigma(I2))^{-1}$. For the lower part of the equation, where InSAR rates are fitted to GNSS rates, we apply the combined weights

$$\sqrt{\frac{m}{n}}(\sigma(I1) + \sigma(G1))^{-1},$$

where the InSAR uncertainties are given by the standard deviation of all pixels within the search radius of a GNSS data point, the GNSS uncertainties are collapsed into line-

of-sight (LOS) and the whole term is scaled by the squar-root of the ratio of number of InSAR data points m and GNSS data points n.

In a second step, we decomposed ascending and descending LOS rates of each pixel, where both were available, into East and Vertical rates following Ou (2020). The line-of-sight velocity V_{LOS} is defined by the heading angle ϕ, measured positive clockwise from north, and the incidence angle θ, measured from the vertical down direction,

$$V_{LOS} = -V_E \cos(\phi) \sin(\theta) + V_N \sin(\phi) \sin(\theta) + V_U \cos(\theta), \tag{1}$$

where each term defines the contributeion of the east, north and vertical component, respectively. Given the near-polar orbits and relatively steep look angle, this means that the individual contributions of each direction are about 40, 10 and 50 per cent, hence, InSAR data is least sensitive to NS-motion (Figure S4).

Equation (1) can then be rearranged to a linear problem that can be inverted to obtain East (E) and a sub-Vertical (UN) direction:

$$V_{LOS} = \begin{bmatrix} -\cos(\phi)\sin(\theta) & \sqrt{1 - \sin^2(\theta)\cos^2(\phi)} \end{bmatrix} \cdot \begin{bmatrix} V_E \\ V_{UN} \end{bmatrix}$$

Each InSAR rate pixel is weighted by its standard deviation. The associated uncertainties $\sigma(V_E)$ and $\sigma(V_{UN})$ are calculated by the design matrix G and the squared uncertainty matrix Σ via $cov(p) = [G^T cov(d)^{-1} G]^{-1}$, where the diagonal terms of $cov(p)$ are the variances, respectively squared uncertainties, of V_E and V_{UN}.

Using independent constraints from GNSS data we then further decompose V_{UN}. The tectonically dominant northward motion of the region is most difficult to resolve with InSAR but is well constrained by GNSS data. Thus, we fixed the North component

using interpolated GNSS data (Figure 1c) and solved for the vertical component. We fit a surface to the GNSS measurements and also the corresponding uncertainties using natural neighbor interpolation and subtracted it from V_{UN},

$$V_U = \frac{V_{UN} \cdot \sqrt{1 - \sin^2(\theta)\cos^2(\phi)}}{\cos(\theta)} - V_N \frac{\sin(\phi)\sin(\theta)}{\cos(\theta)}$$

The corresponding uncertainties were calculated by replacing the rates with the uncertainties in the above formula.

Table S1. Interferometric data base used for SBAS inversion, after quality control, with track and frame numbers, start and end dates (in YYYYMMDD). ΔT is the time period covered by our InSAR networks in years and "ifgs" the number of interferograms used in the inversion. "mask" denotes the percentage of masked pixels per frame. The inversion was an unweighted NSBAS least-square inversion with a gamma value of 0.0001. The coordinates indicate the rate reference point.

Track	Frame	Start date	End date	ΔT [yr]	#sc	#ifg	mask [%]	Lat.[°]	Lon.[°]
005D	050	20170312	20200507	2.98	76	196	32	73.1922	40.0142
005D	051	20180506	20200706	2.00	46	146	52	72.6672	38.3310
005D	053	20170628	20200706	2.94	54	94	46	71.4376	36.1750
071A	052	20150806	20200312	5.02	94	313	11	69.0243	36.9975
071A	054	20141010	20200312	6.00	112	354	42	69.8484	35.6594
078D	050	20171230	20200804	2.93	74	234	46	70.3022	39.8281
078D	052	20170317	20191126	2.02	64	160	45	70.2885	37.1488
078D	054	20170703	20200430	3.07	64	142	50	70.2197	36.3637
100A	050	20160814	20200618	4.01	97	335	44	72.7361	39.2707
100A	052	20170505	20200618	3.03	52	111	56	73.5527	37.5625
151D	052	20171211	20200517	3.01	70	268	9	68.2496	37.7773
173A	051	20160714	20200717	4.01	67	144	68	71.0955	38.7018
173A	053	20151129	20200518	4.97	61	126	58	71.1958	36.8771

Table S2. Individual LiCSBAS processing and filtering parameters sorted by frame and track number. Generally used masking thresholds were average coherence of 0.05, 100 mm/yr standard rate deviation, 10 allowed data gaps, 5 mm spatio-temporal consistency – all other thresholds are stated below. To estimate and suppress the linear height-dependence all pixels above 200 m a.s.l. were included. Each pixel has a spatial extent of 444 m along flight-track and 340-360 m across flight-track.

Track	Frame	T_{max} [a]	# i_no_loop	# loop_err	rms [mm/yr]	filt [km]	filt [d]
005D	050	1.0	50	5	2	2	46
005D	051	1.0	50	**7**	**3**	2	52
005D	053	**0.0**	50	5	2	2	62
071A	052	1.0	50	5	2	2	54
071A	054	1.0	**15**	5	2	**5**	53
078D	050	**0.9**	50	5	2	2	38
078D	052	1.0	50	5	2	2	46
078D	054	1.0	50	5	2	2	49
100A	050	1.0	**10**	5	2	2	43
100A	052	**2.0**	50	5	2	2	67
151D	052	1.0	50	5	2	2	38
173A	051	1.0	50	**0**	2	2	66
173A	053	1.0	50	5	2	2	81

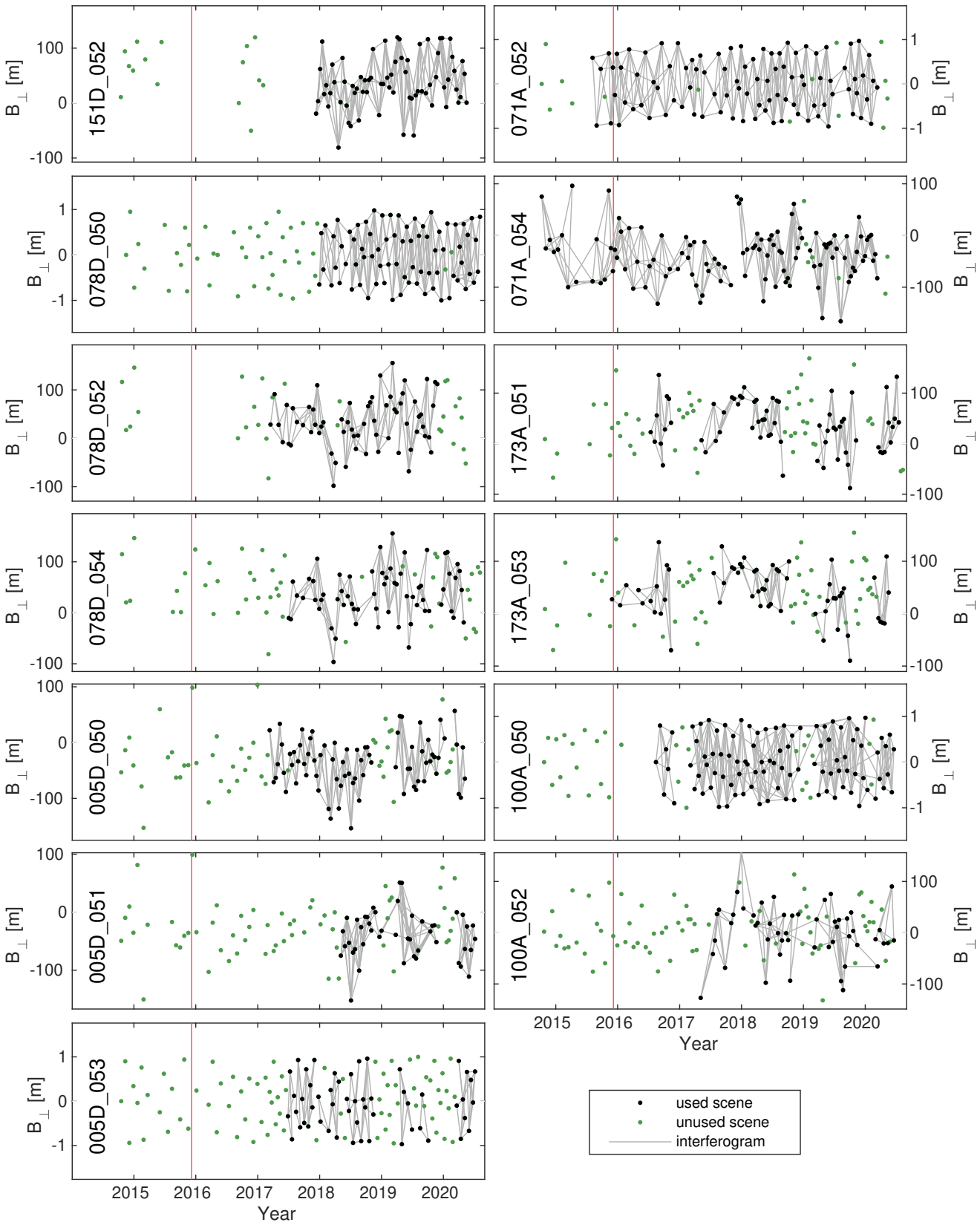

Figure S1. Temporal baselines and interferometric networks sorted by frame number (see Figure 1b for frame locations). Gray lines mark interferograms used in the LiCSBAS time-series analysis, green dots mark unused SAR scenes, red line marks the time of M_W7.2 Pamir earthquake. If no information were available, the orbital baselines are randomized and normalized between ±1.

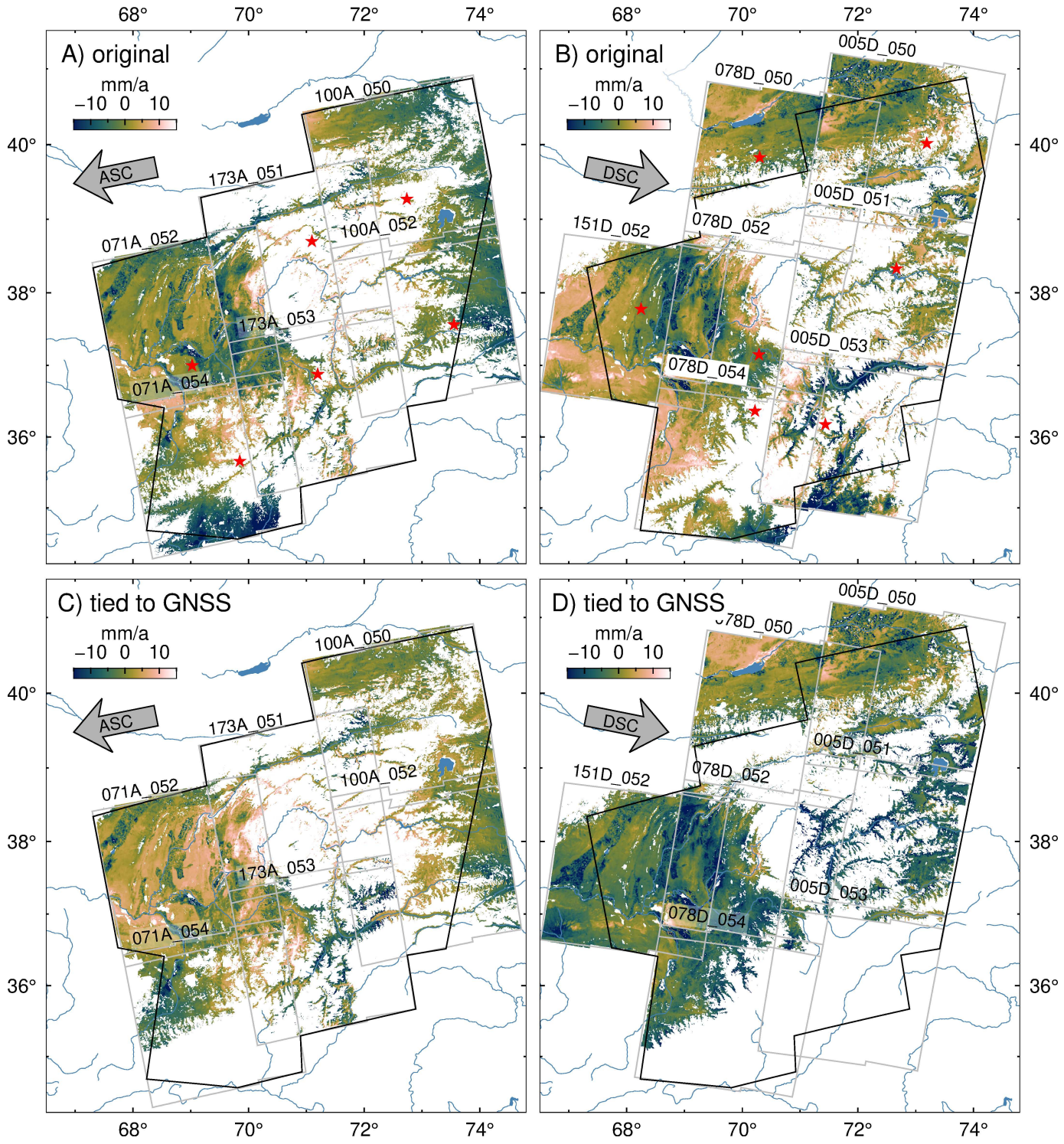

Figure S2. Rate maps resulting from LiCSBAS time-series analysis of A) ascending and B) descending radar frames, relative to the most stable reference point within each frame (red stars) and C) and D) after tying the rates to a Eurasia-fixed GNSS reference frame. Color scales are saturated.

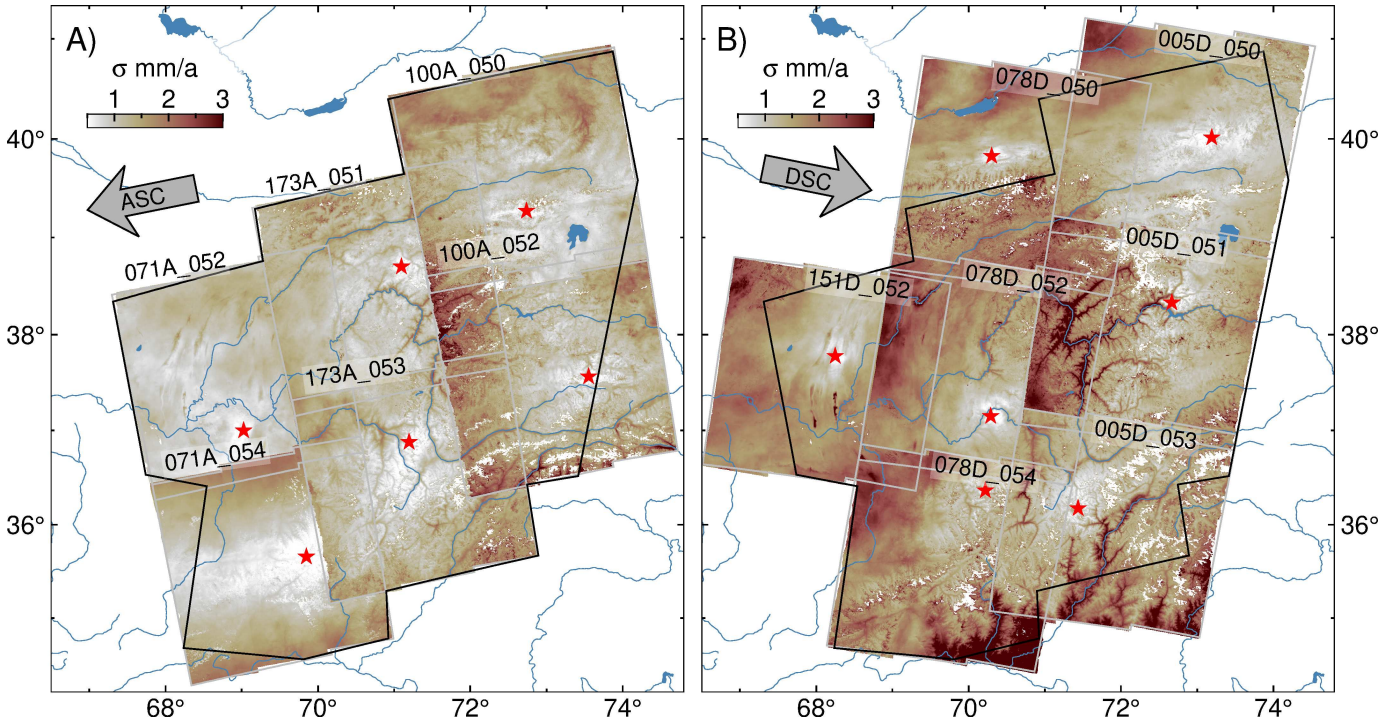

Figure S3. Standard deviations resulting from LiCSBAS time-series analysis of A) ascending and B) descending rate maps. Uncertainties scale with distance to the reference point. Large uncertainties are mostly caused by poorly unwrapped interferograms and/or strongly varying tropospheric conditions.

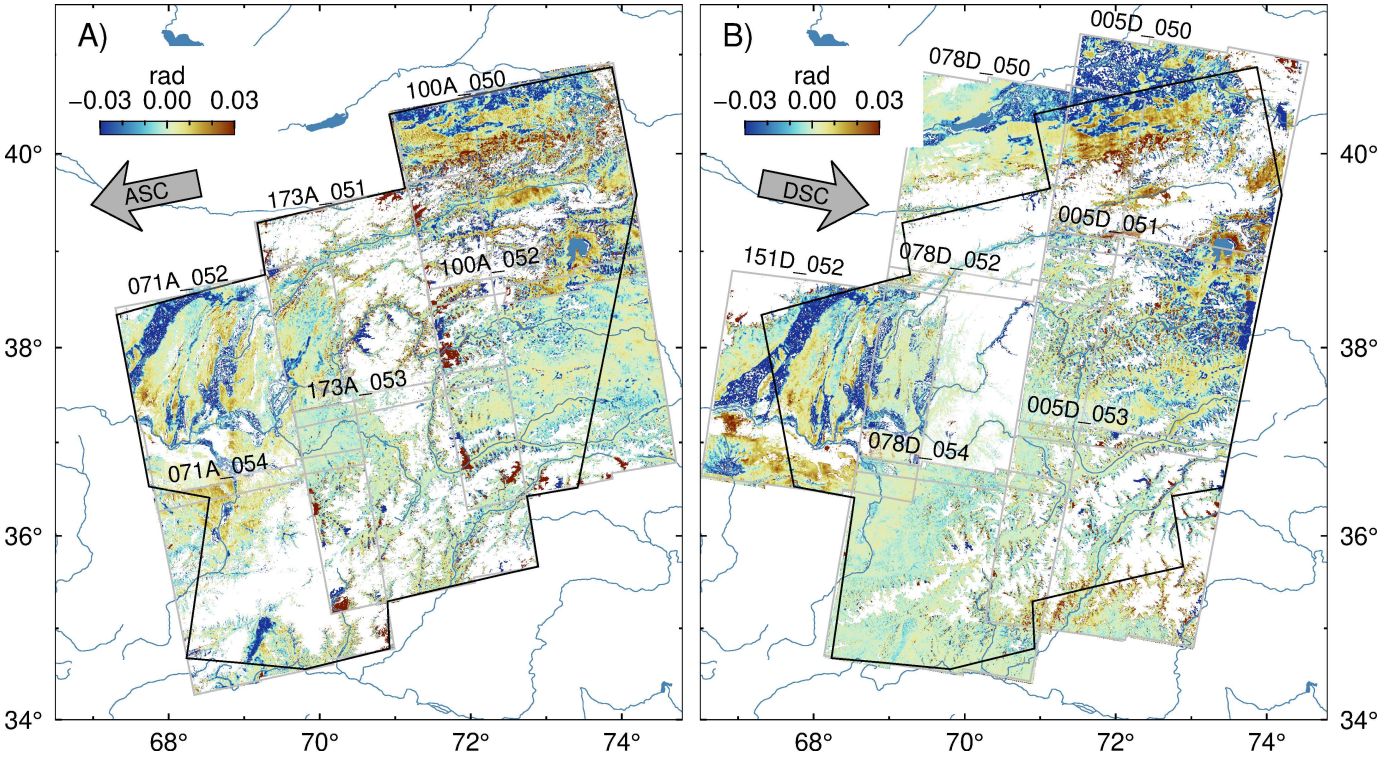

Figure S4. Systematic rate bias in A) ascending and B) descending frames, that is the average of 70-80 interferometric phase closure loops ($\phi_{13} - \phi_{12} - \phi_{23}$) of 2017-2020 interferograms.

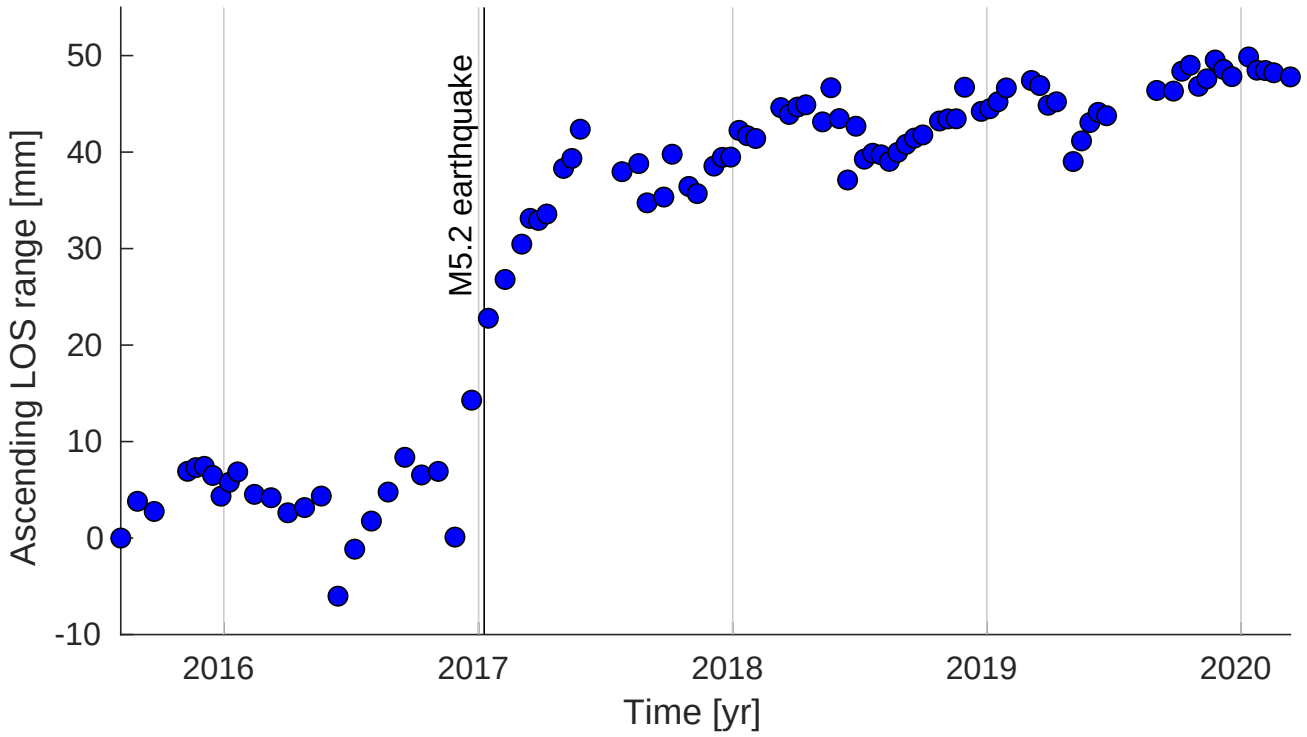

Figure S5. Time-series in ascending line-of-sight of a pixel at the center of marker "g" in Figure 3, showing a combination of uplift and westward motion following the M_W5.2 earthquakes on January 9, 2017. Background signal is caused by seasonal surface changes and tectonic west and/or upward motion.

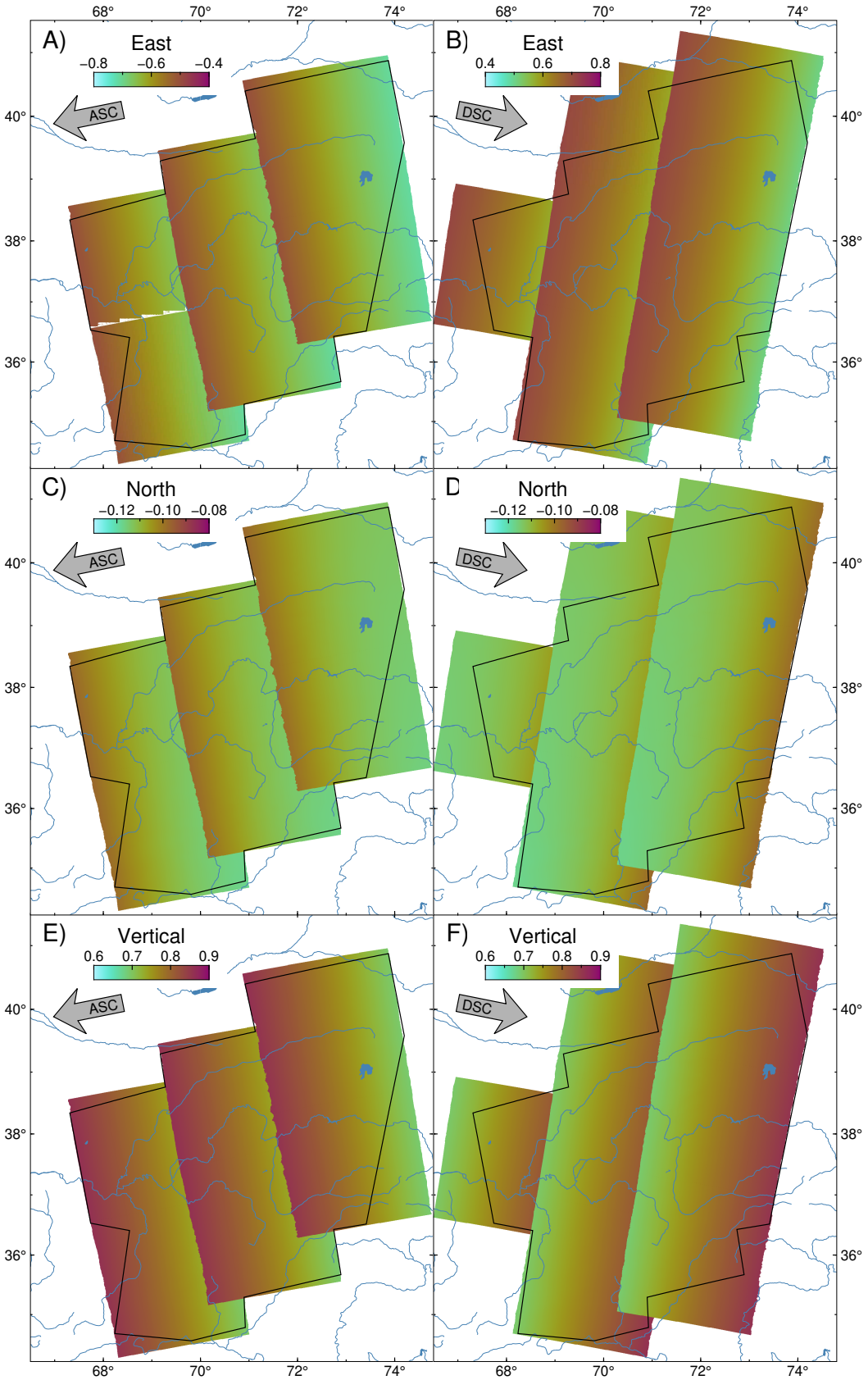

Figure S6. Unit values of the ascending (ASC, from left to right, track 71, 173 and 100) and descending (DSC, track 151, 078 and 005) line-of-sight vector for A), B) east, C), D) north and E), F) vertical direction. Note the different color scales.

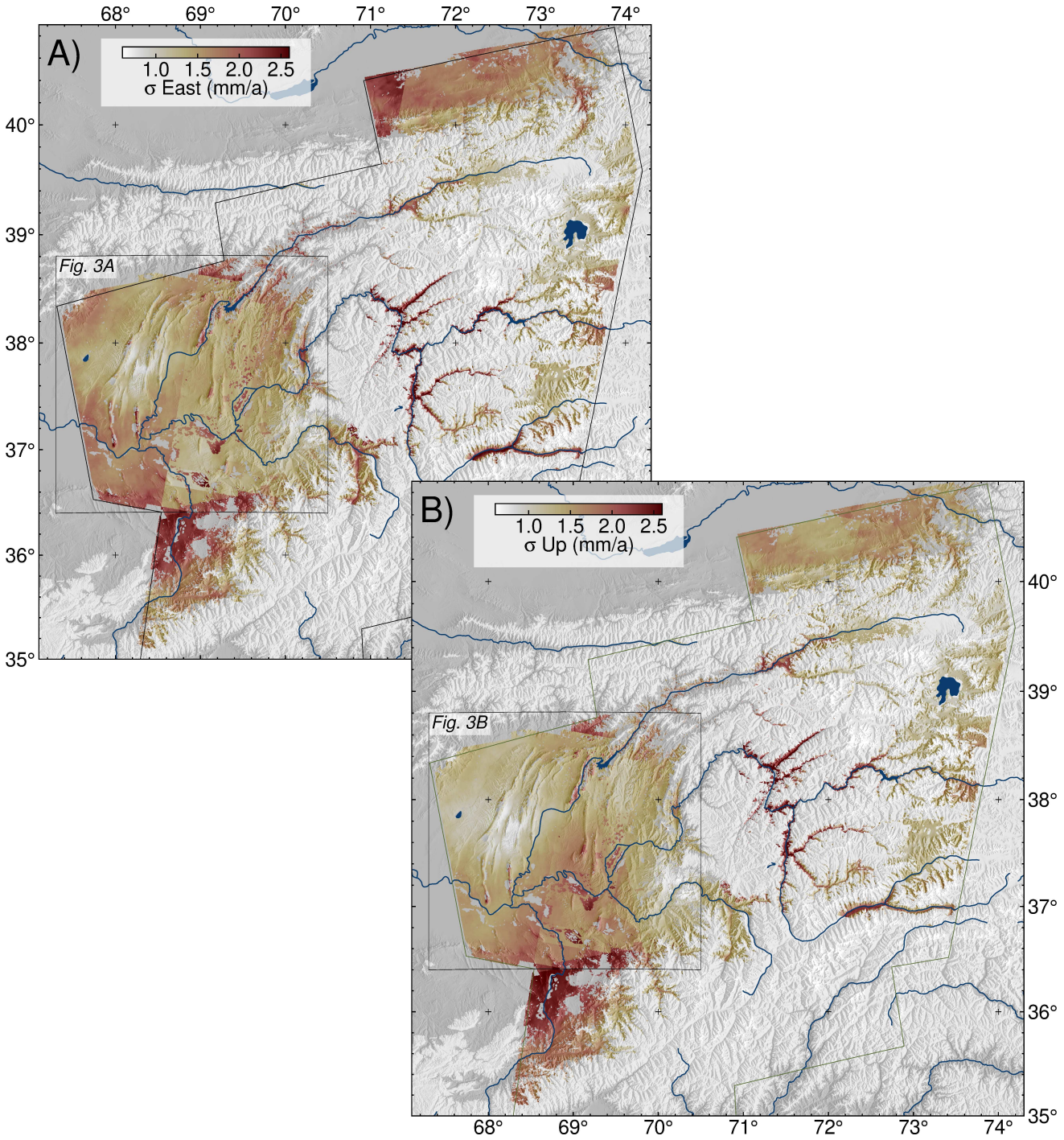

Figure S7. Rate standard deviation of A) east and B) vertical rates after decomposition and inclusion of GNSS rate errors.

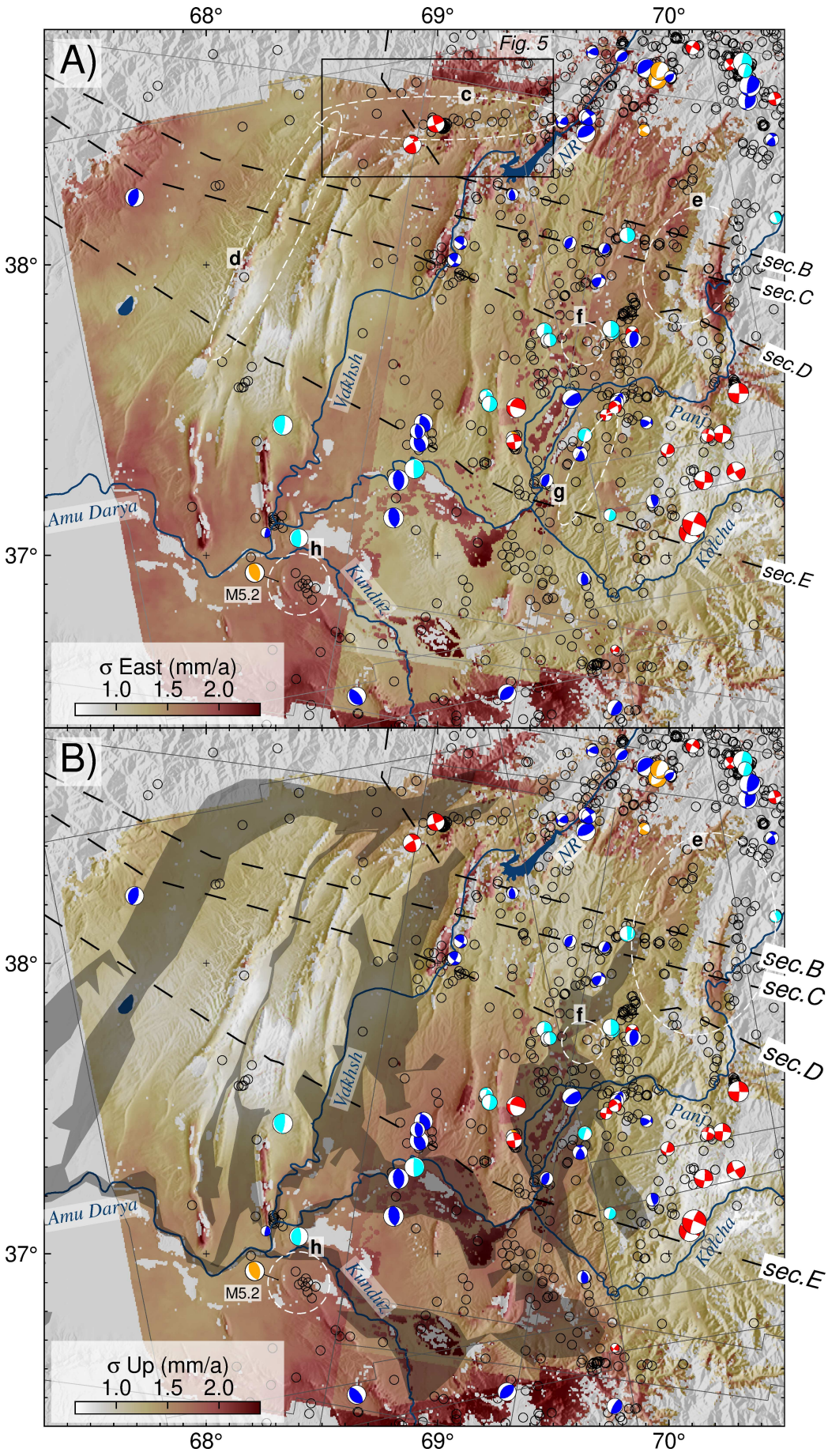

Figure S8. Detail view of Figure S7. See Figure 3 for other features.

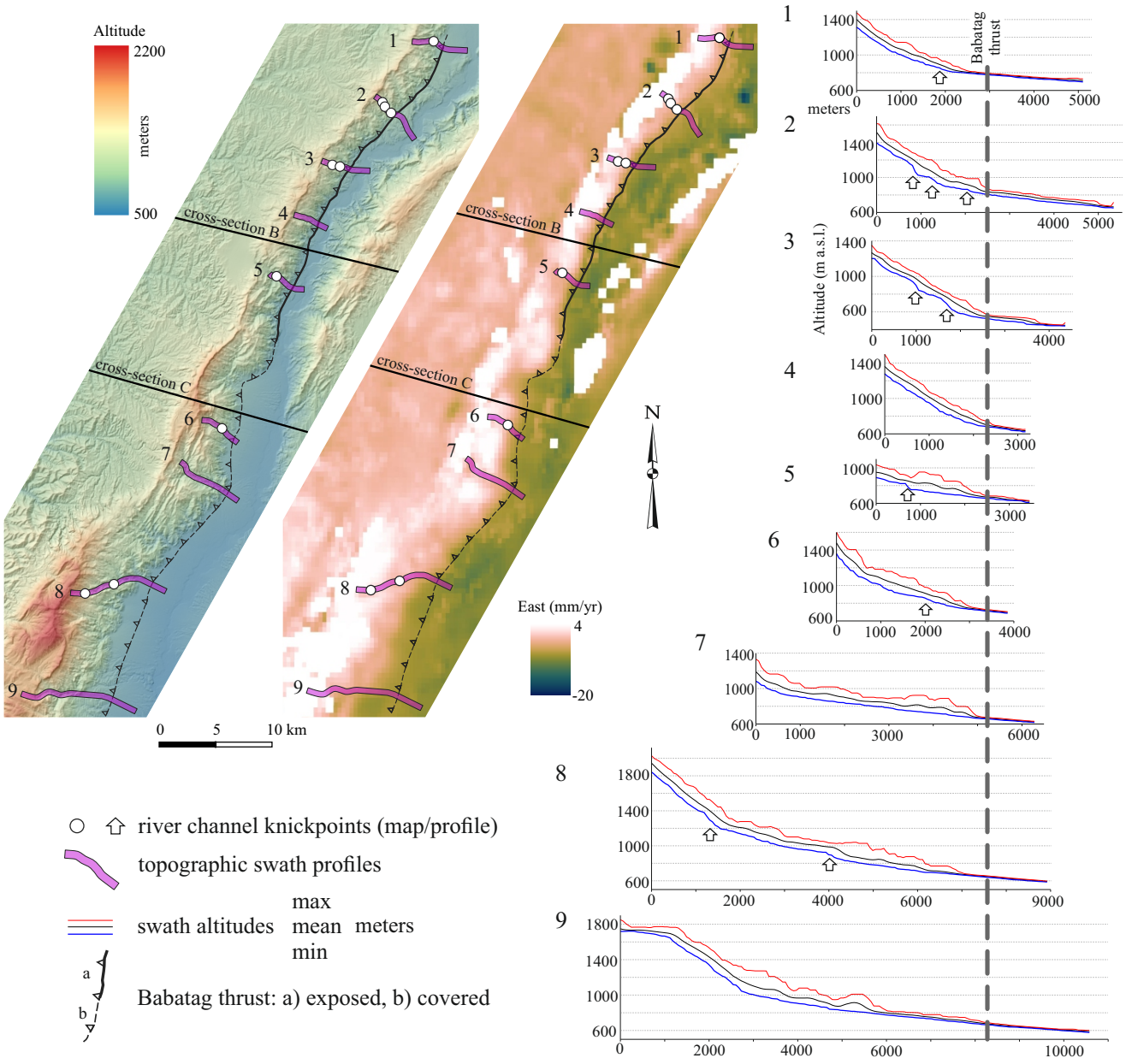

Figure S9. Recent activity of the Babatag thrust indicated by geomorphology. Maps plot topography, east rates, and local geology. The series of 500-m-wide swath profiles along selected stream trunks at the east-facing slopes of the Babatag anticline display knickpoints, likely indicating topographic perturbations due to slip along the Babatag thrust; due to the lack of detailed geological mapping, we cannot exclude that some of the knickpoints mark lithological changes.

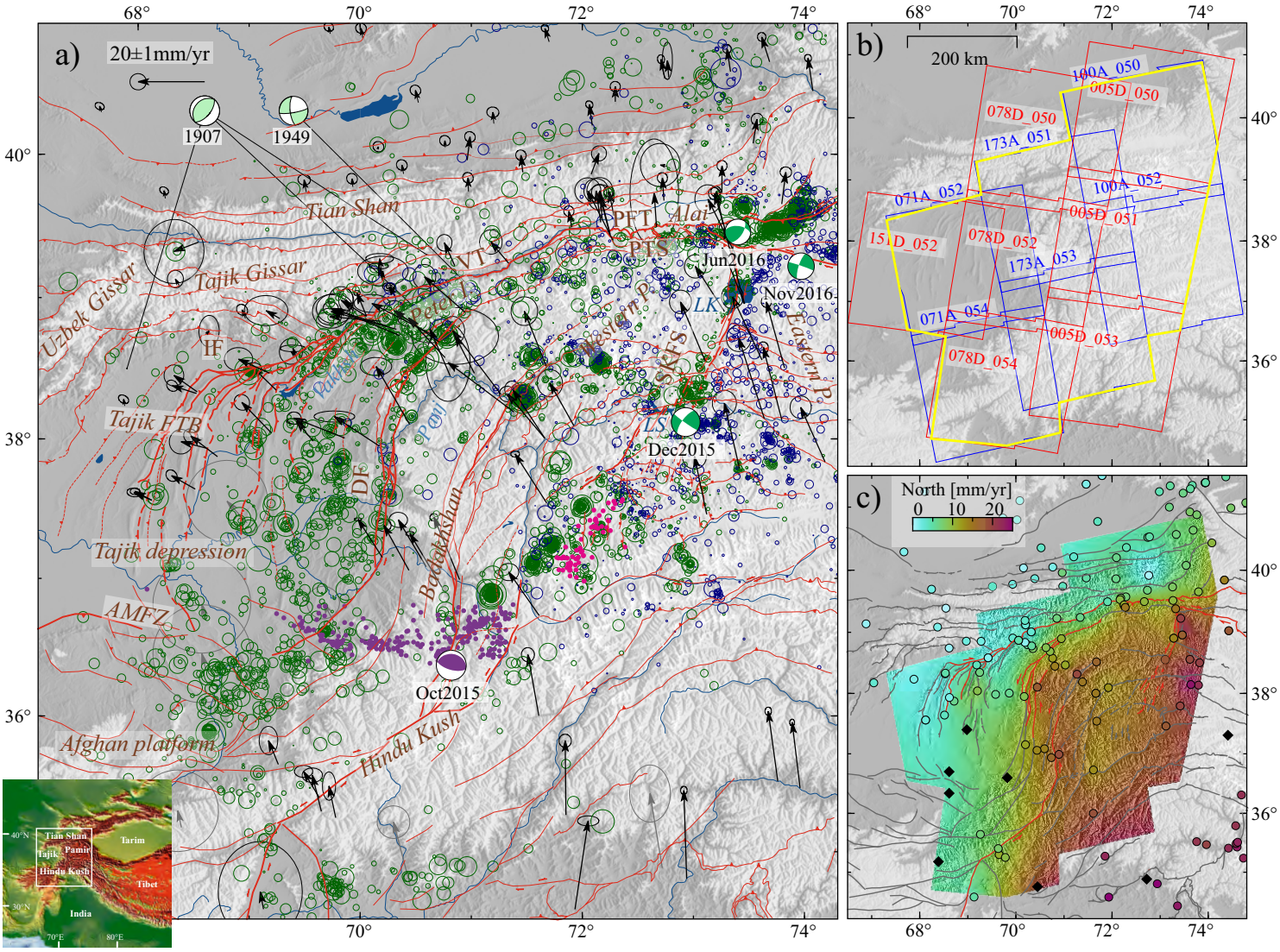

Figure 1. Tectonic setting of the greater Pamir, GNSS displacement rates, and InSAR data coverage. a) Eurasian-fixed GNSS rates (Ischuk et al., 2013; Metzger et al., 2019, 2020, 2021; Perry et al., 2018; Zubovich et al., 2010, 2016), major Cenozoic faults (completed from Abdulhameed et al., 2020; Käßner et al., 2016, Schurr et al., 2014), background seismicity (green circles, scaled by size of Kufner et al., 2018, 2021 in green and Bloch et al., 2019 in blue) and river systems. Inset locates the study area at the northwestern end of the India-Asia collision zone. Historical M7 earthquakes, and M6-7 earthquakes—potentially influencing our analysis—are plotted as bright green, respectively, dark green/violet focal mechanisms (references in text and GEOFON data center). Intermediate-depth earthquakes (>200 km depth) highlight the mantle portion of the Pamir slab (pink dots) and the Hindu Kush slab (purple dots; Kufner et al., 2021). AMFZ: Alburz-Marmul fault zone, DF: Darvaz fault zone, FTB: fold-thrust belt, IF: Ilyak fault, P.: Pamir, PFT: Pamir Frontal Thrust, PTS: Pamir Thrust System, SKFS: Sarez-Karakul fault system, VT: Vakhsh thrust; LK: Lake Karakul, LS: Lake Sarez. b) Interferometric database containing six frames acquired in ascending LOS (blue) and seven frames in descending LOS (red) view direction. Yellow polygon marks region where the LOS rates were decomposed into east and vertical components using interpolated North rates, shown in c), based on available GNSS rates (circles, see references in text), including eight artificial (interpolated) rates to stabilize the sparsely-occupied regions (black squares).

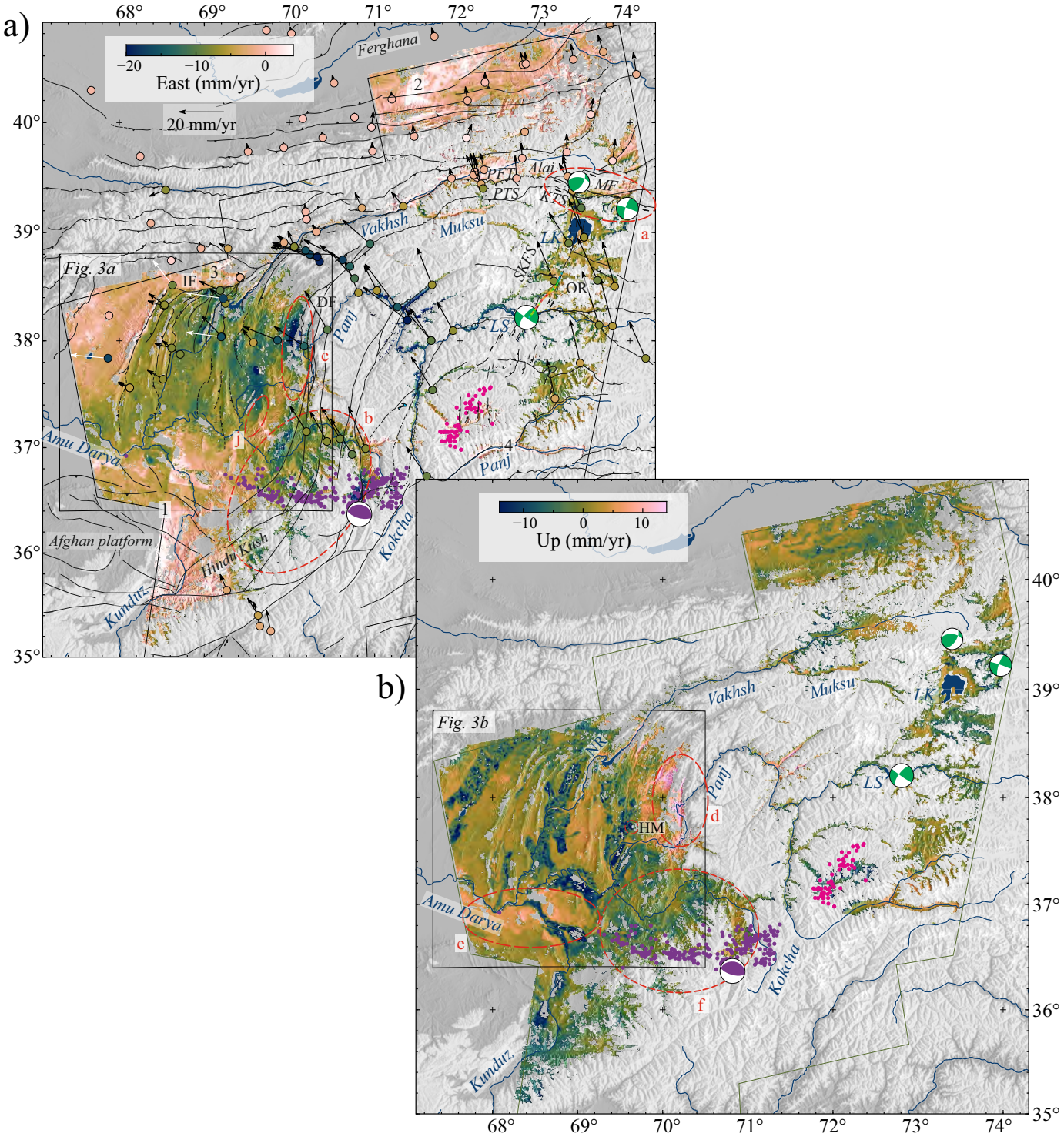

Figure 2. a) East and b) vertical InSAR displacement rates, plotted on topography and simplified fault map. East rates are compared to GNSS rates (vectors and color-coded circles); color scales are saturated. White arrows mark GNSS rates in the Tajik depression that were excluded as outliers. Focal mechanisms indicate crustal (dark green, M>6) and slab break-off (at 200 km, purple, M_w7.5) earthquake(s) that occurred during the data acquisition period (references in text). Purple and pink dots outline the intermediate-depth earthquakes (>200 km depth) of the Hindu Kush and Pamir slabs, respectively. The color-coded line in a) represents the modeled slip of the 2015 Sarez earthquake in the upper 2.5 km of the crust (slip range 0.5-3.0 m; from Metzger et al., 2017). Markers "1" to "4" locate artefacts, i.e., long-wavelength extrema in the corners and edges of frames. Markers "a" to "j" locate features that we discuss in detail in the text. DF: Darvaz fault zone, IF: Ilyak fault, KTS: Kyzilart transfer zone, MF: Muji fault, OF: Officers Range, PFT: Pamir Frontal Thrust, PTS: Pamir Thrust System, SKFS: Sarez-Karakul fault system; HM: Hoja Mumin salt fountain, LK: Lake Karakul, LS: Lake Sarez, NR: Nurak reservoir.

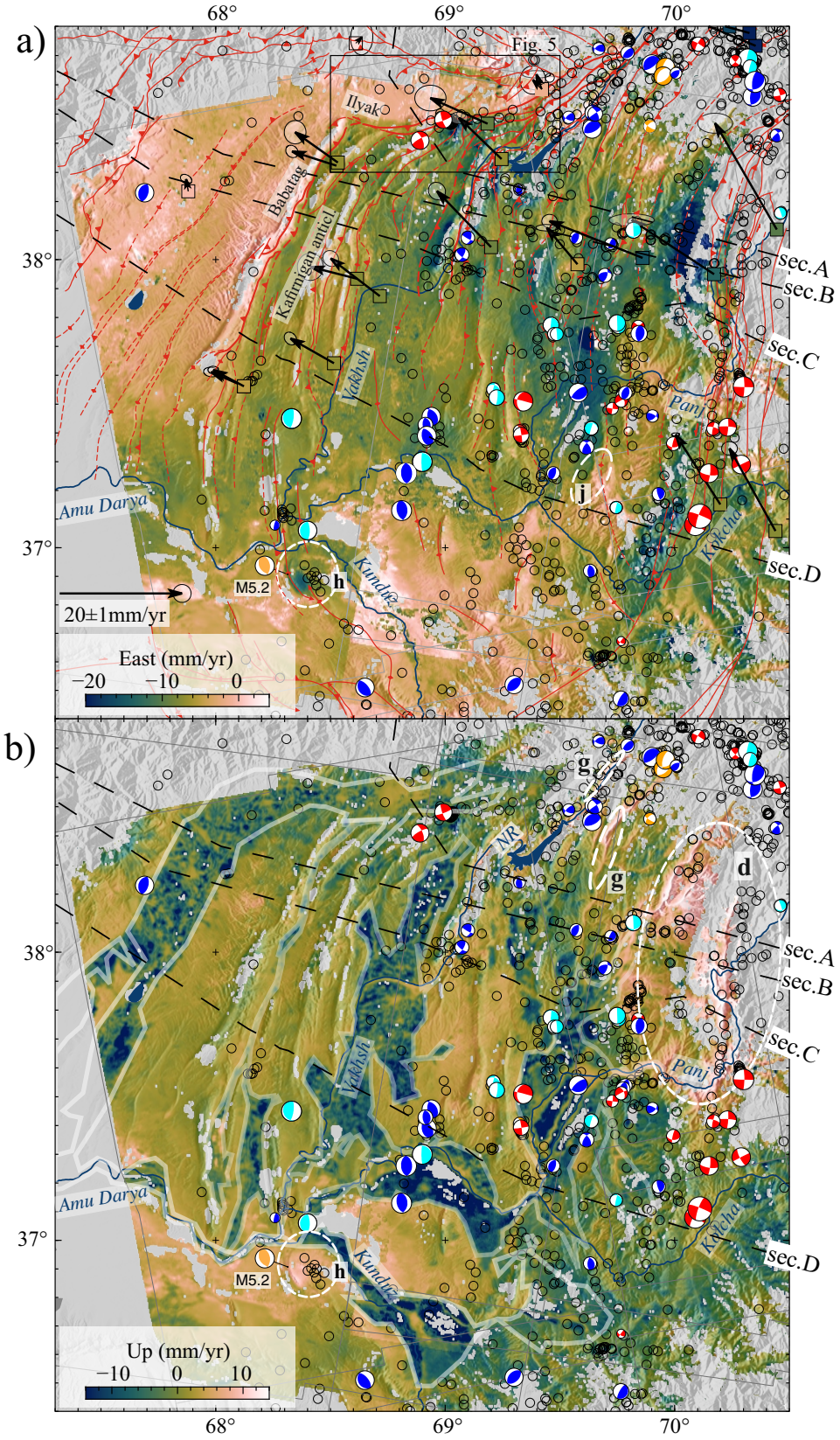

Figure 3. InSAR rates in the Tajik depression, compared to background seismicity (circles and focal mechanisms; Ekström et al., 2012; Kufner et al., 2018, 2021), and plotted on detailed fault-fold map. Thin gray lines mark extent of interferometric frames. a) East rates are compared to GNSS rates (color-coded squares and arrows). b) Vertical rates; white frames mark agricultural land use, based on MDA US BaseVue 2013 Landsat 8 data. Cross sections A to D are shown in Figures 4a and 4b. Markers "d", "h", and "j" locate features that we discuss in detail in the text. NR: Nurak reservoir.

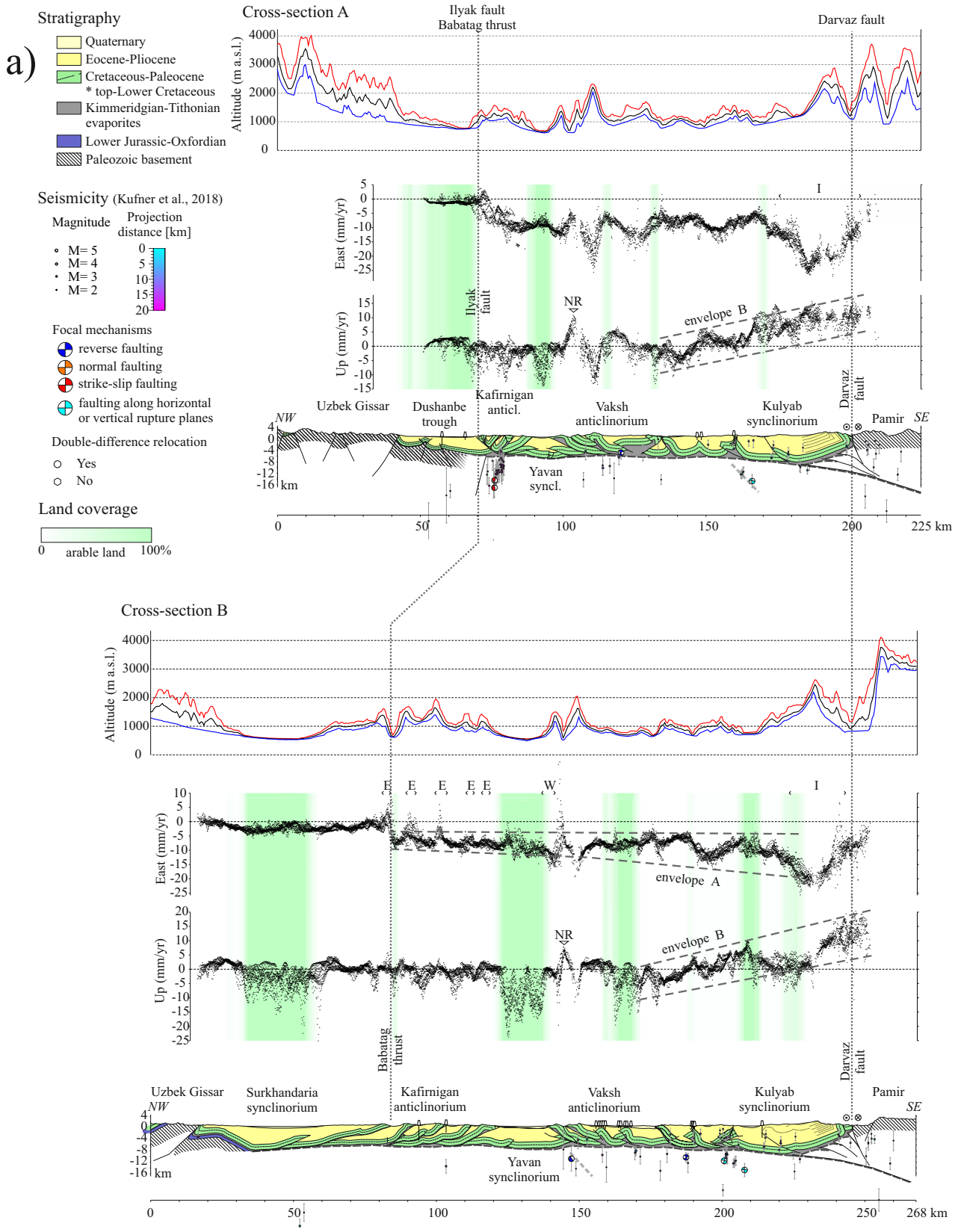

Figure 4. Topographic profiles (max., mean, min. values within 5-km swath), InSAR horizontal and vertical displacement rates, and background seismicity (Kufner et al., 2018) projected onto geological cross-sections A to D through the Tajik depression (Gągała et al., 2020; see Figure 3 for location) with the main structural features named (compare Figures 1 to 3). Markers E, H, I, NR, and W, and envelopes A and B locate features that we discuss in detail in the text.

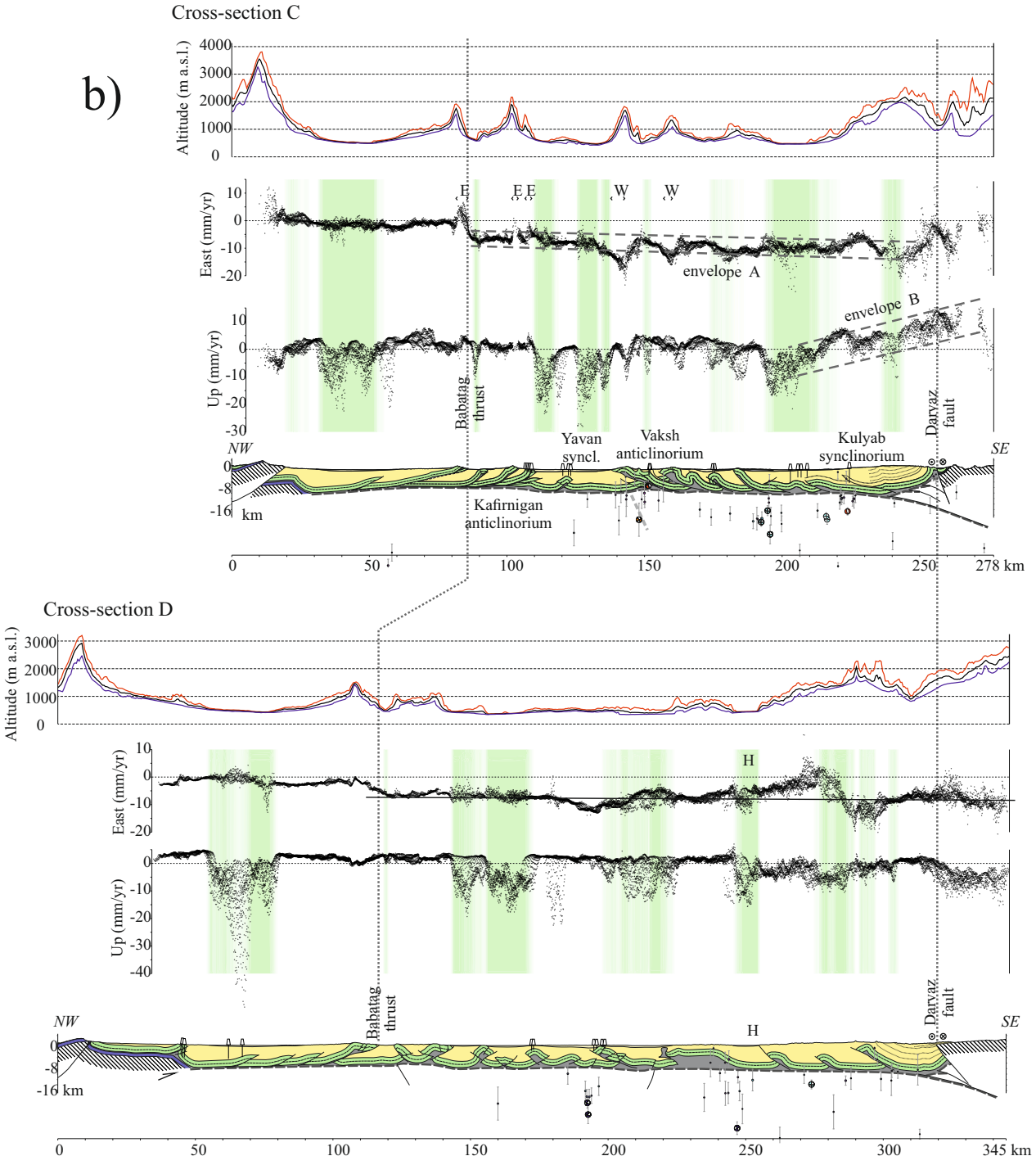

Figure 4. (continued)

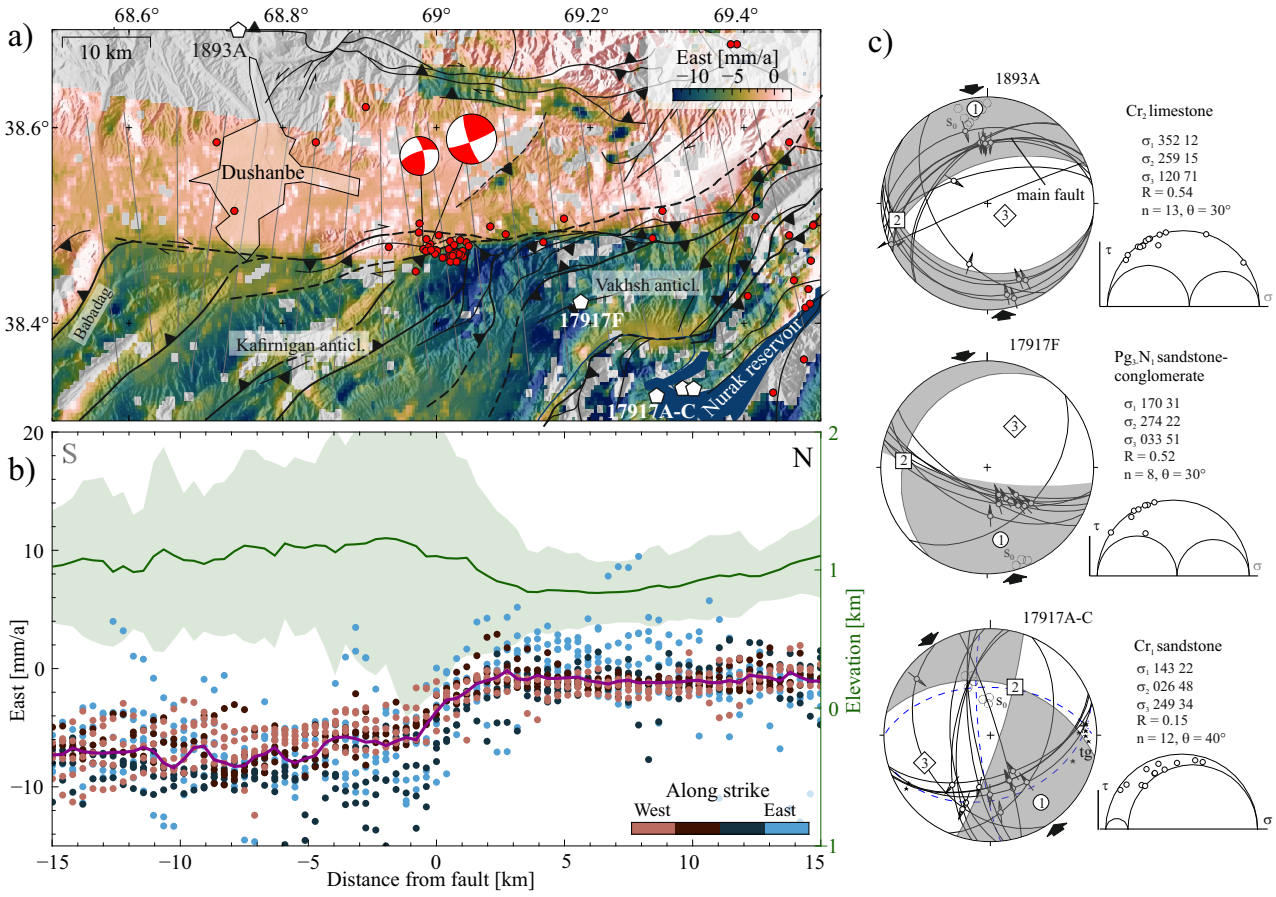

Figure 5. East rates across the Ilyak fault in a) map view and b) as across-fault profile. Background seismicity and focal mechanisms (Kufner et al., 2018) are plotted in red. The profiles in b) are centered along the maximum rate change and are color-coded along strike, indicating different slip behavior. Median rates are plotted in purple, median topography and its deviation is indicated in green. c) Sites that characterize structural data from selected deformation zones north and south of the Ilyak fault, which is badly exposed, mostly due to its anthropogenic overprint. Pure top-to-south thrusting emplaced the crystalline basement of the Tian Shan onto Cretaceous limestone (1893A); the two sites in the Vakhsh anticlinorium characterize that part of the Tajik fold-thrust belt where the overall ∼N-striking thrusts bend into the Ilyak fault zone; they have dextral-transpressive top-to-(N)NW kinematics. Structural data are plotted in lower hemisphere, equal area stereograms. Arrows around the stereograms indicate subhorizontal maximum stress orientations determined from fault-slip analysis (following Sperner & Ratschbacher, 1994). Faults are drawn as great circles and shear directions and striae (slickenlines) as arrows pointing in the direction of the displacement of the hanging wall. Confidence levels of slip-sense determination are expressed in the arrowhead style: solid, certain; open, reliable; half, unreliable. Lithology and strata age (Cr_1: Lower Cretaceous, Cr_2: Upper Cretaceous, Pg_3-N_1: Oligocene-Miocene), and reduced stress-tensor calculations are plotted on the right (principal stress orientations: $\sigma_{1,2,3}$; θ fracture angle used for calculation, R is the shape factor of the stress-ellipsoid, $(\sigma_2-\sigma_3)/(\sigma_1-\sigma_3)$; n: number of data used for calculation; dimensionless Mohr diagram visualizes normal versus shear stress relations for each fault (circles). tg: tensions gashed plotted as poles to the planes, s_0: bedding. Transparent beach balls outline compressional (grey) and extensional (white) dihedra.

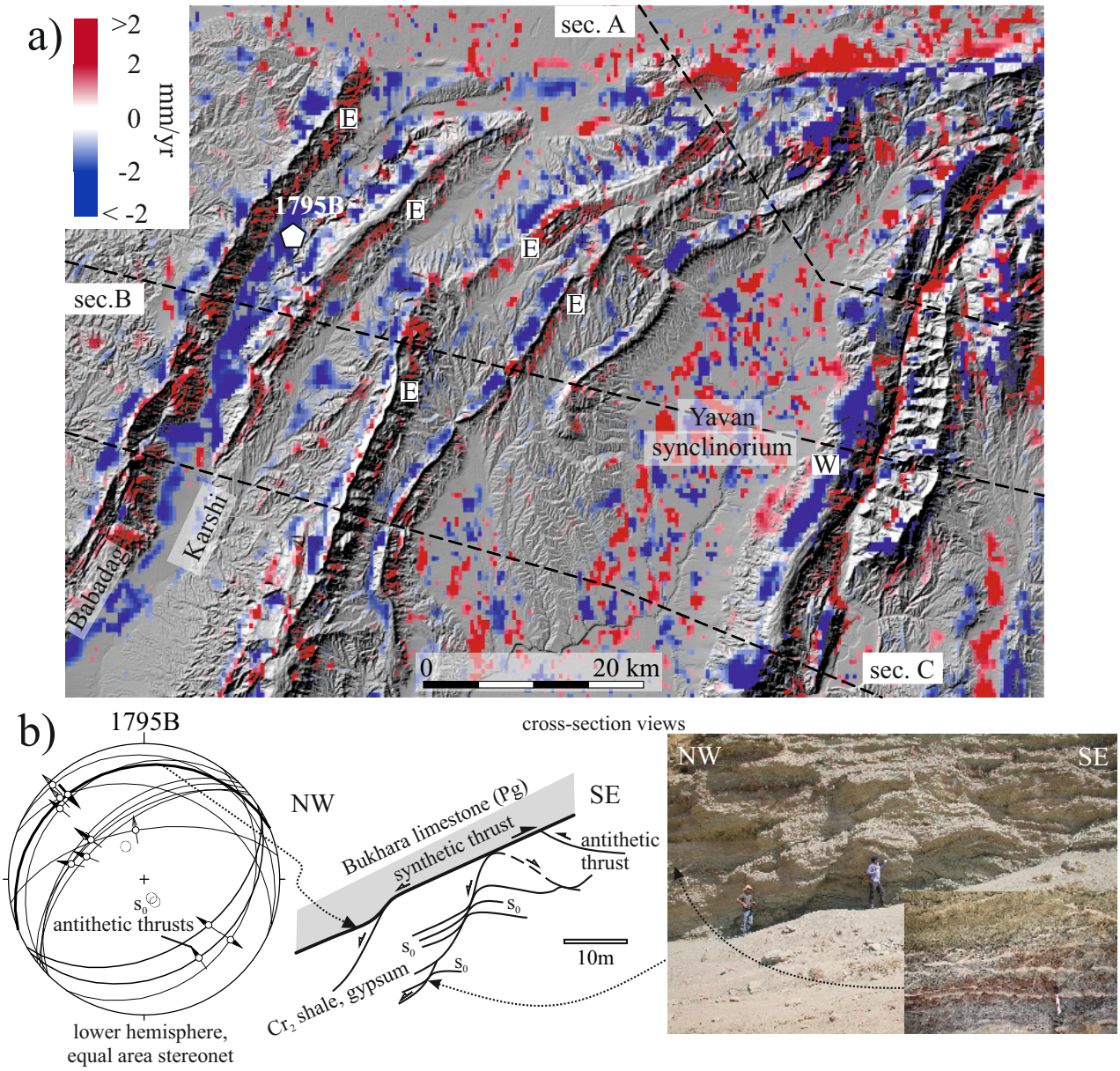

Figure 6. High-pass filtered horizontal displacement map that suppresses the regional component for the northern part of the Kafirnigan anticlinorium superposed over a shaded relief map. Kernel size is 7 pixels, i.e., ∼2800 m. The east-facing scarp slopes of east-facing hogback ridges ("E" markers) show narrow but pronounced positive, the west-facing scarp slopes negative, less pronounced horizontal displacement anomalies. Sign change follows the crests of the topographic hogback ridges, suggesting divergent ground motions. These short-wavelength patterns—superimposed on the regional displacement profiles—are likely related to active gravitationally-induced mass movements. b) Structural evidence for NW-directed mass movement: along a steeply-west-dipping slope in the NW-dipping strata of the Karshi anticline (site 1795B), an Upper Cretaceous shale-gypsum sequence shows dominantly west-directed normal faulting, with the faults planes and numerous tension gashes infiltrated by gypsum. See text for discussion.